

APPLICATION OF DIGITAL THREE-DIMENSIONAL TECHNOLOGIES IN RECONSTRUCTIVE PERIODONTAL SURGERY AND IMPLANT DENTISTRY

PhD thesis

Daniel Palkovics

Károly Rácz Clinical Medicine Doctoral School

Semmelweis University



Supervisor: Dr. Péter Windisch, professor, Ph.D, habil
Official reviewers: Dr. Márk Fráter, assistant professor, Ph.D
Dr. Bence Szabó, assistant professor, Ph.D

Head of the Final Examination Committee:

Dr. Zsolt Németh, associate professor, PhD, med. habil.

Members of the Final Examination Committee:

Dr. Árpád Joób-Fancsaly, associate professor, PhD
Dr. Ákos Nagy, associate professor, PhD

Budapest
2021

TABLE OF CONTENTS

| | |
|---|-----------|
| TABLE OF CONTENTS | 1 |
| LIST OF ABBREVIATIONS | 7 |
| 1. INTRODUCTION | 9 |
| 1.1 Digital data acquisition | 10 |
| <i>1.1.1 Cone-beam computed tomography (CBCT)</i> | 10 |
| 1.1.1.1 Radiation dose | 11 |
| 1.1.1.2 Field-of-view | 12 |
| 1.1.1.3 Image resolution (voxel size) | 12 |
| 1.1.1.4 Artifacts | 13 |
| <i>1.1.2 Intraoral optical scanning (IOS)</i> | 14 |
| 1.2 Digital data processing | 15 |
| <i>1.2.1 Radiographic image processing (segmentation)</i> | 16 |
| 1.2.1.1 Thresholding segmentation methods | 17 |
| 1.2.1.2 Region-based registration methods | 18 |
| 1.2.1.3 Edge detection methods | 19 |
| 1.2.1.4 Artificial intelligence (AI) based segmentation | 20 |
| <i>1.2.2 Computer-aided design</i> | 21 |
| 1.3 Surgical planning in regenerative-reconstructive periodontal surgery and implant dentistry | 23 |
| <i>1.3.1 Diagnostics and surgical treatment planning in periodontology</i> | 23 |
| 1.3.1.1 Clinical examination of periodontal defects | 23 |
| 1.3.1.2 Radiographic examination | 24 |
| 1.3.1.3 Cone-beam computed tomography for the detection of intrabony periodontal defects | 25 |
| 1.3.1.4 Decision making in the surgical treatment of intrabony periodontal defects | 26 |
| <i>1.3.2 Examination and classification of extraction defects</i> | 28 |

| | | |
|------------|--|-----------|
| 1.4 | Regenerative-reconstructive surgical treatment of intrabony periodontal defects and acute alveolar ridge defects following tooth extraction | 31 |
| 1.4.1 | <i>Minimally invasive surgical procedures for the regenerative treatment of intrabony periodontal defects</i> | 31 |
| 1.4.2 | <i>Alveolar ridge preservation</i> | 33 |
| 1.4.2.1 | Extraction site development technique (XSD) | 35 |
| 1.5 | Clinical and radiographic evaluation of surgical outcomes | 38 |
| 1.5.1 | <i>Evaluation of periodontal regeneration following regenerative treatment</i> | 38 |
| 1.5.1.1 | Evaluating outcomes of periodontal regenerative surgery on CBCT datasets | 39 |
| 1.5.2 | <i>Clinical and radiographic evaluation of alveolar ridge alterations</i> | 40 |
| 1.6 | Summary | 41 |
| 2 | OBJECTIVES | 42 |
| 3 | METHODS – PART I: VIRTUAL MODEL ACQUISITION | 43 |
| 3.1 | Semi-automatic segmentation method | 43 |
| 3.1.1 | <i>Delineation of anatomical structures</i> | 44 |
| 3.1.2 | <i>Morphological contour interpolation</i> | 45 |
| 3.1.3 | <i>Smoothing segmentation</i> | 46 |
| 3.2 | Spatial registration of CBCT dataset and intraoral scan | 48 |
| 3.3 | CAD modeling - final virtual patient setup | 50 |
| 3.3.1 | <i>Replacement of tooth crowns</i> | 50 |
| 3.3.2 | <i>Soft tissue CAD modeling</i> | 51 |
| 3.4 | Summary | 53 |
| 4 | METHODS – PART II: CLINICAL APPLICATIONS | 54 |
| 4.1 | Three-dimensional visualization of intrabony periodontal defects for regenerative surgical treatment planning | 54 |

| | | |
|--------------|---|-----------|
| 4.1.1 | <i>Patient selection and radiographic imaging protocol</i> | 54 |
| 4.1.2 | <i>Radiographic image processing</i> | 55 |
| 4.1.3 | <i>Surgical procedure</i> | 56 |
| 4.1.4 | <i>Outcome variables</i> | 57 |
| 4.1.4.1 | Primary outcome measure - Comparison of intrasurgical and digital measurements | 57 |
| 4.1.4.2 | Secondary outcome measure - Preoperative defect assessment | 57 |
| 4.1.5 | <i>Data analysis</i> | 58 |
| 4.2 | Virtual planning and volumetric evaluation in the regenerative-reconstructive surgical treatment of a complex periodontal defect – Case presentation | 59 |
| 4.2.1 | <i>Patient selection, defect description</i> | 59 |
| 4.2.2 | <i>Data acquisition</i> | 60 |
| 4.2.3 | <i>Digital data processing</i> | 61 |
| 4.2.4 | <i>Virtual planning and surgical simulation</i> | 62 |
| 4.2.4.1 | Initial incision and flap elevation | 62 |
| 4.2.4.2 | Regenerative material application | 62 |
| 4.2.5 | <i>Additive manufacturing of hard tissue model</i> | 63 |
| 4.2.6 | <i>Surgical rehabilitation process</i> | 63 |
| 4.2.6.1 | Step 1: Alveolar ridge preservation utilizing the extraction site development technique (XSD) | 63 |
| 4.2.6.2 | Step 2: Periodontal regenerative surgical treatment | 65 |
| 4.2.7 | <i>Follow-up and evaluation of surgical outcomes – Outcome measures</i> | 66 |
| 4.2.7.1 | Primary outcome measure – Volumetric and morphological changes | 67 |
| 4.2.7.2 | Secondary outcome measure – Linear evaluation, radiographic defect fill | 67 |
| 4.3 | CBCT Subtraction Analysis of 3D Changes Following Alveolar Ridge Preservation: a case series of 10 patients with a 6-month follow-up | 69 |
| 4.3.1 | <i>Patient selection</i> | 69 |
| 4.3.2 | <i>Surgical procedure</i> | 70 |
| 4.3.3 | <i>Image acquisition</i> | 70 |

| | | |
|--------------|---|-----------|
| 4.3.4 | <i>Radiographic image processing</i> | 71 |
| 4.3.4.1 | Spatial registration of pre- and postoperative CBCT scans | 71 |
| 4.3.4.2 | CBCT Segmentation and 3D subtraction | 72 |
| 4.3.5 | <i>Outcome variables</i> | 73 |
| 4.3.5.1 | Primary outcome variable – Volumetric and 3D morphological hard tissue alterations | 73 |
| 4.3.5.2 | Secondary outcome measure – Linear measurements of horizontal and vertical dimensions at the surgical area | 74 |
| 4.3.6 | <i>Statistical analysis</i> | 74 |
| 4.4 | Summary | 75 |
| 5 | RESULTS | 76 |
| 5.1 | Digital Hybrid Model Preparation for Virtual Planning of Reconstructive Dentoalveolar Surgical Procedures – Descriptive results | 76 |
| 5.2 | Three-dimensional visualization of intrabony periodontal defects for regenerative surgical treatment planning | 77 |
| 5.2.1 | <i>Baseline patient and defect characteristics</i> | 77 |
| 5.2.2 | <i>Comparison of intrasurgical- and digital measurements – validation of virtual models</i> | 77 |
| 5.2.3 | <i>Preoperative defect morphology assessment</i> | 78 |
| 5.3 | Virtual planning and volumetric evaluation in the regenerative-reconstructive surgical treatment of a complex periodontal defect | 80 |
| 5.3.1 | <i>Volumetric and 3D morphological alterations after stepwise surgical treatment</i> | 80 |
| 5.3.2 | <i>Linear evaluation, radiographic defect fill after reconstructive periodontal treatment</i> | 80 |
| 5.3.2.1 | Baseline defect parameters | 80 |
| 5.3.2.2 | Outcomes at 9-month follow-up | 83 |
| 5.4 | CBCT Subtraction Analysis of 3D Changes Following Alveolar Ridge Preservation: a case series of 10 patients with a 6-month follow-up | 86 |

| | | |
|--------------|---|------------|
| 5.4.1 | <i>Baseline patient demographics</i> | 86 |
| 5.4.2 | <i>Volumetric and 3D morphological analysis</i> | 86 |
| 5.4.2.1 | Baseline 3D defect morphology | 86 |
| 5.4.2.2 | 3D radiographic hard tissue alterations at 6-month follow-up | 87 |
| 5.4.3 | <i>Linear evaluation of alveolar ridge alterations</i> | 89 |
| 5.5 | Summary | 90 |
| 6 | DISCUSSION | 91 |
| 6.1 | LEVEL 1 - Digital hybrid model acquisition method | 91 |
| 6.1.1 | <i>Discussion of model preparation method</i> | 91 |
| 6.1.2 | <i>Advantages</i> | 91 |
| 6.1.3 | <i>Disadvantages, future improvements</i> | 93 |
| 6.2 | LEVEL 2 - 3D diagnostics and postoperative evaluation method | 94 |
| 6.2.1 | <i>Three-dimensional visualization of intrabony periodontal defects for regenerative surgical treatment planning</i> | 94 |
| 6.2.1.1 | Discussion of 3D diagnostic method | 94 |
| 6.2.1.2 | Advantages | 95 |
| 6.2.1.3 | Disadvantages, improvements | 96 |
| 6.2.2 | <i>Virtual planning and volumetric evaluation in the regenerative-reconstructive surgical treatment of a complex periodontal defect</i> | 98 |
| 6.2.2.1 | Discussion of 3D diagnostic and evaluation method | 98 |
| 6.2.2.2 | Advantages | 99 |
| 6.2.2.3 | Disadvantages, future improvements | 100 |
| 6.2.3 | <i>CBCT Subtraction Analysis of 3D Changes Following Alveolar Ridge Preservation: a case series of 10 patients with a 6-month follow-up</i> | 100 |
| 6.2.3.1 | Discussion of 3D evaluation method | 100 |
| 6.2.3.2 | Advantages | 101 |
| 6.2.3.3 | Disadvantages, future improvements | 102 |
| 6.3 | LEVEL 3 - Analysis of clinical outcomes | 103 |

| | | |
|--------------|---|------------|
| <i>6.3.1</i> | <i>Three-dimensional visualization of intrabony periodontal defects for regenerative surgical treatment planning</i> | 103 |
| <i>6.3.2</i> | <i>Virtual planning and volumetric evaluation in the regenerative-reconstructive surgical treatment of a complex periodontal defect</i> | 104 |
| <i>6.3.3</i> | <i>CBCT Subtraction Analysis of 3D Changes Following Alveolar Ridge Preservation: a case series of 10 patients with a 6-month follow-up</i> | 105 |
| 7 | CONCLUSIONS | 107 |
| 8 | SUMMARY – ENGLISH | 109 |
| 9 | SUMMARY – HUNGARIAN | 110 |
| 10 | BIBLIOGRAPHY | 111 |
| 11 | BIBLIOGRAPHY OF THE CANDIDATE’S PUBLICATIONS | 132 |
| 12 | ACKNOWLEDGEMENT | 133 |

LIST OF ABBREVIATIONS

2D: two-dimension

3D: three-dimension

AI: artificial intelligence

ALADAIP: as low as diagnostically acceptable being indication-oriented and patient-specific

ALARA: as low as reasonably achievable

ANN: artificial neural network

AR: augmented reality

ARP: alveolar ridge preservation

BC: bone crest

BD: bottom of the defect

BDX: bovine derived xenograft

CAD: computer-aided design

CAL: clinical attachment level

CAM: computer-aided manufacturing

CBCT: cone-beam computed tomography

CEJ: cemento-enamel junction

CNN: convolutional neural network

CT: computer assisted tomography

DL: deep learning

DMFR: in dento-maxillofacial radiology

E.A.O.: European Association of Osseointegration

EDS: extraction defect sounding

EMD: enamel matrix derivative

EPPT: entire papilla preservation technique

FMBS: full mouth bleeding score

FMPS: full mouth plaque score

FOV: field-of-view

GTR: guided tissue regeneration

IGT: Image Guided Therapy

INTRA: intrabony component depth

IOS: intraoral optical scan

IR: intraoral periapical radiographs

ITK: Insight Toolkit

MIS: minimally invasive surgical approach

MIST: minimally invasive surgical technique

ML: machine learning

M-MIST: modified minimally invasive surgical technique

MPR: multiplanar reconstruction

NIPSA: non-incised papilla surgical approach

OBJ: object (file format)

PCL: polycaprolactone

PPD: probing pocket depth

REC: gingival recession

ROI: region of interest

SD: standard deviation

SFA: single flap approach

SLA: stereolithography (3D printing technology)

STL: stereolithography (file format)/
standard tessellation language

VBS: virtual bone sounding

VISTA: vestibular incision
subperiosteal tunnel access

V-MIS: videoscope assisted minimally
invasive surgical approach

VREC: virtual gingival recession

WIDTH: root surface-bone crest
distance

XSD: extraction site development

1. INTRODUCTION

Rapid technological advances in dentistry have enabled computer-aided planning and treatment. Digital technologies are applied in all fields of dental care nowadays. In periodontology (1), dentoalveolar surgery, implant dentistry (2), endodontic surgery (3), and maxillo-facial surgery (4), procedures can be planned virtually, and navigated surgeries can be performed with the aid of different guide systems. During prosthetic rehabilitation, digital methods are used to design and manufacture conventional or implant-retained prostheses, and with the application of chair-side systems direct final restorations can be provided for the patient immediately (5). Orthodontists can use backward planning in accordance with the final occlusion to digitally plan each phase of treatment (6). Integration of additive manufacturing facilitates the point-of-care production of anatomical models, surgical guides, temporary prostheses, and orthodontic splints (7).

A workflow on computer-aided surgical planning in general medicine has been published by *Matsumoto et al.* (8) affiliated with the Mayo Clinic (Rochester, Minnesota, USA), which can be considered one of the pioneers in the application of medical 3D technology. Elements from this workflow and other similar articles (9-11) can be implemented into the digital three-dimensional (3D) planning of surgical procedures in periodontology and implant dentistry (*Figure 1.*), which consists of the following steps: (i) digital data acquisition, (ii) digital data processing, (iii) virtual surgical planning, (iv) computer-aided surgical procedure, and (v) three-dimensional postoperative evaluation.

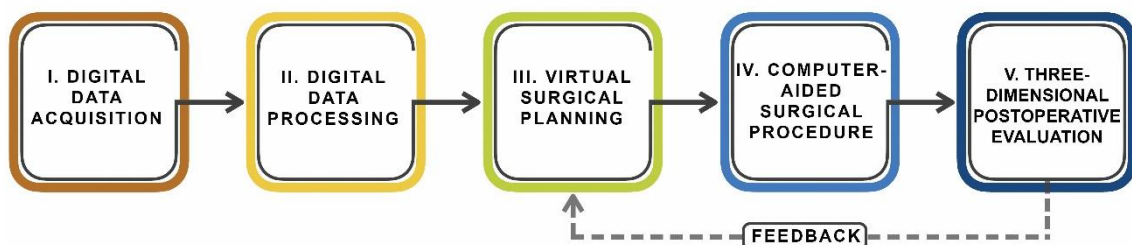


Figure 1.: Digital workflow in periodontology and implant dentistry

1.1 Digital data acquisition

Two essential methods for 3D data acquisition in digital dentistry are: (i) cone-beam computed tomography (CBCT) and (ii) intraoral optical scanning (IOS). CBCT is utilized to acquire volumetric data of hard tissues (alveolar bone and teeth). It is routinely used in the planning of many different types of surgical procedures (i.e., alveolar ridge preservation, alveolar ridge augmentation, sinus elevation, and dental implant placement). Intraoral optical surface scanners provide digital information on the clinical scenario (clinical crown of the teeth and soft tissues). With the combination of these methods, digital information of all anatomical structures relevant for surgical planning can be acquired.

1.1.1 Cone-beam computed tomography (CBCT)

Arguably one of the biggest achievements in modern medicine was the invention and constant development of radiographic imaging modalities. Radiography in healthcare allows clinicians to view parts of the human body in ways that are impossible with the naked eye. Soon after the first discovery of X-rays (radiation between wavelengths of 10 pm and 10 nm) by Wilhelm Conrad Röntgen on November 8th, 1895, dentists very quickly recognized the diagnostic advantage of this type of radiation in their own field (12). Radiography since then has become the most common diagnostic modality in dentistry. The next major historical landmark in radiology was the invention of computer assisted tomography (CT) in 1979 by Allan M. Cormack and Godfrey N. Hounsfield, which allowed the viewing of three-dimensional images of anatomical structures and related pathologies.

Eventually conventional CT imaging was used in dental diagnostics, however after the introduction of cone beam technology in 1996 (QR s.r.l. NewTom 9000) (13) it quickly took over and has become the gold standard in dental 3D imaging. The main reasons for its success are accessibility, compact size, low cost, and relatively low radiation dose. Beyond its diagnostic applications CBCT images are also often used for presurgical

treatment planning and occasionally even postoperatively for the evaluation of healing or in cases of post-surgical complications.

Many factors determine the success of CBCT application in diagnostics and surgical planning. Recommendations were established by *Jacobs et al.* (14) that clinicians should follow for optimal individualized CBCT image acquisition. Parameters of the imaging device should be calibrated for each individual case as determined by the application. The following factors determine the quality and diagnostic value of CBCT images: (i) radiation dose, (ii) field-of-view (FOV), (iii) image resolution (voxel size), (iv) artifacts.

1.1.1.1 Radiation dose

The biggest concern in 3D imaging compared to conventional two-dimensional imaging modalities is the elevated radiation dose. Levels vary greatly between CBCT devices due to the lack of standardization. The radiation dose of CBCT machines was found to be between 10 μSv and 1000 μSv , which is equivalent to 2-100 panoramic X-rays (14-16), yet still much lower than conventional CT devices. However, it was stated in the European Association of Osseointegration (E.A.O.) 2011 guidelines that the application of CBCT can be justified if clinical benefits exceed risks (17). Application for preoperative planning can be justified by anatomical considerations, complex defect morphologies, insufficient bone volume, the use of advanced surgical techniques, and computer-aided dental implant placement (1-4). This resulted in a transition from the classic principle of “as low as reasonably achievable” (ALARA) (18) to “as low as diagnostically acceptable being indication-oriented and patient-specific” (ALADAIP) (19).

In recent years low-dose protocols have emerged that lower exposure factors without significant deterioration of image quality and diagnostic utility (20, 21). Dose reduction can be achieved by reducing field-of-view, tube current, scan time, or the number of projections, and by utilizing partial rotation modes. Limited evidence can be found in the literature for the application of low-dose CBCT protocols in periodontology and implant dentistry. Dose reduction is achieved by reducing tube current, anode voltage, and resolution (22, 23).

1.1.1.2 Field-of-view

FOV size can generally be categorized into large, medium, and small. In large FOV scans craniofacial structures beyond the oral cavity and the maxillary sinus floor are visible, medium FOV scans are limited to dentoalveolar structures, and small FOV scans are localized to a specific area and usually capture few adjacent teeth within their periapical regions (16). Smaller FOV images achieve better image resolution and have a lower radiation dose but show more pronounced artifacts, noise, and a greater variability of density values. Large FOV images have lower resolution with more consistent gray values and an elevated radiation dose (24). Due to the significant differences in image properties between the different FOV sizes, it is suggested to use the field-of-view that is best suited for the specific case (17).

1.1.1.3 Image resolution (voxel size)

CBCT images are considered high resolution radiographic images compared to conventional CT scans, with voxel sizes ranging from 80–400 μm . Smaller voxel sizes have advantages in depicting small areas such as root canals and periodontal tissues (*Figure 2.*). Higher resolution images also aid the radiographic segmentation process, therefore higher quality models can be acquired (15). However, radiation dose increases with image resolution, therefore smaller voxel sizes (sub 100 μm) are usually only applicable in small FOV scans which cannot be utilized for presurgical virtual treatment planning in certain cases. Hence, an ideal FOV-voxel size ratio should be

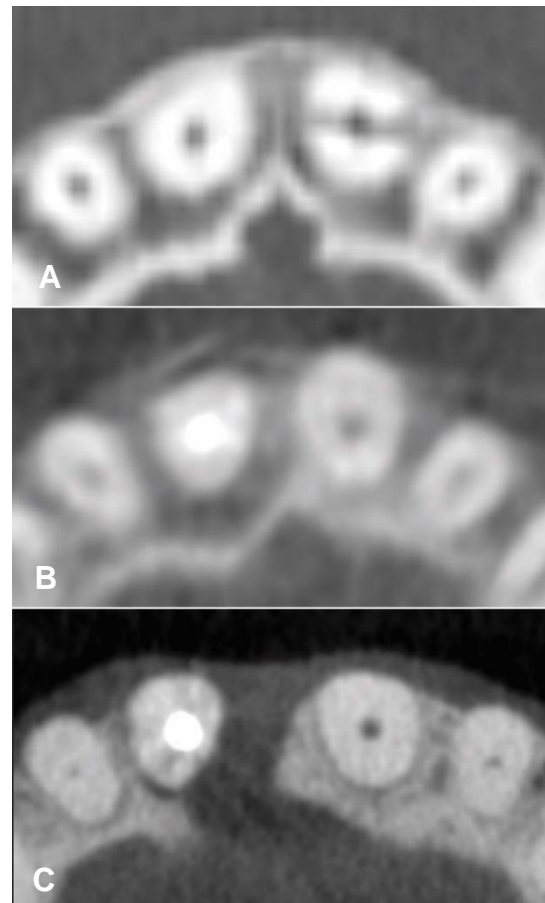


Figure 2.: Radiographic images with different resolution (voxel size)
A: 750 μm CT scan; B: 300 μm CBCT scan; C: 150 μm CBCT scan

selected. For virtual planning of surgical procedures a medium FOV scan with a voxel size of 150 – 200 μm should be sufficient (25).

1.1.1.4 Artifacts

Probably the greatest hinderance in dental 3D imaging is the formation of artifacts on CBCT images, which compromise image quality and diagnostic accuracy (*Figure 3.*). Artifacts are distortions or errors in the image that are unrelated to the object being examined. The most common artifacts that are present on CBCT images include: (i) beam hardening, (ii) extinction artifacts, and (iii) exponential edge gradient effects (26). Artifacts caused by high density objects (i.e., metal and zirconia restorations, titanium implants) are called "metal artifacts" (27).

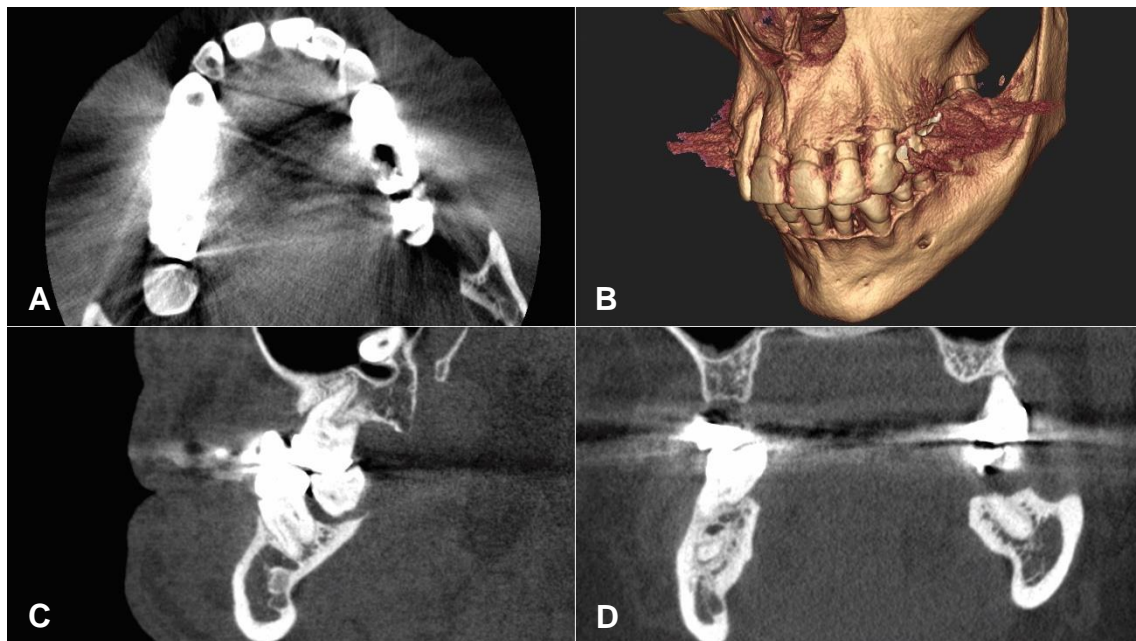


Figure 3.: CBCT image with extensive metal artifacts produced by dental restorations
A: Axial view; B: 3D view; C: Sagittal view; D: Coronal view

Methods can be utilized to reduce artifacts on final CBCT images and can be divided into two groups. Firstly, there are methods that can be applied in specific cases to prevent or minimize artifact formation during scanning, such as: (i) adjusting the field-of-view by excluding diagnostically unimportant areas with metal objects, (ii) removing non-permanently fixed restorations prior to imaging, (iii) avoid using thick scanning templates or ones that are fabricated from high density materials, and (iv) placing cotton rolls

between the upper and lower teeth to prevent complete occlusion (2). Secondly, different metal artifact reduction algorithms can be applied during the post-processing of the raw projections (i.e., interpolation-based methods, iterative reconstruction algorithms, and adaptive filtering algorithms) (28)

1.1.2 Intraoral optical scanning (IOS)

CBCT scans are utilized to visualize hard tissues in 3D. Intraoral scanners (IOS), which are used to directly acquire 3D digital data of dentogingival structures (*Figure 4.*), were introduced in 1987 as an element of a newly developed computer-aided design/computer-aided manufacturing (CAD/CAM) system for dental use called Chairside Economical Restoration of Esthetic Ceramics (CEREC®, Dentsply Sirona, York, Pennsylvania, USA) (29-31). Since the late 1980s almost every major dental company has been developing their own system, and today more than a dozen different types of intraoral scanners are commercially available.

The original intended purpose of IOS was to directly acquire digital models of patients for chairside planning and fabrication of dental prostheses, however due to the wide range of possible applications its use was quickly implemented in other fields of dentistry. Primarily, IOS can substitute the use of traditional impressions in the prosthetic rehabilitation of patients (32) allowing for a completely digital workflow to be applied (33).

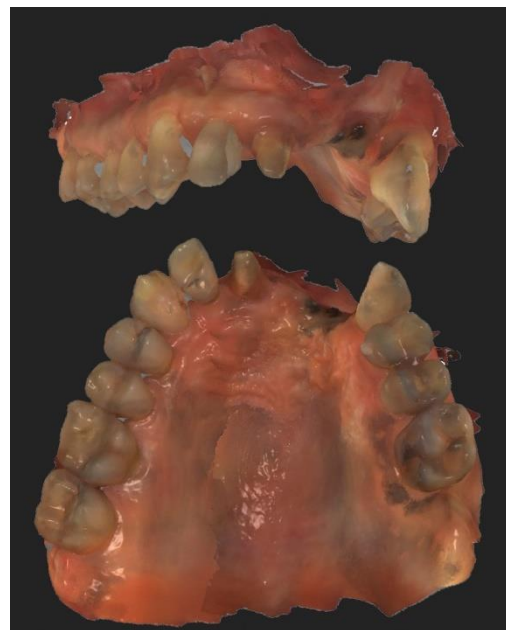


Figure 4.: Intraoral optical surface scan

Based on digital models acquired with IOS and backward planning, orthodontists utilize removable, semi-elastic aligners (Invisalign®, Align Technology, Santa Clara, California, USA) for orthodontic tooth movement (34, 35). Maxillo-facial surgeons combine IOS with CBCT scans to digitally plan and simulate orthognathic surgeries (4). Furthermore, in implantology the combination of CBCT datasets and stereolithography

(STL) files of IOS is used for the planning of dental implant placement and the fabrication of static drilling guides (2).

1.2 Digital data processing

To further increase the diagnostic value of digital data and to enhance the clarity of the acquired images, digital data have to be processed with the help of a computer and dedicated image analysis and modeling software. According to a recent article by Vandenberghe in 2018, digitization (36) and data processing aid conventional treatment planning on three distinct levels:

1. **Digital patient:** Acquired digital data (CBCT, IOS) are stored and can be viewed, however data are still unprocessed (*Figure 5.*).

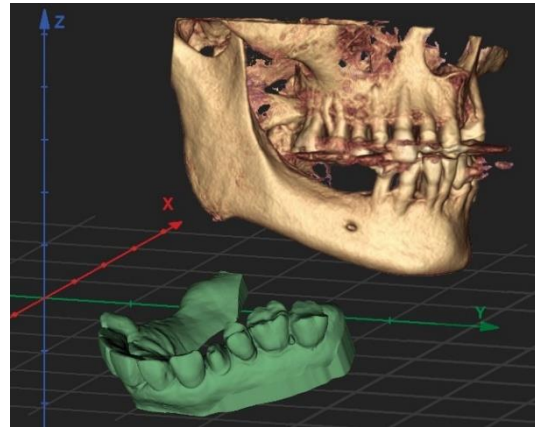


Figure 5.: Digital patient

2. **Virtual patient:** Acquired data are processed and combined. A virtual 3D representation of the patient appears on screen allowing for virtual treatment planning (*Figure 6.*).

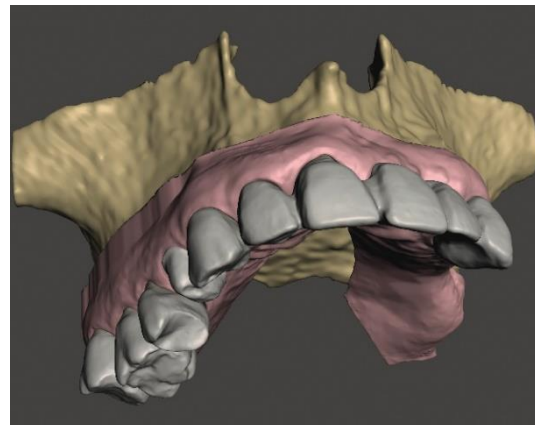


Figure 6.: Virtual patient

3. **“Real” patient:** Virtual 3D models are manufactured with additive (3D printing) or subtractive (milling) methods. 3D printed models are utilized prior to and during surgical treatment to enhance haptic perception. (Figure 7.).



Figure 7.: “Real” patient model manufactured with stereolithography (SLA) 3D printing technology

Virtual patient setup allows for the development of virtual treatment planning and simulation of various surgical interventions, ultimately reducing occasional errors (37). In cases where haptic feedback is necessary to plan certain interventions, application of the “real” patient concept can be applied with the help of realistic 3D printed anatomical models. However, in most cases in periodontal, dentoalveolar, and implant surgery virtual planning is sufficient, therefore only the virtual patient concept will be addressed.

Data processing in digital dentistry consists of two major steps: (i) radiographic image processing (segmentation) and (ii) CAD modeling.

1.2.1 Radiographic image processing (segmentation)

Segmentation is the process where labels are designated to pixels (2D) or voxels (3D) to distinguish anatomical objects from each other and from the background in order to facilitate image analysis. Segmentation is a crucial step in 3D visualization, treatment planning, and volumetric evaluation (38-40). As a result, clinicians can acquire 3D virtual models from the CBCT scans of the patient to enhance diagnosis and treatment planning.

Segmentation methods can be classified into multiple groups: (i) classical image segmentation methods (thresholding, region-based, edge-based methods), (ii) pattern recognition-based methods, (iii) deformable models, (iv) wavelets-based methods, (v)

atlas-based techniques, and (vi) knowledge-based techniques (40). For maxillo-facial applications, thresholding methods, region-based registration, edge detection methods, and knowledge-based techniques are the most frequently applied segmentation modalities, therefore only these techniques will be discussed in detail from a clinician's point of view.

1.2.1.1 Thresholding segmentation methods

Among classical image segmentation methods, thresholding algorithms are the most frequently used. Thresholding methods can be categorized into two groups: (i) *global thresholding* and (ii) *local adaptive thresholding* (40).

Global thresholding is the quickest and most straightforward segmentation method. It is incorporated into most DICOM imaging and implant planning software, the use of which involves the selection of a voxel grey value limit, and voxels with higher intensity levels will be classified as the region of interest (ROI) (39) separating them from the background (*Figure 8.*). In a recent study, a significant difference in surface variation and point-to-point distance has been found between models segmented with different global threshold values, subsequently

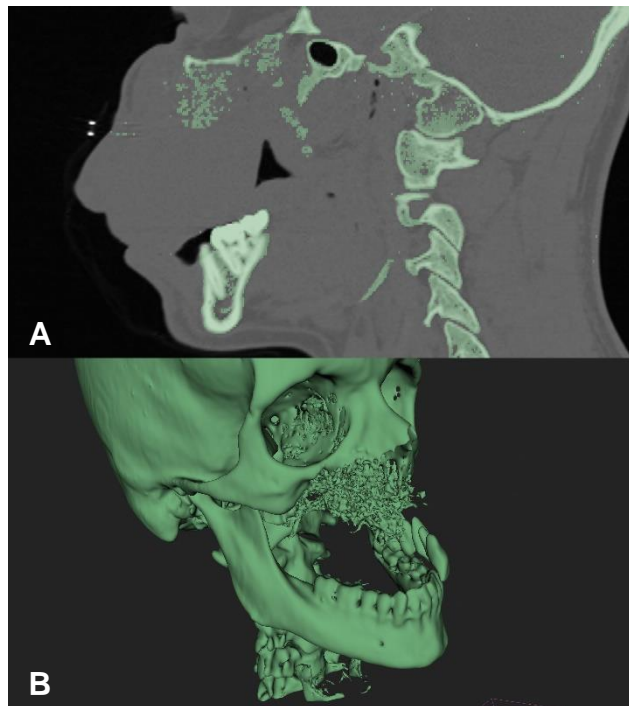


Figure 8.: Results of global thresholding segmentation

A: 2D Sagittal view; **B:** 3D model

affecting the accuracy of reconstructed 3D models (41). This effect has been observed by the authors in both CT scans and CBCT scans, however due to the diverse voxel intensities of CBCT scans segmentations were affected more heavily in the latter case. Therefore, segmentations may be inaccurate, lowering their diagnostic value.

Local adaptive methods set a threshold limit for all pixels based on the intensity of their locality. Adaptive thresholding methods have previously been used for the segmentation of endodontic CBCT and μ CT (reference) images taken of extracted teeth. The authors compared the results of the two imaging modalities and found no significant difference between the two, therefore concluded that adaptive thresholding may be a valuable tool for clinical use (42). The aforementioned article and one other on the same topic (43) both conducted examinations on extracted, preserved teeth, however literature data regarding the clinical application of adaptive thresholding is very limited.

1.2.1.2 *Region-based registration methods*

The most prominent region-based registration algorithms are (i) *region-growing* segmentation and (ii) *watershed algorithm* (40).

Region-growing segmentation includes the selection of groups of pixels named ‘seeds’ and region-growing around these using homogeneity criteria (44). Region-growing algorithms are fast; they have therefore been used for segmentation in dento-maxillofacial radiology (DMFR) (45, 46). The disadvantage of region-growing methods is that they are relatively sensitive to noise, therefore multiple seeds must be selected manually, which may increase the duration of the process (*Figure 9*).

Watershed methods are remarkably similar to region-growing methods; they work based on grayscale mathematical morphology. Watershed algorithms are among the more popular semi-automatic segmentation methods in DMFR (47-49).

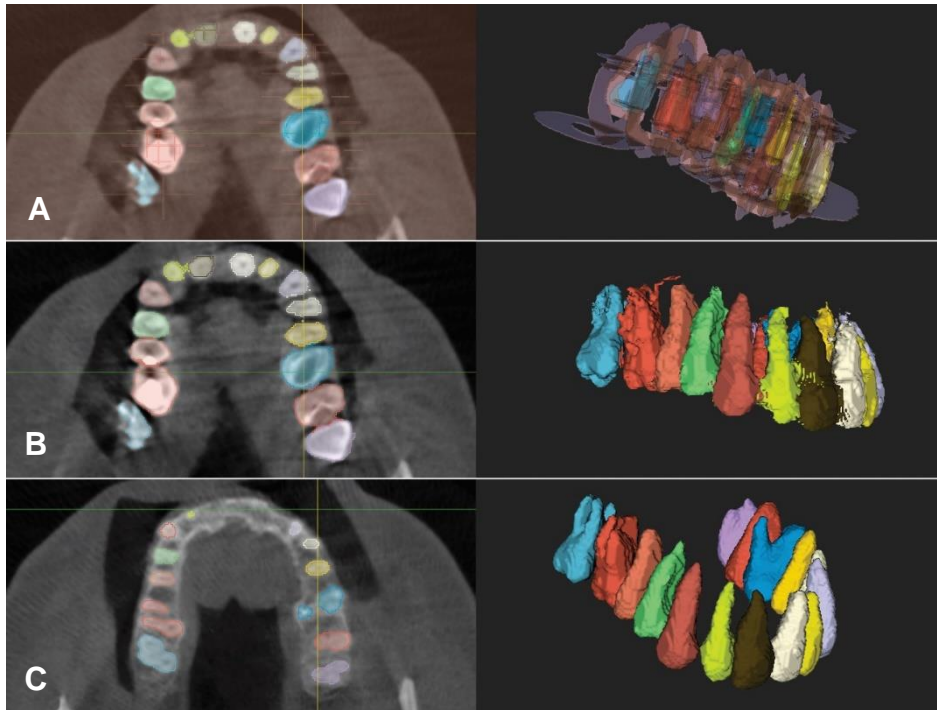


Figure 9.: *Region growing method*

A: *Separation of different anatomical structures from the background;*

B: *Unedited result of region growing; C: Smoothed 3D model*

1.2.1.3 Edge detection methods

Edge detector algorithms scan images for areas where pixel intensity values change drastically along a certain direction (40, 50). Edge-detection methods utilize different operators (e.g. Prewitt, Sobel, Roberts, and Laplacian of Gaussian) to calculate edges (51). Edge detection has previously been used for the segmentation of endodontic images and titanium implants, both in preclinical settings (52, 53). Neither of the articles reported any significant difference in results compared to reference images, and in the case of implants the edge detection method was found to be more reliable than manual thresholding methods (52).

1.2.1.4 Artificial intelligence (AI) based segmentation

In recent years, development in automatic image segmentation has aimed to reduce image processing duration and to avoid inter/intra-examiner errors (54) (*Figure 10*).

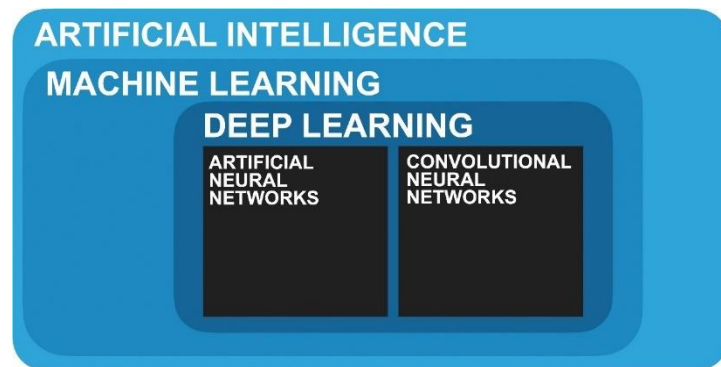


Figure 10.: overview of artificial intelligence, machine learning, and deep learning

Machine learning (ML) is a part of artificial intelligence

that is used to analyze large amounts of data. Machine learning is an adaptive computer algorithm that carries out data processing based on a sample database (training data) (55). In radiographic image analysis a subclass of ML called deep learning (DL) is applied. It utilizes a hierarchical network of nodes, called an artificial neural network (ANN) – constructed similarly to the human brain – to analyze data. ANNs might be used to analyze extracted radiomic features of images, rather than the images themselves. Also, results are limited by the quality of the input database. Alternatively, radiographic images may be fed into a convolutional neural network (CNN) to analyze features directly on unlabeled images (56) (*Figure 11*). Current applications of DL and radiomics in DMFR have been summarized in recent review articles (57, 58). It was found that the overwhelming majority of articles utilized CNNs for analysis of intraoral radiographs, panoramic x-rays, and CBCT datasets (57). The majority of the reviewed articles utilized AI-based segmentation of CBCT images for the detection of (i) periapical pathologies, or (ii) the localization of anatomical landmarks for the digital planning of orthodontic/orthognathic treatments (58). This is most likely due to the fact that these applications are the least effected by the limitations of AI-based segmentation, as was pointed out in both review articles.

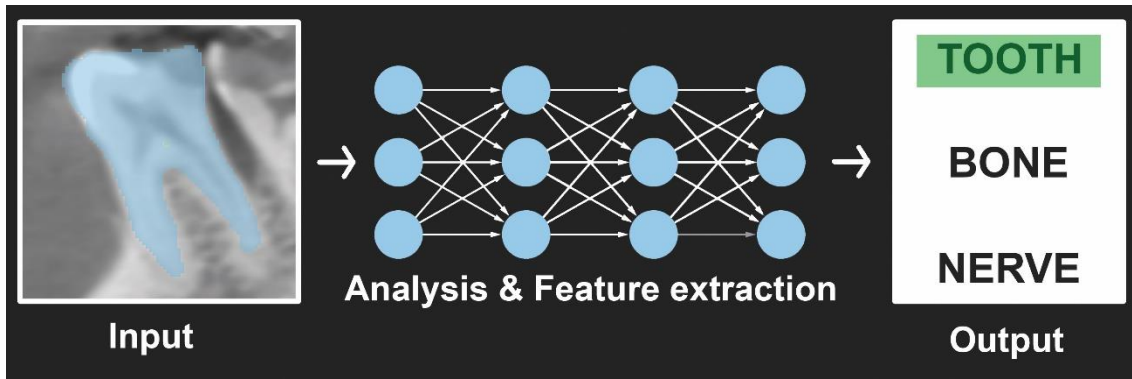


Figure 11: Working process of convolution neural networks

The number-one limitation is the heterogeneity of sample databases, due to the morphological diversity of hard tissue defects (periapical, periodontal, alveolar); differences in radiographic density; and lack of corticalization at pathologic areas, resulting in unreliable outcomes. Another notable limitation is the relative low availability of AI-based segmentation algorithms. Additionally, currently available algorithms have been trained on CBCT datasets with confirmed types of defects, therefore they can only be used for the segmentation of these specific defects. AI-based segmentation algorithms so far however have not been developed for the segmentation of periodontal patients (58).

1.2.2 Computer-aided design

Computer-aided design (CAD) involves using computers to aid the creation, modification, analysis, or optimization of a wide range of applications in various fields, such as (i) the automotive industry, (ii) the shipbuilding industry, (iii) the aerospace industry, (iv) architectural design, (v) computer animation, (vi) medicine, and (vii) dentistry (59, 60). There are many different CAD subcategories developed for different purposes. In oral surgery and periodontology, the main focus of CAD modeling is (i) refinement of 3D models acquired by the segmentation of CBCT datasets and IOS, and (ii) design and fabrication of static surgical guides to aid the surgical process (61). For both applications, mesh modeling and free form surface modeling are employed.

The most commonly used file format for CAD modeling in dentistry is the stereolithography (STL) file format, often called a “standard tessellation language” file. The STL file format describes the surface geometry of three-dimensional objects with tessellation. Tessellation tiles the surface of an object using multiple basic geometric shapes (*Figure 12.*). An STL file consists of vertices, edges, and triangulated surfaces (62).

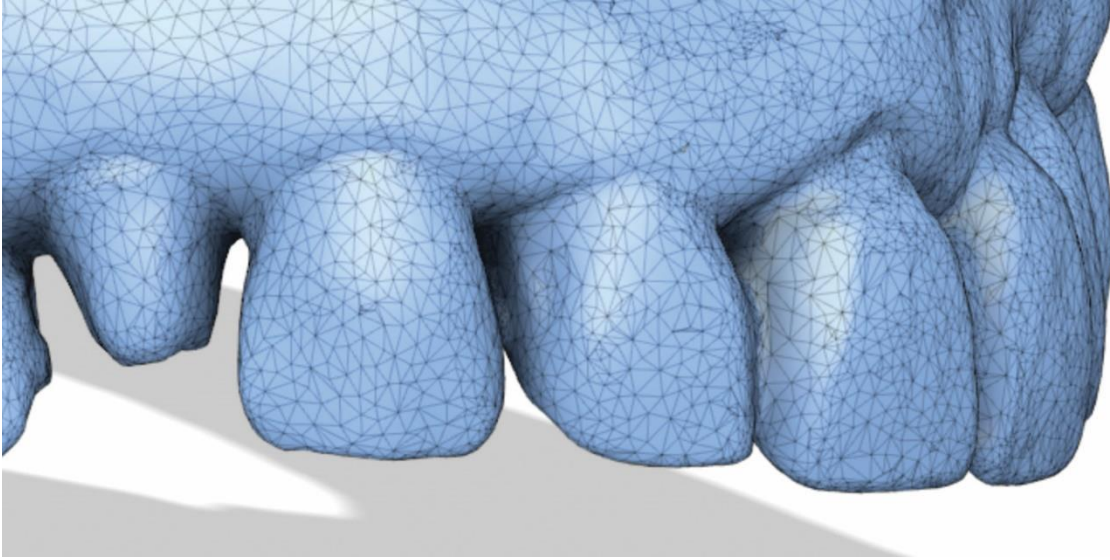


Figure 12.: STL file of an IOS with visible triangles

1.3 Surgical planning in regenerative-reconstructive periodontal surgery and implant dentistry

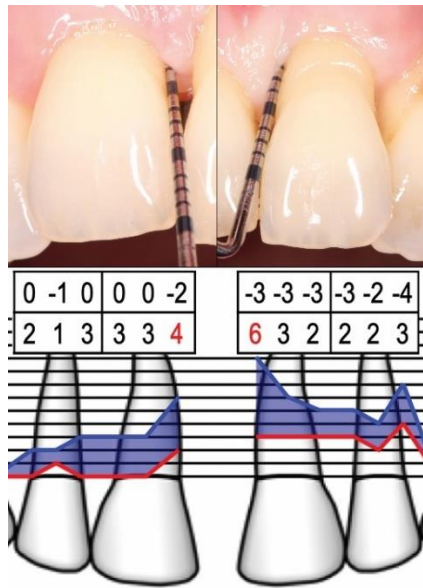
This section will detail the currently available tools for diagnostics and treatment planning of (i) periodontal intrabony defects around teeth with favorable and questionable prognosis, as well as (ii) acute alveolar ridge defects following the extraction of periodontally involved teeth with a hopeless prognosis. In the case of advanced defects further hard tissue augmentation at the edentulous ridge may be necessary, however planning and surgical therapy will not be discussed in the current thesis.

1.3.1 Diagnostics and surgical treatment planning in periodontology

Diagnostic processes have been well established in periodontology for many years with specific clinical and radiographic protocols. Conventional diagnostic methods include clinical measurements with a periodontal probe (63) and the series of 14 intraoral periapical radiographs (IR) referred to as a periodontal status radiograph (64). The combination of these methods is used to determine the stage/grade of the disease (65), the single tooth prognosis, and to plan surgical interventions. Even though these diagnostic methods are routinely used, both have notable downsides. To overcome these limitations, articles have suggested alternative methods, such as the application of CBCT scans for the diagnosis and treatment planning of periodontitis (66-69).

1.3.1.1 Clinical examination of periodontal defects

Clinical assessment of the staging and grading of periodontal processes is executed by measuring probing pocket depth (PPD), gingival recession (REC), and clinical attachment loss (CAL) (*Figure 13.*). Clinical examination utilizing different types of periodontal probes (e.g., UNC-15 probe, WHO probe, Williams probe, Nabers probe) is a highly subjective method that may be determined by many different factors; therefore, measurements are often difficult to reproduce accurately. Soft tissue oedema, overhanging restorations, and calculus make it difficult to standardize probing angles and



probing forces, subsequently producing unpredictable results. Clinical studies on the accuracy of periodontal probing have shown that clinicians underestimated the extent of intrabony defects during clinical examination prior to periodontal surgery (70, 71). As a result, surgical techniques may be adjusted during intervention. Clinical studies often utilize pressure-sensitive probes to reduce errors (72).

Figure 13.: Clinical examination

1.3.1.2 Radiographic examination

Periodontal status radiographs consist of 14 intraoral periapical radiographs acquired with a parallel long-cone technique where the angle of the film/sensor is parallel to the long axis of the tooth in order to avoid distortion of the image (73) (*Figure 14.*). However, traditional radiographic imaging methods (IR, panoramic x-ray) produce a planar summation image where overlapping anatomical structures make it difficult to analyze the morphology of periodontal defects accurately. Furcation defects, three wall intrabony defects, midbuccal intrabony defects, interdental craters, and dehiscence-type defects are the most difficult to analyze on IRs (74-77).

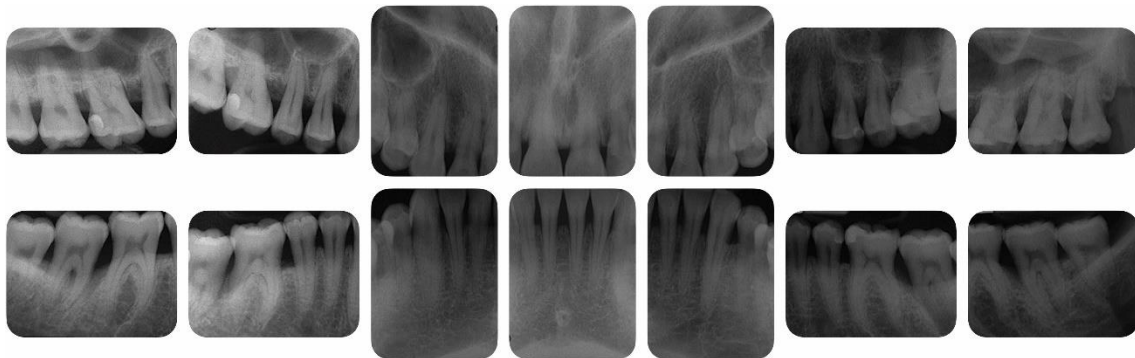


Figure 14.: Periodontal status radiograph comprised of 14 periapical radiographs

1.3.1.3 Cone-beam computed tomography for the detection of intrabony periodontal defects

Due to the aforementioned limitations, several authors suggested the application of CBCT scans for diagnosis of periodontal defects in cases where sufficient information cannot be gained using conventional methods (74-77). CBCT scans are used for the detection and classification of furcation and intrabony defects (*Figure 15.*). Articles comparing results to IRs and clinical examination concluded that linear measurement of intrabony defects and furcation lesions is significantly more accurate on CBCT scans compared to clinical examination and IRs (78-82). Findings are also supported by several systematic reviews

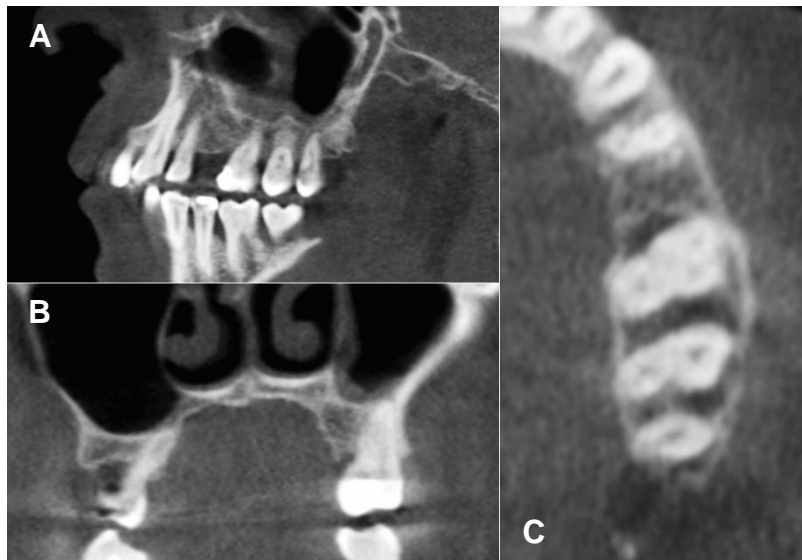


Figure 15.: CBCT visualization of a periodontal defect around tooth 26 and 27

A: Sagittal view; **B:** Coronal view; **C:** Axial view

(66, 68, 69, 83). In previously mentioned articles and systematic reviews however, detection and diagnosis of periodontal lesions were performed on two-dimensional slices of CBCT scans.

To acquire a realistic representation, CBCT datasets need to be reconstructed in 3D with one of the

previously mentioned segmentation methods. There are limited number of articles available in the literature that analyze periodontal defect morphologies on three-dimensional virtual models segmented from CBCT scans (1, 84-88). In their article, *Güth et al.* combined CBCT datasets with STL files of an intraoral scan, creating a virtual patient setup for surgical simulation prior to esthetic crown lengthening. CBCT segmentation was carried out by the global thresholding method, therefore 3D models were compromised by the shortcomings of this method (1). *Tayman et al.* and *Gonçalves et al.* analyzed the volume of intrabony periodontal defects and furcation lesions on a

CBCT dataset using manual color delineation for segmentation, however segmentation of teeth and alveolar bone was not performed, therefore baseline defect morphology could not be assessed (85, 87). Besides analyzing baseline periodontal defect volume, *Nemoto et al.* assessed the volumetric defect fill by manual delineation on axial images, however defect morphology was not reconstructed in 3D (84). None of the previous articles utilized 3D models for virtual planning of regenerative treatment of intrabony periodontal defects.

1.3.1.4 Decision making in the surgical treatment of intrabony periodontal defects

In 2015 *Cortellini and Tonetti* published an article that summarizes concepts for the regenerative treatment of intrabony periodontal defects (89). The article discusses patient-related factors (general conditions) and site-related factors (local conditions). Characteristics of the surgical area determine different elements of the surgical intervention. Flow charts assist in determining the (i) surgical access, (ii) flap design, (iii) regenerative strategy, and (iv) suturing technique (*Figure 16*). Flap design and regenerative material application are primarily determined by the morphology of the intrabony defect, which is determined by the combination of clinical examination and intraoral radiographs.

This article however does not discuss surgical approaches, such as the single flap approach (90), the entire papilla preservation technique (91), or the non-incised papillae surgical approach (92), and the presented treatment strategies apply mostly to singular intrabony defects, and not for complex defects involving multiple teeth with various prognoses.

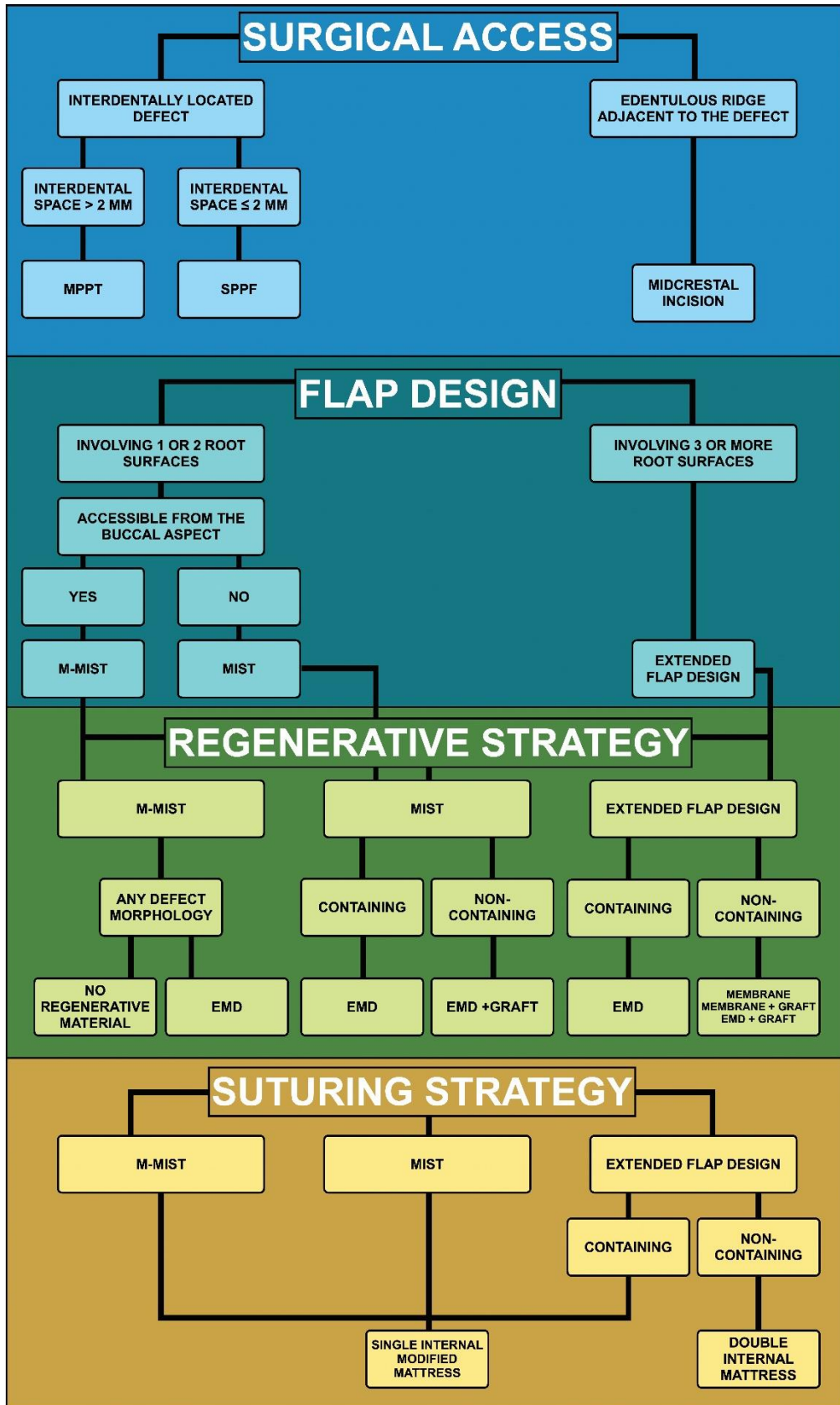


Figure 16.: Decision tree for the regenerative treatment of intra periodontal defects

1.3.2 Examination and classification of extraction defects

By their prognosis, teeth can be categorized into three classes: (i) favorable prognosis, (ii) questionable prognosis, and (iii) hopeless prognosis (irrational to treat). From a periodontal aspect teeth with attachment loss to the apex, perio-endodontal lesions, and reoccurring periodontal abscesses can be classified as irrational to treat (93). Extraction of these teeth is advised to avoid further progression of hard tissue lesions. However, in the aforementioned scenarios periodontal hard tissue conditions may be severely compromised, therefore treatment of extraction defects may be beneficial if prosthetic rehabilitation is planned with implant-supported fixed partial dentures (94). The complexity of extraction defects can be classified by the extraction-defect sounding (EDS) system introduced in 2005 by *Caplanis, Lozada and Kan* (95). According to the EDS classification, extraction defects can be divided into four categories based on hard and soft tissue conditions immediately after tooth extraction. Additionally, the paper recommends treatment protocols for each category.

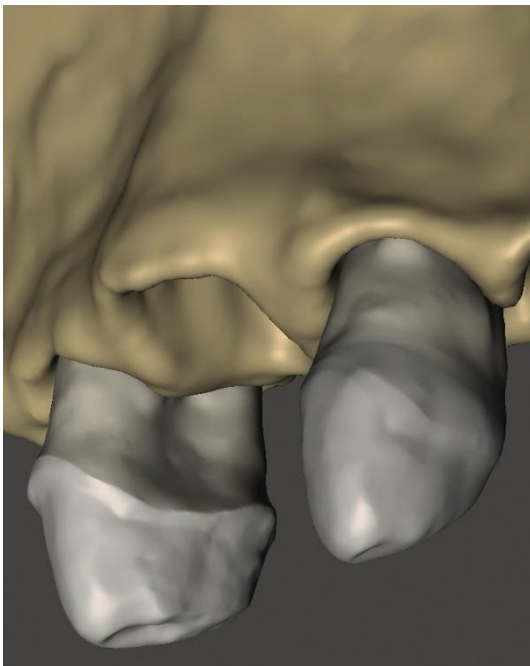


Figure 17.: EDS type 1

Characterized by a pristine, undamaged socket, with a thick periodontal- and soft tissue phenotype where the thickness of the buccal bone wall is 1 mm or more. These types of defects are ideal for immediate implant placement. In periodontally involved patients EDS type 1 defects rarely occur, due to previous periodontal tissue breakdown.

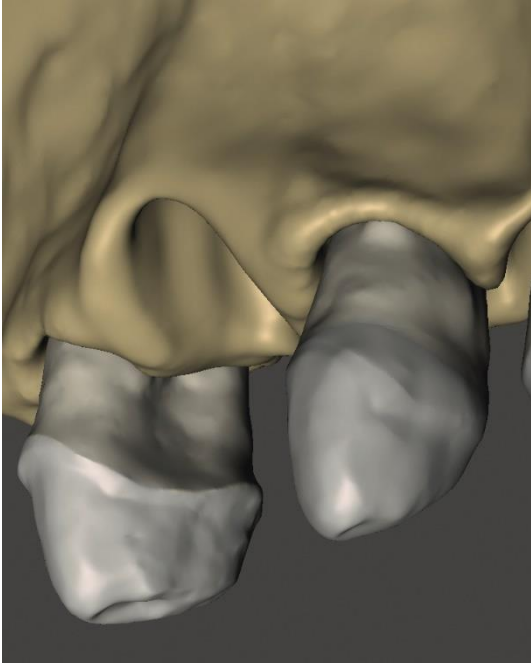


Figure 18.: EDS type 2:

Alveolar sockets with a mild (up to 2 mm) crestal bone loss and only one compromised bone wall. Either thin or thick phenotype with a buccal bone wall not thicker than 1 mm. Even though results are less predictable, if surrounding tissue conditions are adequate immediate implant placement can be applied.

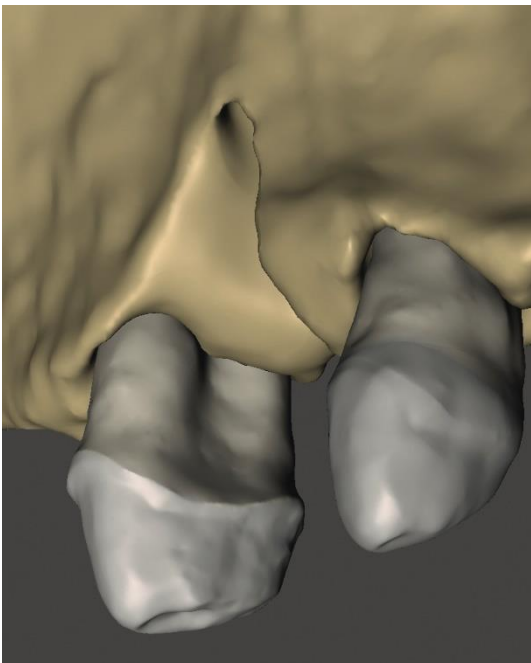


Figure 19.: EDS type 3

Alveolar sockets are moderately compromised with a vertical or horizontal hard and/or soft tissue resorption of 3–5 mm. Two of the bone walls are compromised, and defects may involve adjacent tooth surfaces. Immediate implant placement is no longer a treatment option; instead two-stage rehabilitation should be applied consisting of alveolar ridge preservation (stage 1) and late (conventional) implant placement (stage 2).

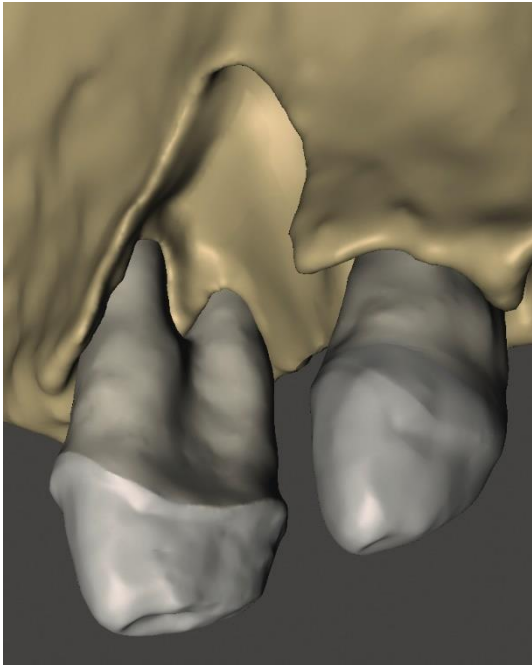


Figure 20.: EDS type

Severely compromised alveolar sockets with at least 5 mm vertical or horizontal hard and soft tissue loss. EDS type 4 defects occur in cases of advanced periodontal tissue breakdown with destruction of both the buccal and the palatal/ lingual bone walls. Bone loss can severely affect interproximal tissues. Due to the great extent of the baseline defect morphology authors recommend a three-staged approach: alveolar ridge preservation (stage 1), alveolar ridge augmentation (stage 2), and implant placement (stage 3).

According to the same principles, extraction defect characteristics can be assessed on CBCT scans following the extraction of hopeless teeth (96, 97).

1.4 Regenerative-reconstructive surgical treatment of intrabony periodontal defects and acute alveolar ridge defects following tooth extraction

1.4.1 Minimally invasive surgical procedures for the regenerative treatment of intrabony periodontal defects

Development in regenerative periodontal surgery has taken two major paths that have facilitated the evolutions of one another: (i) the introduction of new regenerative materials, and (ii) developments in surgical techniques. With the aim to enhance regenerative potential and to reduce postoperative patient morbidity, minimally invasive surgical approaches have been introduced. A major step in regenerative periodontal surgery was the introduction of enamel matrix derivatives (EMD) in 1997 (98, 99). Utilizing EMD, the formation of a new periodontal attachment has histologically been proven without the application of a barrier membrane (100, 101). Therefore, extended flap designs could be avoided in certain cases.

The first introduced surgical technique was the minimally invasive surgical (MIS) approach by *Harrel* developed in 1998 (102). The initial incision is made buccally and a split thickness flap is elevated at the lingual/ palatal aspect of the defect-involved interdental space. To increase visibility authors modified the MIS technique with the application of a videoscope (V-MIS), which provides 10–40x magnification and is equipped with a high-definition camera.

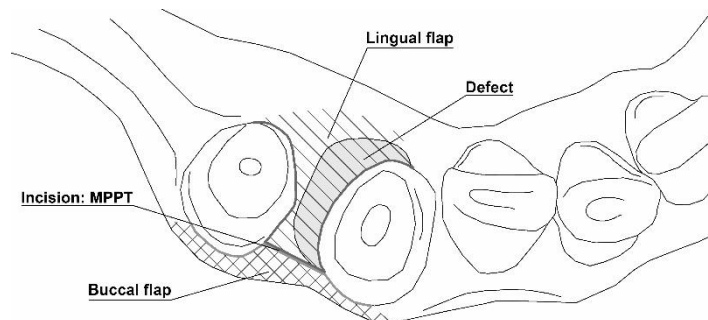


Figure 21.: Minimally invasive surgical technique

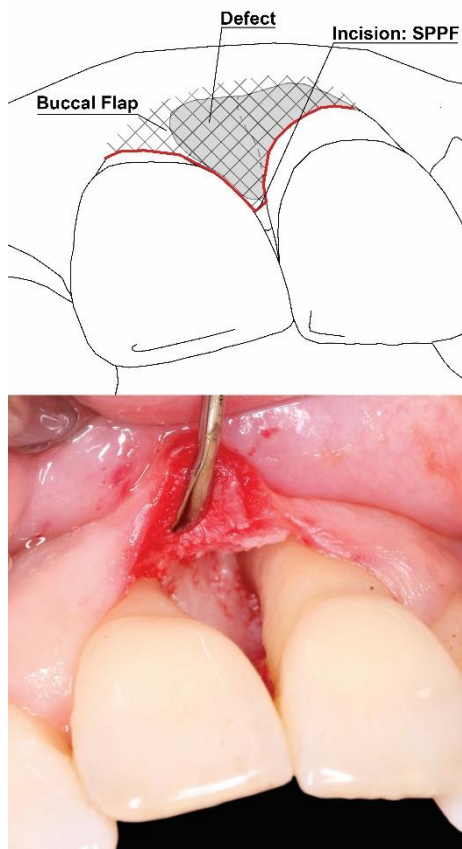


Figure 22.: Modified minimally invasive surgical technique

Initially this videoscope is used for the non-surgical visualization of renal calyces (103, 104).

Based on their papilla preservation techniques (105, 106) *Cortellini and Tonetti* introduced the minimally invasive surgical technique (MIST) that suggested limiting the mesio-distal extension of the initial incision to the defect-involved interdental area (*Figure 21.*). The flap is elevated on both buccal and lingual/palatal aspects, with only the marginal bone crest being exposed (107). The author further reduced the invasiveness of the technique with the introduction of the modified minimally invasive technique (M-MIST) (108), where a flap was elevated only on the buccal aspect (*Figure 22.*). However, the M-MIST technique is only recommended if the defect can be accessed completely from the buccal aspect (89).

Another unilateral flap design for the regenerative treatment of intrabony defects is the single flap approach (SFA) (90). Contrary to M-MIST, flap elevation depends on the most convenient access to the defect, therefore SFA can be performed either on the buccal or the lingual aspect (*Figure 23.*). Additionally, the mesio-distal extension of the initial incision is not limited to the defect-involved interdental area to ensure tension-free wound closure.

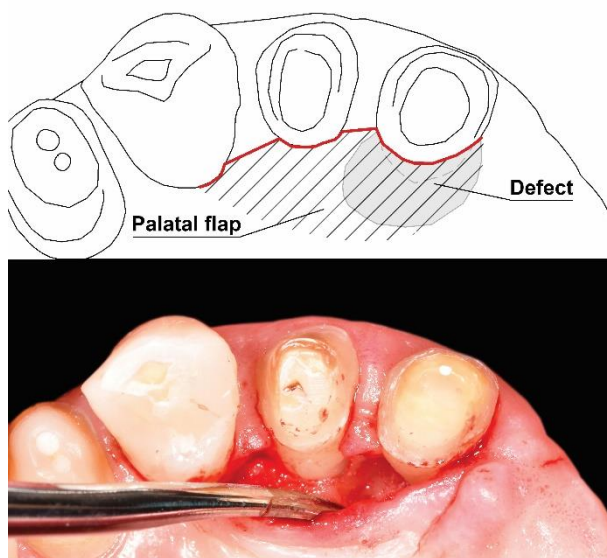


Figure 23.: Single flap approach

Other minimally invasive approaches include the entire papilla preservation

technique (EPPT) (91) and the non-incised papillae surgical approach (NIPSA) (92); these avoid incision of the papillae completely. In EPPT, defects are accessed from a buccally-placed vertical incision at the base of the papilla, whereas NIPSA utilizes an apical access.

Minimally invasive approaches combined with EMD alone or in combination with graft materials seem to offer significant clinical improvements in terms of probing depth reduction and clinical attachment level gain. However, compared to extended flap designs, invasiveness reduction, increased post-operative wound stability, reduced post-operative complications, and reduced patient morbidity can be achieved (109-111). In a three-way comparative clinical study *Cortellini and Tonetti* compared the efficacy of M-MIST with or without regenerative materials (no materials, EMD alone, EMD + bovine derived xenograft) (112). Significant probing pocket depth (PPD) reduction and clinical attachment level (CAL) gain was demonstrated in all three groups even when no regenerative materials were applied. No statistically significant difference could be demonstrated between the groups, suggesting that the increased post-operative blood clot stability achieved with M-MIST greatly affects periodontal wounds. The beneficial effects of a limited flap elevation were also demonstrated by *Azuma et al.* in an animal study (113). The authors compared the early healing capacity of periodontal intrabony defects treated with minimally invasive procedures and extended flap designs by histological evaluation performed at 1, 3, and 5 days after surgery. Histological and immunohistochemistry analysis demonstrated an accelerated shift from blood clots to granulation tissue, and an earlier, more significant increase of type III collagen at surgical sites treated with single flap periodontal surgery compared to conventional flap elevation, resulting in more efficient wound healing.

1.4.2 Alveolar ridge preservation

As was presented by *Araújo and Lindhe* in an experimental study, horizontal and vertical reduction of the alveolar ridge is a natural and inevitable consequence of tooth extraction (114). Histological analysis showed that dimensional alterations occurred during the first eight weeks following tooth extraction. Bone resorption occurred at both the buccal and

the lingual bone walls although it was more pronounced at the buccal than at the lingual aspect. The height reduction was accompanied by a reduction of horizontal ridge dimension. In cases of advanced extraction defect morphologies and EDS type 3 and type 4 defects (95), alveolar bone surrounding the teeth is already compromised prior to tooth extraction, therefore a more pronounced loss of hard tissue volume can be expected (115, 116). The alveolar ridge preservation (ARP) procedure is recommended as the first stage of a stepwise surgical rehabilitation (95).

The primary aim of ARP procedures is to prevent or reduce post-extraction hard tissue loss, and to enable dental implant placement without the need for extensive hard tissue augmentation (117). Many different approaches can be found in the literature with many systematic reviews summarizing the results (118, 119). In the majority of published articles, ARP is performed by filling the fresh extraction socket with autologous, alloplastic, xenogeneic, or synthetic non-resorbable particulate graft material. In a series of animal histologic studies, the application of different grafting materials was tested for ARP following single tooth extraction (120-122). It was demonstrated that grafting materials acted as scaffolds but did not interfere with natural healing processes and did not enhance bone formation. Width reduction of the edentulous ridge was found to be 35% in case of spontaneous healing, and significantly less – only 12% – following ARP with a bovine-derived xenograft material (Bio-Oss Collagen®, Geistlich AG, Wolhusen, Switzerland) (120). However, 5% of the xenograft particles were found to be encapsulated in connective tissue, mostly in the coronal portion of the alveolar socket. This ratio was found to be greater in a human study, being 14% (123). Histological analysis following ARP with various grafting materials demonstrated inferior hard tissue quality compared to native bone after spontaneous healing (118).

For these reasons (inferior tissue quality, residual graft particles) some authors suggested the application of barrier membranes without xenogeneic graft particles for ARP (115, 124).

1.4.2.1 Extraction site development technique (XSD)

In their article *Windisch et al.* compared results of a novel two-layer tunneled guided bone regeneration approach, called extraction site development (XSD) for ARP (test group) to spontaneous healing (control group). The authors examined EDS type 3 and type 4 extraction defects (115) around single-rooted teeth by re-establishing the missing buccal bone wall from a semi-closed approach. The XSD approach combines different aspects of the alveolar ridge preservation procedure described by *Lekovic et al.* (124) and the vestibular incision subperiosteal tunnel access (VISTA) presented by *Zadeh* (125).

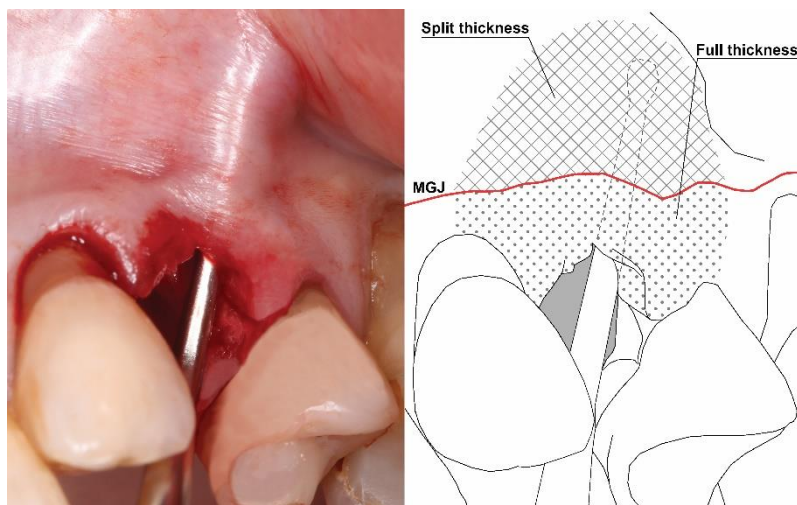


Figure 24.: Preparation of an envelope flap

After atraumatic tooth extraction, an envelope flap was prepared from the extraction socket towards the adjacent papillae (full-thickness to the mucogingival junction and split-thickness above) (*Figure 24.*).

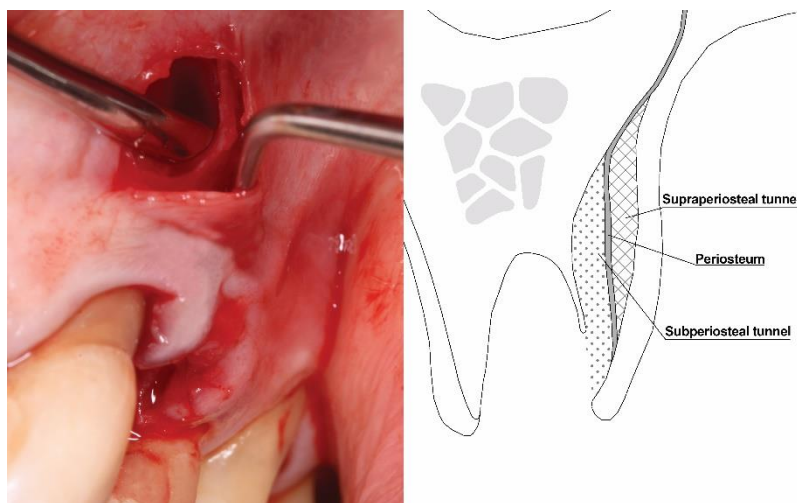


Figure 25.: Bilaminar buccal tunnel flap

From a mesially and a distally placed vertical incision, a bilaminar buccal tunnel was prepared over and under the periosteum (*Figure 25.*). The two tunnels separated by the periosteum were

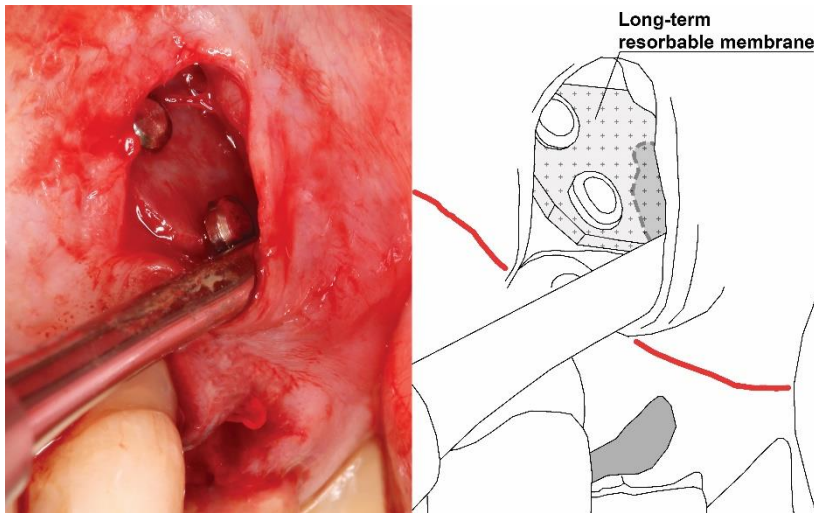


Figure 26.: Re-establishment of the buccal bone wall of the extraction socket utilizing a long-term resorbable membrane

connected with the previously prepared envelope.

After preparation of the tunnel-like flap, a long-term resorbable membrane. (Soft Cortical Lamina®, TecnoSS, Torino, Italy) was fixed under the periosteum by titanium pins to re-establish the missing buccal bone wall (Figure 26.).

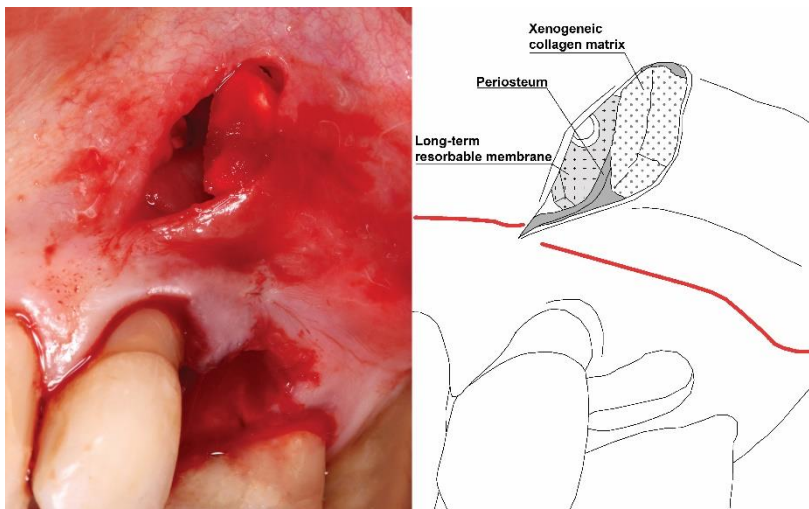


Figure 27.: Xenogeneic collagen matrix place in the suprapariosteal tunnel

A xenogeneic collagen matrix was fixed suprapariosteally to achieve an ideal soft tissue contour (Figure 27.). Application of non-resorbable xenogeneic graft materials was avoided; instead a resorbable collagen fleece was placed into the

extraction socket. The long-term resorbable membrane was utilized to re-establish the destroyed buccal bone wall at the extraction sites to increase the stability of an enlarged blood clot (Figure 28.). The authors reported that in the control group alveolar ridge dimensions were reduced approximately by 15%, whereas in the test group a 10% gain

was observed. Radiographically, newly formed hard tissues showed trabecularization similar to native bone. The authors emphasized the positive effect of an enlarged blood clot may not only have occurred directly at the edentulous site, but indirectly affected the defect-involved root surfaces of neighboring teeth as well (115).

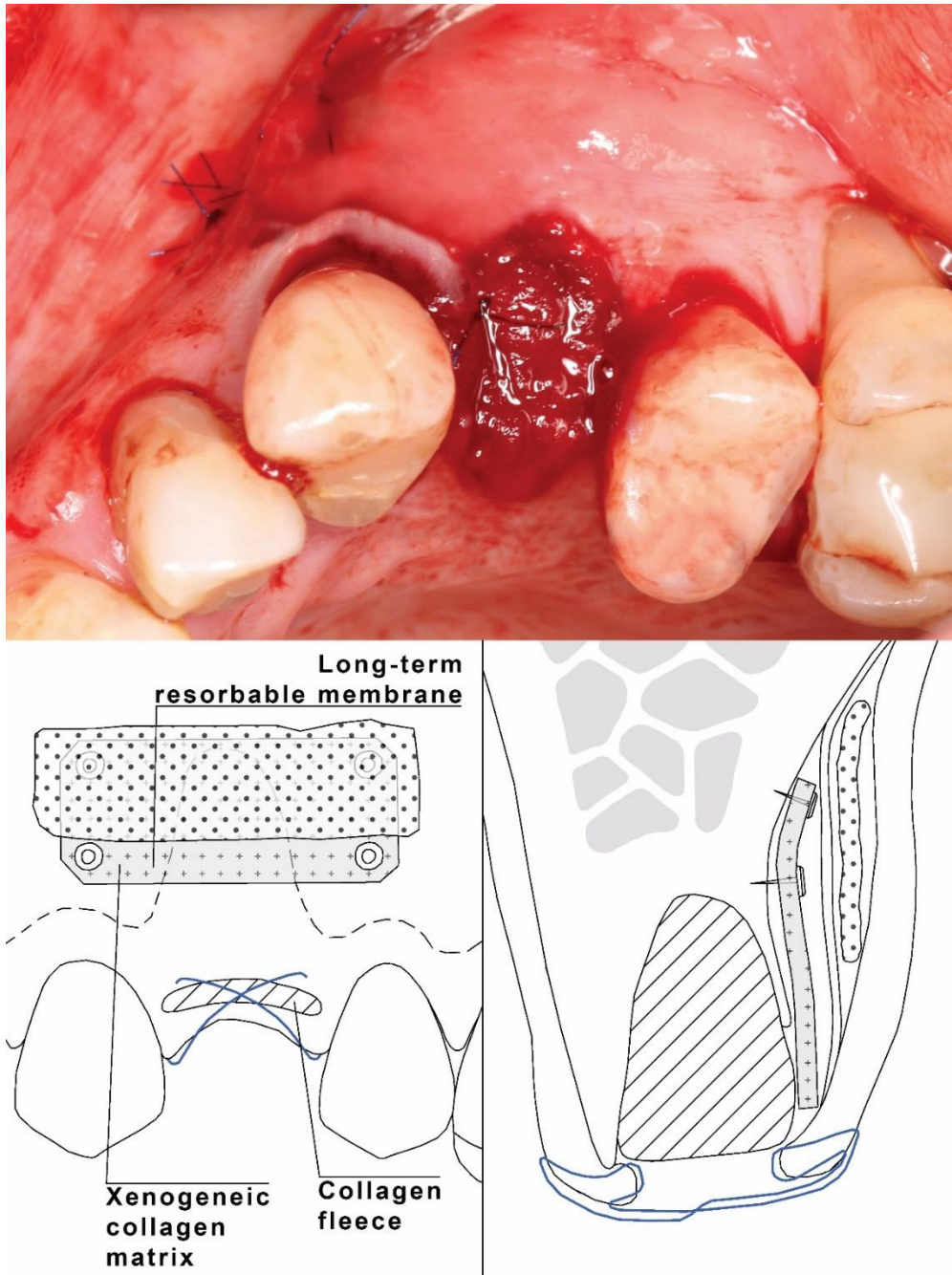


Figure 28.: Wound closure

1.5 Clinical and radiographic evaluation of surgical outcomes

1.5.1 Evaluation of periodontal regeneration following regenerative treatment

The primary objective of regenerative periodontal surgical procedures is the resolution of intrabony periodontal defects by achieving new periodontal attachment (126). The first clinical evidence of new periodontal attachment in humans was first demonstrated by *Nyman et al.* in 1982, where the formation of root cementum, periodontal ligaments, and alveolar bone was histologically proven. After a 3-month healing period the tooth was removed *en bloc* together with the buccal periodontium for histologic evaluation (127). However, due to ethical reasons human histology cannot be part of a routine postoperative assessment. Besides histological analysis, direct bone measurements, clinical examination and radiographic analysis can be applied to evaluate the performance of biomaterials and regenerative surgical approaches in the treatment of intrabony periodontal defects.

Histology provides the strongest evidence of new attachment formation and is the only method that can evaluate the composition and the quality of newly formed tissues. Articles have stated that if the formation of a new periodontal attachment is the result of regenerative treatment as has previously been proven histologically, it can be assumed that detected clinical and/or radiographical changes represent successful regenerative outcomes (128, 129).

Bone sounding is commonly used in clinical practice to directly assess periodontal bone topography under local anesthesia. Bone sounding overcomes limitations of clinical assessment methods such as probing force, probing angle, residual soft tissue inflammation, and oedema. Clinicians were less likely to underestimate the extent of periodontal defects. As with clinical examination, it is difficult to standardize the bone sounding process, therefore it is not recommended as a primary outcome variable to determine periodontal regeneration (130). Direct bone measurements can also be performed during a re-entry procedure. In this case linear measurements are taken at both the initial surgery and second surgical session to validate hard tissue changes directly

(131). This method still requires an additional procedure – with unnecessary surgical trauma – that can only be applied in controlled studies.

To validate outcomes after regenerative periodontal surgery, non-invasive methods should be applied. Clinical measurements (probing pocket depth: PPD, clinical attachment level: CAL, gingival recession: REC) (63) and radiographic evaluation on IRs (64) are used most frequently. As mentioned earlier, clinical measurement methods and conventional radiographic evaluation have their own limitations (70, 71, 77).

1.5.1.1 Evaluating outcomes of periodontal regenerative surgery on CBCT datasets

As with initial assessment of periodontal defect morphology, CBCT could also be a valuable tool for validating surgical outcomes after periodontal regenerative therapy. In a study, *Grimard et al.* compared the accuracy of clinical, periapical radiograph, and CBCT scan measurements for the assessment of periodontal bone level changes, concluding that CBCT measurements were significantly more accurate than the other two methods (77).

Besides linear measurements, *Nemoto et al.* assessed volumetric changes following regenerative periodontal therapy. A reference plane was determined perpendicularly to the long axis of the tooth at the most coronal part of the bone defect. Multiplanar reformation (MPR) of the CBCT dataset was performed based on the previously determined reference plane to generate an MPR view. Defects were manually delineated on each slice, and area was calculated. To determine baseline defect volume and residual defect volume at 12 months, the area of the bone defect on each slice was multiplied by the slice thickness (84). With this method initial defect volume and hard tissue fill could be calculated, however the article does not utilize 3D reconstructed models to visualize defect morphologies or postoperative healing dynamics.

Yan et al. analyzed hard tissue alterations in three dimensions following mandibular third molar coronectomy (88). CBCT scans were taken one day after surgery and 6 months later, and 3D models were generated for both datasets. Initial- and endpoint 3D models were aligned, and the two models were subtracted using Boolean operations. Linear and volumetric measurements were performed, and volumetric change both at the extraction

socket and at the distal aspect of mandibular second molars were calculated. The authors determined a 2 mm zone around the second molar to determine the volume of the periodontal hard tissue gain (132). Besides describing a high-quality protocol, the authors provided evidence of the tooth extraction affecting periodontal regeneration on neighboring teeth. However, the study has some clear limitations that must be addressed. Firstly, the 2 mm zone around the second mandibular molar to determine the volume of periodontal regeneration cannot be implemented for other teeth. Secondly, calculating the surface area of a new periodontal attachment might be a more objective outcome measure than calculating volumetric changes.

1.5.2 Clinical and radiographic evaluation of alveolar ridge alterations

To evaluate the effectiveness of ARP, linear intraoperative measurements and linear (133) or volumetric CBCT analysis can be performed. Volumetric CBCT analysis provides thorough understanding of ridge alterations in a non-invasive way.

In the aforementioned (in section *1.4.2*) comparative study, *Windisch et al.* evaluated the effectiveness of their extraction site development technique (XSD). Results were evaluated by comparing measurements on baseline and follow-up CBCT scans. The authors utilized I-CAT Vision® (KaVo Dental GmbH, Biberach an der Riß, Germany) to create orthoradial cross sections at the mesio-buccal, mid-buccal, and disto-buccal aspects of extraction sites, and images were further analyzed using ImageJ® software. On the pre- and postoperative CBCT scans, vertical and horizontal measurements were taken using a 1 mm² grid that was projected over the 2D images. The area of the alveolar ridge was also determined; teeth were excluded on the preoperative images. Three-dimensional evaluation however was not performed (115).

In their study, *Chappuis et al.* examined ridge alterations following tooth extraction on 3D virtual models. Even though an ARP procedure was not applied, this article analyzes 3D ridge alterations by comparing 3D models generated from pre- and postoperative CBCT scans. Rigid spatial alignment was done by anatomical landmarks to superimpose the CBCT scans, and differences were visualized by color-coded zones to indicate post-

extraction bone remodeling. This method primarily observes morphological alterations, and only linear measurements are performed (134).

In a more recent article, the authors analyzed tissue alteration after ARP, utilizing a bilayer polyethylene membrane. Hard tissue alterations were assessed similarly to the previously described method: by the superimposition of 3D models generated from the pre- and postoperative CBCT scans. In this article analysis was also performed at the soft tissues level by the spatial alignment of intraoral scans taken at different timepoints (135). In the previously mentioned articles 3D models did not contain separate anatomical structures, therefore the effects of tooth extraction and ARP on neighboring teeth could not be demonstrated, and neither of the articles calculated volumetric differences.

1.6 Summary

This part reviewed elements of a digital workflow applied in the virtual planning process of surgical procedures in periodontology and implant dentistry. For each step of the workflow, currently available technologies and methods found in the literature were summarized, pointing out their advantages and disadvantages. Many of the previously referenced articles utilized 3D technologies with the aim to (i) acquire detailed information on 3D morphologies of periodontal and alveolar ridge defects, (ii) achieve a thorough preoperative planning to reduce complications, and (iii) get a better understanding of healing mechanisms of various defect morphologies. Limitations of currently available methods have led to the development of the currently presented protocol.

2 OBJECTIVES

The most prominent limitation so far has been the inability to acquire realistic 3D models where all relevant anatomical structures i.e., teeth, alveolar bone, soft tissues, nerves, and arteries can be separated, and both the visibility and opacity of each element be adjusted. None of the previously mentioned articles utilized a “virtual patient” setup where teeth, alveolar bone, and soft tissues were separated, even though this would seriously benefit the previously mentioned applications.

The objective of this thesis was therefore to present a novel method for 3D virtual model acquisition to aid treatment planning, surgical intervention, and postoperative evaluation following regenerative periodontal surgery and alveolar ridge preservation.

The “Methods” chapter can be divided into two major sections. In the first part, elements of a **model acquisition method** are detailed that allow practitioners to generate realistic virtual 3D models where relevant anatomical structures are separated to represent the actual and clinical situation realistically. In the second part, various **clinical applications** within the framework of the digital workflow already discussed are presented which are possible to perform due to the acquired virtual models. These include:

- three-dimensional visualization of intrabony periodontal defects prior to regenerative surgical treatment to aid the decision-making process
- presentation of a completely digital workflow in the regenerative-reconstructive treatment of complex periodontal-alveolar ridge defects
- subtraction analysis of volumetric and morphological hard tissue alterations following ARP

3 METHODS – Part I: Virtual model acquisition

The most important aspect of this thesis is the novel virtual model acquisition method which combines radiographic image processing and computer aided design techniques. Contrary to most of the articles referenced in the “Introduction” chapter, this method can be executed using only free software and there is no need to spend large amounts of money to carry out the protocol. The software that was used for radiographic image processing is the open-source medical image processing software platform 3D Slicer (<https://www.slicer.org/>) (136). The software used for CAD modeling is the prototype design software developed by the company Autodesk (San Rafael, California, USA) called Meshmixer® (<https://www.meshmixer.com/>).

The major steps of the model acquisition method are: (i) semi-automatic segmentation of the CBCT dataset, (ii) spatial alignment of the CBCT dataset and IOS, and (iii) CAD modeling (137).

3.1 Semi-automatic segmentation method

The primary reason why thresholding segmentation algorithms produce poor results in dental CBCT scans is the extensive amount of metal artifacts (26, 27) and scatter visible on the images, compromising the accuracy and trueness of 3D models (41). To overcome the limitation of thresholding segmentation, this method utilizes various semi-automatic and manual segmentation tools found in the inventory of 3D Slicer.

Relevant anatomical structures are highlighted separately by generating 3D binary labelmap volumes on the CBCT dataset. A binary labelmap indicates whether a specific voxel is inside (1) or outside (0) the generated structure. Three-dimensional closed surface representations are automatically rendered from binary labelmaps generated on the dataset (138).

The semi-automatic segmentation process can be divided into three major phases: (i) delineation of anatomical structures, (ii) morphological contour interpolation, and (iii) segmentation smoothing. Different anatomical structures must be segmented separately

and are represented by different binary labelmaps to achieve a realistic result, therefore the previously mentioned steps need to be carried out for all teeth and the alveolar bone separately (137).

3.1.1 Delineation of anatomical structures

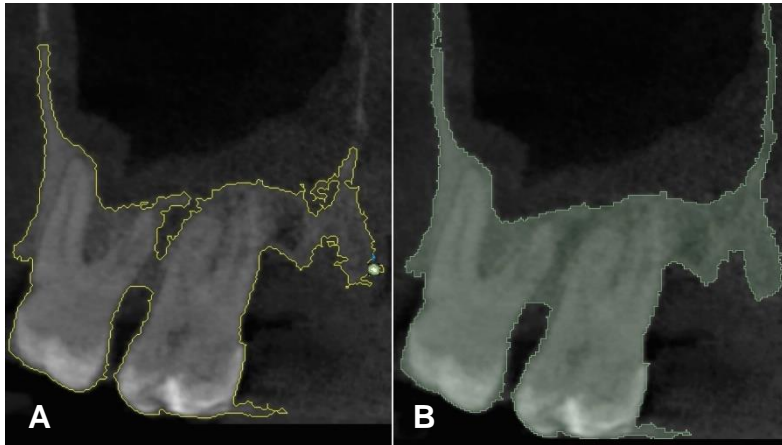


Figure 29.: *Outlining the alveolar bone using level tracing*
A: *Dragging the cursor to the perimeter of the alveolar ridge;*
B: *Generated labelmap*

In this phase a binary labelmap is generated for one specific anatomical structure. These initially created labelmaps will become the input data for segmentation tools in later steps. Delineation of anatomical structures is performed with the “**Level Tracing**” tool

found in the “*Segment editor*” module of 3D Slicer (*Figure 29.*). This tool traces a level curve from a seed point, and pixels within this level curve are labeled within the outlined region (independently from their intensity value) and will be highlighted. This tool can be considered as a basic edge detector.

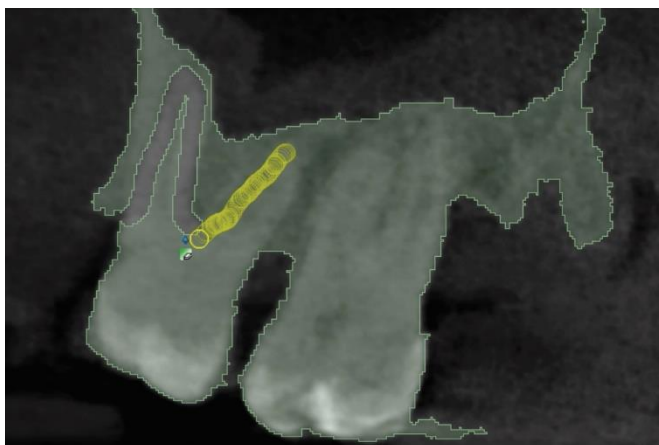


Figure 30.: *Erasing teeth from the labelmap representing the alveolar bone*

In practice, the operator must drag the cursor to the perimeter of the desired anatomical structure. A yellow line will indicate the boundary of the area, and if the result is satisfactory the binary labelmap for that specific slice can be generated. On slices where other anatomical structures are also visible (e.g., teeth), the algorithm

often fails to outline only the desired area, due to the similarity in voxel intensities. Therefore, in these instances results will have to be corrected with the help of manual segmentation tools i.e., “**Paint**” and “**Erase**” (*Figure 30.*). For example, if teeth are also outlined together with the bone, the perimeter of the teeth must be traced manually and the labelmap has to be erased in the area of the teeth(137).

To reduce segmentation time, this type of semi-automatic delineation must only be performed on every 5th to 10th slice (depending on slice thickness) (*Figure 31.*); the missing labelmaps will be calculated by a morphological contour interpolation algorithm (139).

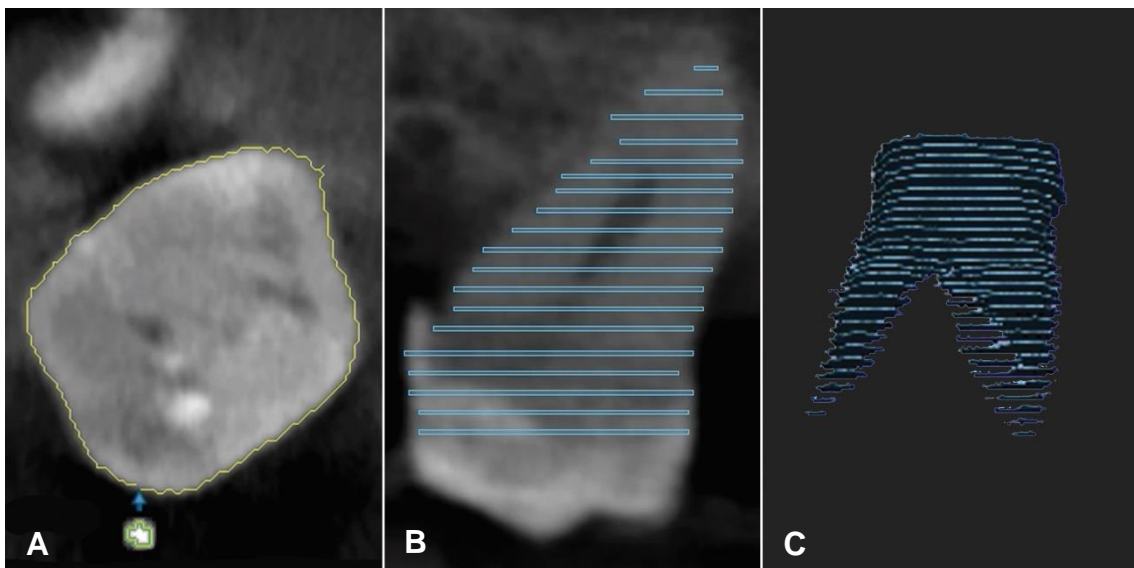


Figure 31.: Level tracing segmentation of teeth

A: outlining the perimeter on axial slices; B: Sagittal view of generated labelmaps, C: 3D view of generated labelmaps

3.1.2 Morphological contour interpolation

The morphological contour interpolation algorithm in 3DSlicer, “**Fill between slices**” is an iterative interpolation tool (140, 141). The algorithm analyzes the shape of the input binary labelmaps generated in the previous step, computes the transition sequence between corresponding input labelmaps, and generates new labelmaps on interim slices (*Figure 32.*). It must be noted that the algorithm does not analyze pixel gray values or anatomical structures visible on slices – just the basic shape of the already-created binary

labelmaps. This type of iterative interpolation is especially useful in medical imaging, although it can be applied in many other scientific fields as well (137).

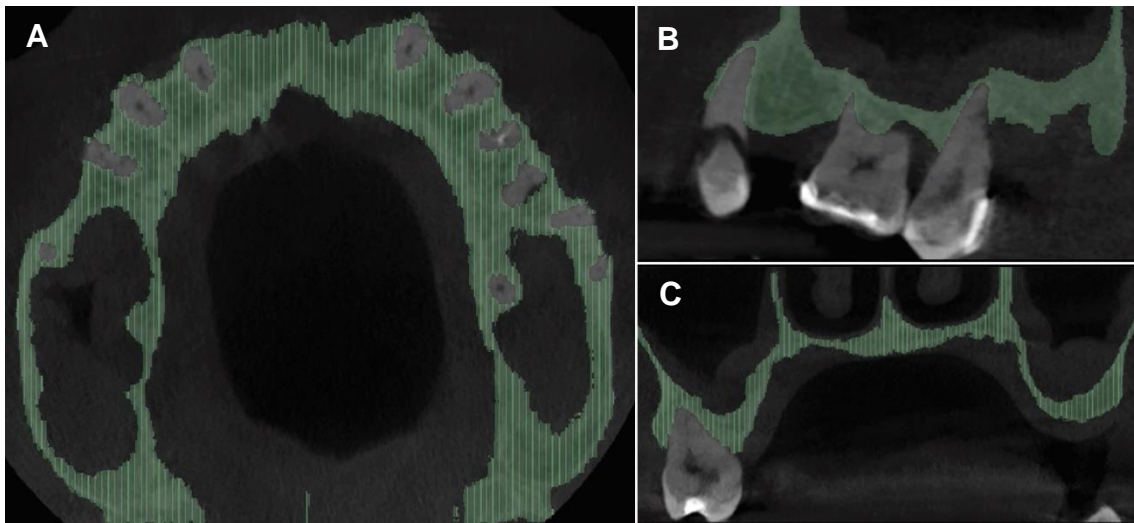


Figure 32: Morphological contour interpolation of generated labelmaps **A:** Axial view, (light green lines indicate generated labelmaps); **B:** Sagittal view; **C:** Coronal view

3.1.3 Smoothing segmentation

With the previous two steps a raw version of the 3D model can be acquired, however due to occasional errors the model appears pixelated and rough at this point, therefore smoothing must be performed (142).

Smoothing can be done at one of two stages:

- the 3D closed surface representations of binary labelmaps can be smoothed with tools found in 3DSlicer
- the exported STL file of the segmentation can be smoothed in Meshmixer®

Binary labelmap volumes are the main input/output format of tools in the 3D Slicer inventory. Due to the conversion algorithms, changes made to labelmaps are visualized in real time on the 3D surface representations as well. In this case, modifications are done to the labelmaps and not to the 3D models directly (*Figure 33.*), whereas in the case of STL files alterations are made to the 3D model directly. The second difference is that the amount of smoothing can easily be controlled on the visible CBCT images in 3DSlicer, however this feature is not available in Meshmixer®.

It is advised to carry out the majority of the smoothing at this stage to avoid the loss of information due to occasional over-smoothing at later stages.

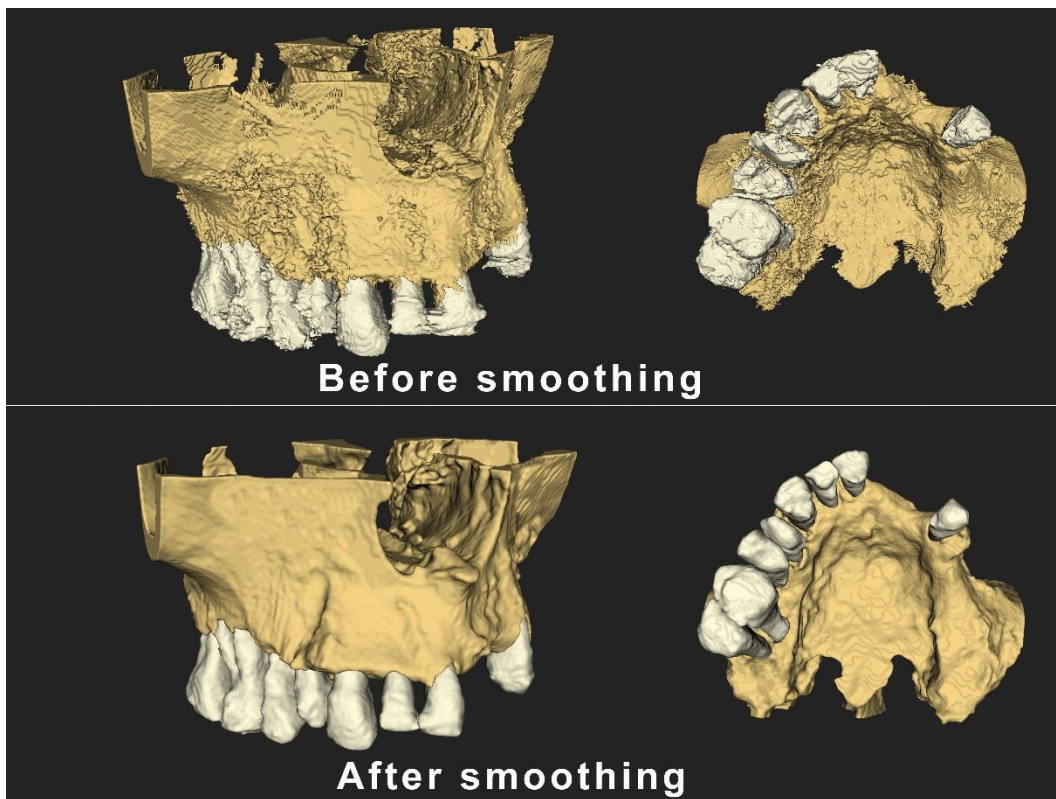


Figure 33.: Before and after smoothing

The “**Smoothing**” tool in 3DSlicer has various parameters that have to be adjusted to achieve an ideal result. The tool is capable of either local smoothing with the application of a brush, or generalized smoothing where the entire model will be smoothed equally. The smoothing method and amount of smoothing can also be adjusted. For this protocol the median smoothing method was selected. It removes protrusions and fills small holes at the same time, although other methods can be implemented in the future as well. It is advised that in areas where important small details (e.g., thin marginal bone crest, knife-edge alveolar ridge) are visible the amount of smoothing should be reduced (142).

3.2 Spatial registration of CBCT dataset and intraoral scan

Three-dimensional models of hard tissues can be acquired from CBCT datasets, however soft tissues are not visible on CBCT images. To utilize a true “virtual patient” setup the inclusion of 3D soft tissue models is also necessary. A combination of CBCT datasets and IOSs is frequently used in various fields of dentistry (1, 2, 4, 6, 135). Most of the previous articles did not combine the two 3D models (segmented CBCT models and intraoral scans) into one hybrid model that contains 3D data of all relevant structures.

It must be noted that incorporation of an intraoral scan has not always been utilized in the articles that describe the application of the current model acquisition protocol. Even though inclusion of IOS data would provide a better understanding of tissue alterations. A primary determinant factor in treatment planning and the evaluation of surgical outcomes in periodontology and implant dentistry is periodontal/alveolar bone topography. Therefore, not all of the currently presented articles describe the application of IOSs.

Nevertheless, spatial alignment of dental CBCT data and IOSs is most frequently done by the selection of identical anatomical landmarks between the two models (143, 144). In 3D Slicer, installation of the “Image Guided Therapy (IGT)” extension (145) is necessary for spatial registration of the two models. The basic principle is similar to other anatomical landmark-based registration methods (146, 147); identical points are selected on cusps and incisal edges of teeth. Two lists of fiducial markers must be created. The first list (“From”) is created on the moving object, which is usually the IOS. The second

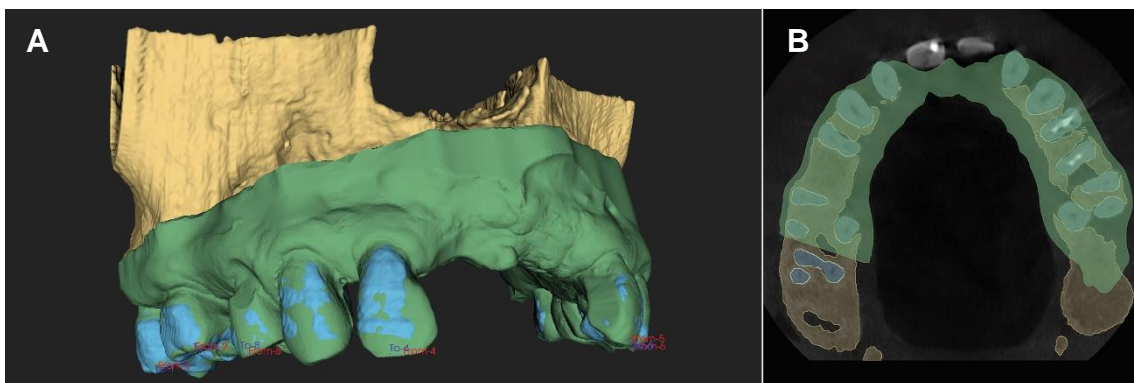


Figure 34.: Alignment of the segmented 3D model and IOS

A: 3D view; selected identical points are visible in red and blue; **B:** 2D (axial) view

list (“*To*”) is created on the fixed object, which is usually the CBCT dataset (*Figure 34*). Identical points are more easily marked on cusps and incisal edges of teeth, although in high quality CBCT scans markup points can also be placed on the mucosa (e.g., palatal rugae) (148). The more identical points can be selected, all equally spaced along the entire dental arch, the greater the accuracy of the registration (149). For instance, spatial registration of a CBCT scan and IOS with only a single tooth gap in the dental arch is more easily carried out than in cases of large edentulous areas (especially in the molar region) or a totally edentulous arch. To enhance alignment in these cases, the authors have suggested the use of scanning templates with artificially placed fiducial markers (150, 151). To further enhance the alignment, it is advised to place cotton rolls between the upper and lower teeth (2). This way, large amounts of scatter occurring at the line of occlusion can be avoided and a clear image of crown topography can be acquired. Occasional misalignments can be corrected by hand.

After this step, both the segmented 3D model of hard tissues and the aligned 3D model of the IOS have to be exported as an STL file for further refinement in Meshmixer® (137).

3.3 CAD modeling - final virtual patient setup

At this point the model is already suitable for virtual planning, and the majority of methods described by this article execute virtual planning at this stage. Three-dimensional hard tissue models with superimposed IOSs can be considered as a virtual patient setup (36, 144, 152), however with further CAD modeling the level of reality can be increased significantly. Final model composition is achieved by a series of Boolean operations (153) that in computational modeling can be described as the interaction of two or more polygonal objects. The Boolean operations used most frequently in CAD modeling are: **Boolean union**, **Boolean subtraction**, and **Boolean intersection** (Figure 35.)

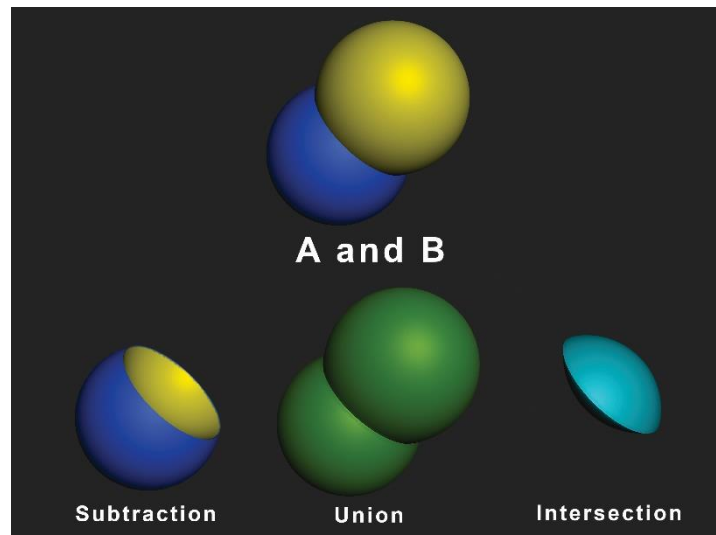


Figure 35.: Demonstration of basic Boolean operations

(154).

3.3.1 Replacement of tooth crowns

Coronal portions of teeth appear very radio dense on CBCT scans, therefore they produce a large amount of artifacts, especially if the patient has any prosthetic restoration (155, 156). Metal artifacts produced by prosthetic restorations affect the accuracy and trueness of tooth crowns on 3D models (157). For this reason, authors have previously suggested replacing the coronal portion of 3D tooth models derived from CBCT scans with the crowns of teeth present on IOSs (158, 159). Both articles primarily aimed to determine the accuracy of the replacement with in vitro methods and did not describe an exact CAD modeling process.

Both of the exported STL files are opened with Meshmixer®, and following initial inspection the crowns of teeth can be separated from the rest of the model captured by the intraoral scanner. By selecting the triangles of the STL file that represent the crowns of teeth, the selected and unselected portions can be separated into open surface objects. CAD modeling is easiest on closed surfaces, therefore holes must be closed. Crowns of teeth separated from the IOS can now be merged with the 3D models of teeth acquired by CBCT segmentation with **Boolean union** (153, 154) to create hybrid tooth models (crown from IOS, root from CBCT) (*Figure 36.*).

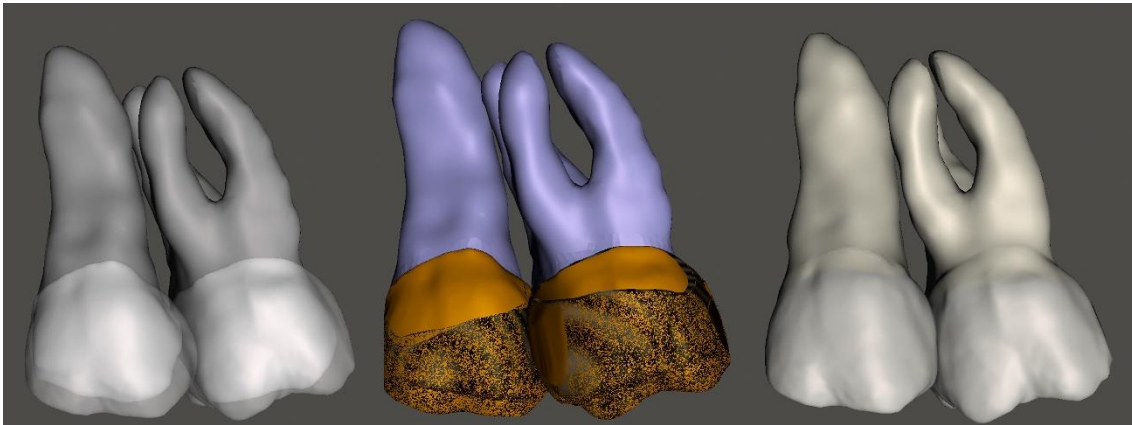


Figure 36.: Replacement of tooth crowns

3.3.2 *Soft tissue CAD modeling*

To realistically emulate gingival and alveolar soft tissue dimensions, a series of **Boolean subtractions** (153, 154) have to be executed. After separation of teeth, the original IOS without teeth becomes the soft tissue model. Firstly, the bone model must be subtracted from the soft tissue model; this way the soft tissue layer is on top of the bone model and represents the true clinical situation. In the second step, hybrid models of teeth need to be subtracted from the soft tissue model to emulate the marginal thickness of the gingiva (*Figure 37.*).

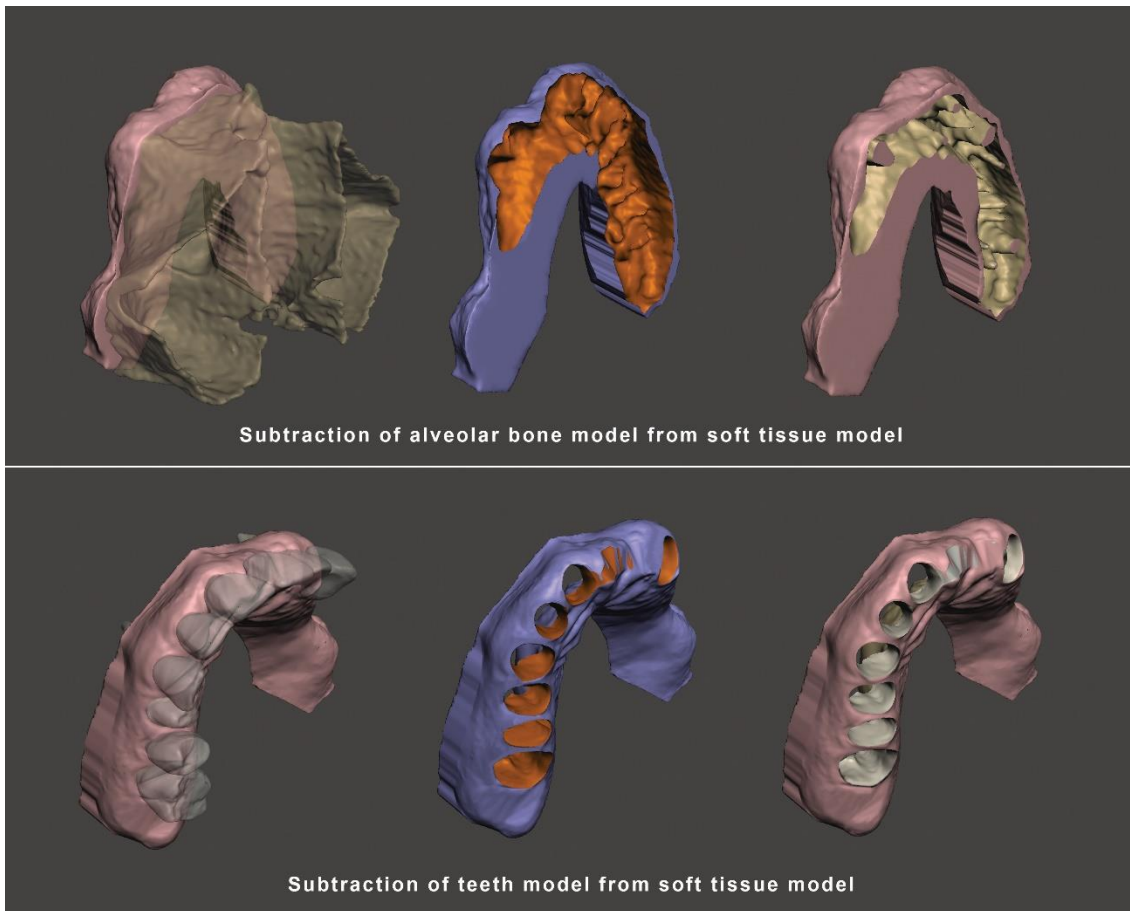


Figure 37: Series of Boolean subtractions for the construction of the soft tissue model

This type of model composition replicates the clinical situation virtually and allows for the 3D treatment planning of each individual step of surgical procedures i.e., initial incision, flap design and elevation, debridement, application of regenerative materials, and wound closure. A similar method has not yet been described elsewhere in the literature for virtual model acquisition.

The STL file format is not able to represent the color of the object, thus all STL files appear white (or colorless). To make the models appear more realistic, surfaces can be colored with brushes. In order to visualize colors, the 3D digital models must first be converted to the OBJ (object) file format developed by Wavefront Technologies (*Figure 38.*) (137).

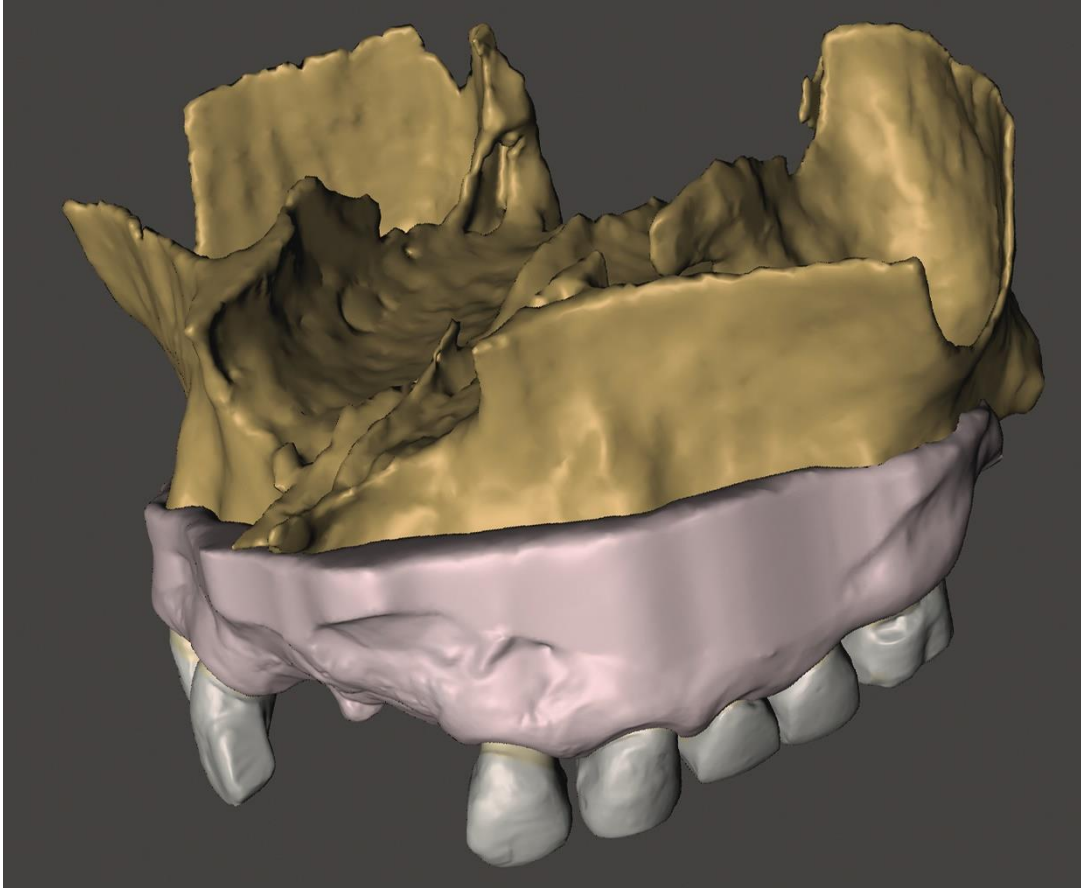


Figure 38.: Final virtual hybrid model

3.4 Summary

In this part of the “Methods” chapter, the methodology for 3D virtual model acquisition was presented with the aim to overcome the limitations of previously existing methods found in the literature. Basic principles of applied image processing and CAD modalities were introduced. With the developed semi-automatic radiographic segmentation method different anatomical structures were reconstructed separately. In addition to 3D hard tissue models derived from CBCT scans, IOS data were also included by utilizing anatomical landmark-based spatial registration (rigid model transformation). CAD modeling allows the composition of a virtual patient setup that depicts anatomical structures in 3D with a high level of reality. Regardless of the clinical application, the model acquisition stages are the same, therefore the presented method can be utilized for many different clinical applications.

4 METHODS – Part II: Clinical applications

4.1 Three-dimensional visualization of intrabony periodontal defects for regenerative surgical treatment planning

It was mentioned previously (in section *1.3.1*) that the diagnostic and treatment planning process in the case of specific intrabony periodontal defect morphologies can be challenging with conventional periodontal diagnostic methods, and to overcome their limitations the application of a CBCT scan for diagnostic purposes has been proposed (74-76, 78, 79, 82, 83, 160) with some articles even suggesting the application of 3D virtual models (1, 84-88). However, the majority of these articles utilized automatic, thresholding segmentation techniques for the 3D reconstruction of CBCT datasets. With the previously presented (in section *3.1.1*) semi-automatic method, teeth and alveolar bone can be segmented separately, therefore boundary and periodontal defect morphology can be visualized more clearly.

In our article, our aim was to utilize 3D virtual models for the treatment planning of minimally invasive periodontal surgeries and to evaluate the accuracy of the virtual models by comparing digital measurements to direct intrasurgical measurements (161).

4.1.1 Patient selection and radiographic imaging protocol

Four patients with six intrabony periodontal defects around three single-rooted teeth and three multi rooted teeth were enrolled in this retrospective case study. Patients were diagnosed with Stage III/Grade B periodontitis (65).

Exclusion criteria were

- Patient related factors: (i) previous irradiation therapy in the maxillo-facial area, (ii) uncontrolled diabetes, (iii) systemic steroid treatment, (iv) systemic bisphosphonate treatment, (v) pregnancy, (vi) smoking, (vii) insufficient oral hygiene (full mouth plaque score (FMPS) > 25%), (viii) high levels of inflammation (full mouth bleeding score (FMBS) ≤ 25%).
- Site related factors: (i) circumdental defects, (ii) endo-periodontal lesions, (iii) periodontal bone loss beyond the apex, (iv) Grade III furcation defects.

Two months after cause-related periodontal therapy, CBCT scans were taken with I-CAT FLX® (KaVo Dental GmbH, Biebrach an der Riß, Germany) and clinical parameters (PPD, REC, CAL, FMBS, FMPS) were registered utilizing a UNC-15 periodontal probe.

Imaging parameters:

- voxel size: 30 µm
- tube current: 36 mA
- anode voltage: 120 kV
- FOV: 16 cm × 8 cm

The enrolled patients were under periodontal treatment at the Department of Periodontology, Semmelweis University. A large FOV was selected to plan not just periodontal treatment, but also the entire surgical rehabilitation process for the dentition, including alveolar ridge preservation, alveolar ridge augmentation, sinus floor elevation, and implant placement procedures. The large FOV was compensated for by the relatively low image resolution in order to reduce radiation dose (22, 23). Although image resolution had to be compromised, the segmentation process could be executed regardless.

4.1.2 Radiographic image processing

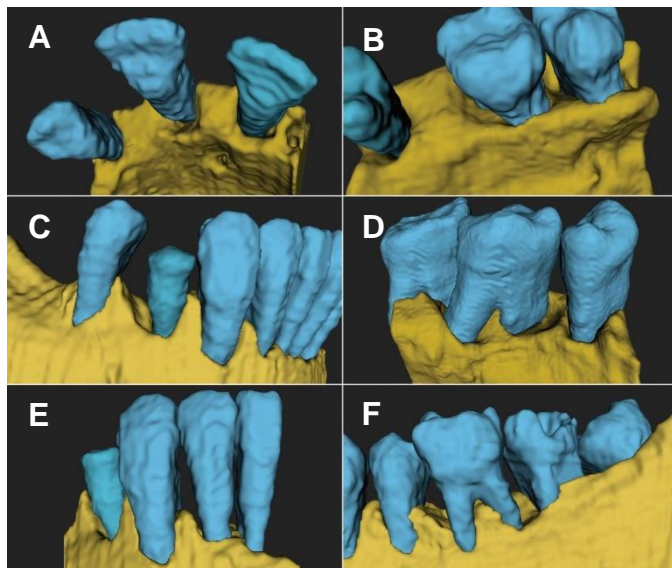


Figure 39.: Three-dimensional models of the selected six cases

A: Three-wall combined defect; **B:** Two-wall intrabony and grade II furcation involvement; **C:** One-wall intrabony defect; **D:** One-wall intrabony defect and mesial grade II furcation; **E:** One-wall intrabony defect; **F:** One-wall intrabony defect and lingual grade II furcation involvement

Acquired CBCT scans were processed according to the segmentation method presented in section 3.1.1. To reduce segmentation time, only the surgical areas were reconstructed in 3D. In this study intraoral scan data were not included, thus only hard tissue dimensions could be assessed (*Figure 39.*).

4.1.3 Surgical procedure

Minimally invasive surgical procedures aim to improve blood clot and wound stability to enhance regenerative potential and to reduce patient morbidity by limited flap elevation (113). The biggest disadvantage of a minimal flap design is the limited intraoperative visibility, therefore 3D visualization of the surgical area prior to and during surgery is extremely useful. 3D models aid intraoperative navigation during defect debridement and application of the regenerative material.

Periodontal defects were treated with unilateral flap designs, either a single flap approach (90) or a modified-minimally invasive surgical technique (108). The appropriate flap design and point of access (buccal or palatal/lingual) were determined on the 3D models based on the most convenient access. Based on literature data (110, 112) only an enamel matrix derivative (EMD) (Emdogain®, Straumann, Basel, Switzerland) was applied. Tension-free wound closure was achieved by the suturing technique described in the original articles of M-MIST (108) and SFA (90) respectively (*Figure 40.*). Sutures were removed after 14 days. Patients were instructed to avoid mechanical cleaning in the surgical area until suture removal.

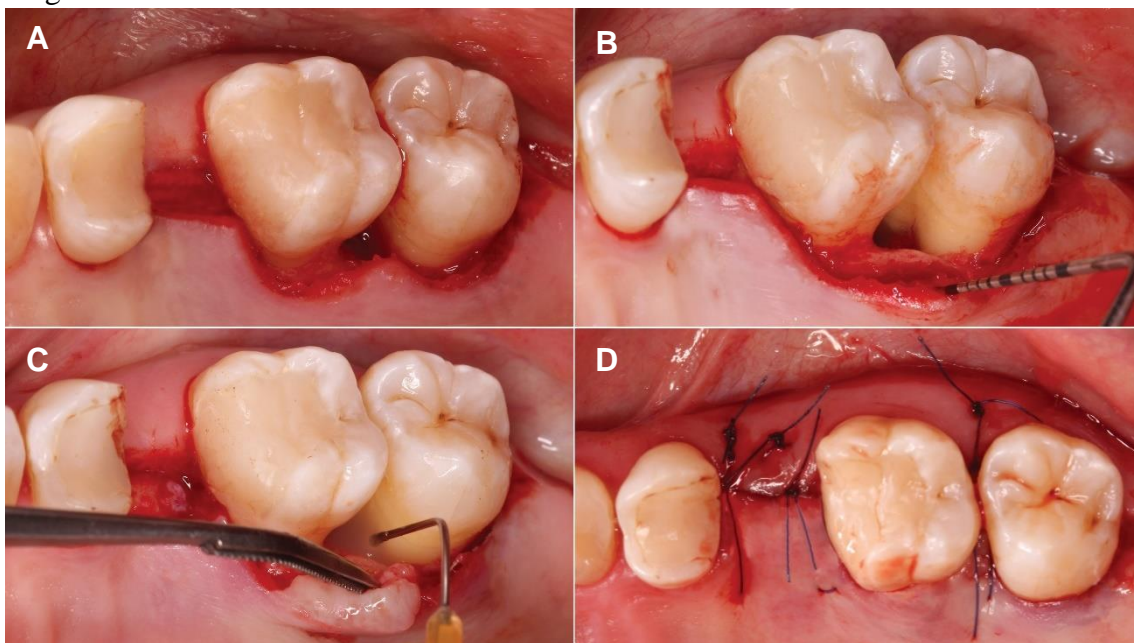


Figure 40.: Regenerative surgical treatment utilizing a single flap approach
A: Initial incision and palatal flap elevation; **B:** Intraoperative visualization of the defect morphology; **C:** Application of enamel matrix derivate; **D:** Wound closure

4.1.4 Outcome variables

4.1.4.1 Primary outcome measure - Comparison of intrasurgical and digital measurements

The primary outcome was to assess the accuracy of the 3D virtual models. Following flap elevation, direct intrasurgical measurements were taken to assess periodontal bone topography. The vertical distance from the marginal bone crest to the base of the defect (intrabony component depth: **INTRA**) and the horizontal distance from the root surface to the most coronal point of the bone crest (root surface-bone crest distance: **WIDTH**) was registered intrasurgically (131). After the surgical intervention, similar linear measurements were

performed on the 3D virtual models utilizing the “**Line markup**” tool in 3D Slicer. Contrary to other studies that measure distance on CBCT datasets, in this examination linear distances were also measured on the three-dimensional models (*Figure 41.*). Therefore, it was possible to reproduce intraoperative measurements digitally.

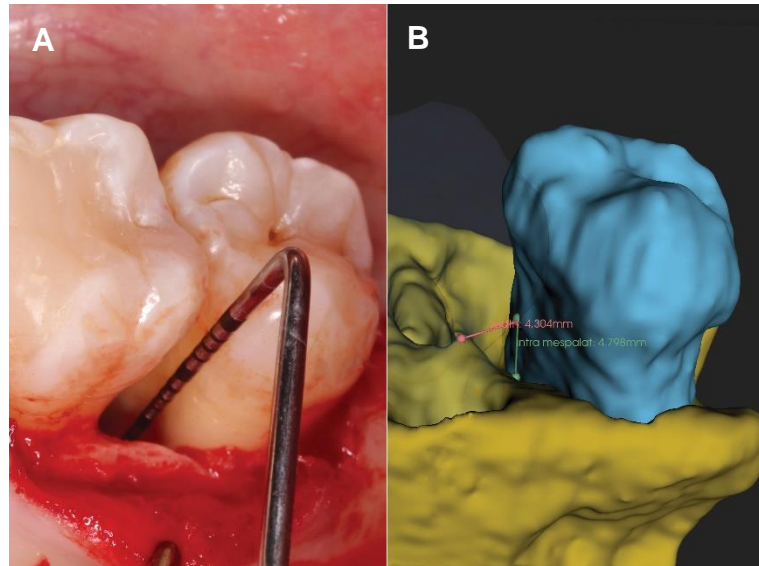


Figure 41.: Intraoperative and digital measurements

A: Intraoperatively measure depth: 5 mm; **B:** digitally measured depth: 4.79 mm

4.1.4.2 Secondary outcome measure - Preoperative defect assessment

A secondary outcome was to investigate whether specific defect characteristics could be determined with conventional diagnostic methods (intraoral radiographs and clinical measurements) and with the application of the 3D models; these were compared to the intraoperative defect morphology assessment.

The following parameters were assessed (162-164):

- **general morphology of the defect:** (i) supraosseous (horizontal); (ii) intraosseous (vertical); or (iii) combined
- **number of affected root surfaces:** one; two; three; or four
- **number of bony walls:** (i) tree-wall defect (self-contained); (ii) two-wall defect or interdental crater; (iii) one-wall defect (non-contained); or (iv) circumferential crater
- **furcation involvement and grade of the furcation defect:** (i) grade I; (ii) grade II; or (iii) grade III

The aforementioned characteristics are defect-related factors that determine surgical flap design and the type of the applied regenerative strategy (89). In each case, if at least three of the four characteristics were determined correctly, the diagnosis was considered accurate (*YES*), and if two or fewer characteristics were determined correctly the diagnosis was considered inaccurate (*NO*). This relatively subjective evaluation method was utilized to support the clinical feasibility of the newly introduced diagnostic modality.

4.1.5 Data analysis

The focus of the statistical analysis was on the differences between intraoperative and digital measurements. Intrasurgically and digitally measured values were expressed as mean value \pm standard deviation. One sample t-test was performed with a significance level (P) set to 0.001. Bland Altman analysis was performed to determine the agreement between the two measurement values. Statistical analysis was performed in SPSS Statistics® (IBM, Armonk, New York, USA) and Excel® (Microsoft, Redmond, Washington, USA).

4.2 Virtual planning and volumetric evaluation in the regenerative-reconstructive surgical treatment of a complex periodontal defect – Case presentation

In the article summarized in the previous section, 3D models were only utilized for surgical treatment planning. However, as was found in the literature, with the segmentation and comparison of both pre- and postoperative CBCT scans the result of the surgery can also be analyzed in three dimensions.

In a recently published case presentation article, 3D virtual models acquired by CBCT segmentation were utilized both for treatment planning and for postoperative evaluation with the integration of IOS data as well (165).

4.2.1 Patient selection, defect description

The treatment of a 53-year-old male patient diagnosed with Stage III/Grade B periodontitis (65) was presented. In the case report the regenerative-reconstructive surgical treatment of complex periodontal defects involved the upper left premolars and molars, which were treated with a novel stepwise approach (*Figure 42.*).



Figure 42.: Intraoral periapical radiograph of the upper left quadrant

Subcomponents of the defect:

- Around the two premolars circumferential intrabony defects developed involving all four surfaces of the roots. Circumferential defects were separated by a small bony peak
- Around tooth 26 a vertical perio-endodontal defect extending beyond the apex developed, causing grade III furcation involvement (164) of the tooth
- The extensive periodontal lesion also involved the mesial surface of tooth 27 causing an approximal grade II furcation defect around the tooth (164).

Of the four teeth, 26 was prognosed as “hopeless”, and teeth 24, 25, and 27 were deemed “questionable” (93). Due to the complexity of the defect morphology, CBCT and IOS were taken, and a virtual hybrid model was prepared to aid the treatment planning process.

4.2.2 Data acquisition

CBCT scans were taken before and 9 months after surgical treatment with a Planmeca Viso G7® (Planmeca, Helsinki, Finland) machine (*Figure 43.*).



Figure 43.: Baseline CBCT scan

A: Axial view; **B** Sagittal view; **C:** Coronal view of tooth 23; **D:** Coronal view of tooth 24; **E:** Coronal view of tooth 25; **F-H:** Coronal view of tooth 26; **I:** Coronal view of tooth 27

Imaging parameters:

- voxel size: 150 μm
- anode voltage: 100 kV
- tube current: 12 mA
- FOV: 100 mm x 100 mm

Intraoral scans were taken using a Trios 3® (3Shape, Copenhagen, Denmark) intraoral optical scanner to capture a digital model of the clinical situation.

4.2.3 Digital data processing

After semi-automatic segmentation of CBCT images, STL files of the intraoral scan were imported to 3D Slicer. Spatial registration was performed according to the method described in section 3.1.2 using the “Fiducial registration wizard” module found in the “IGT” extension of 3D Slicer (145). Rigid Alignment was executed based on anatomical landmarks (33, 146). The model was further processed in Meshmixer®. Crowns of the segmented tooth models were substituted with the crowns from the IOS (158, 159) generating composite tooth models. Final model composition and coloring of the model were also carried out to make the appearance more realistic (Figure 44.).

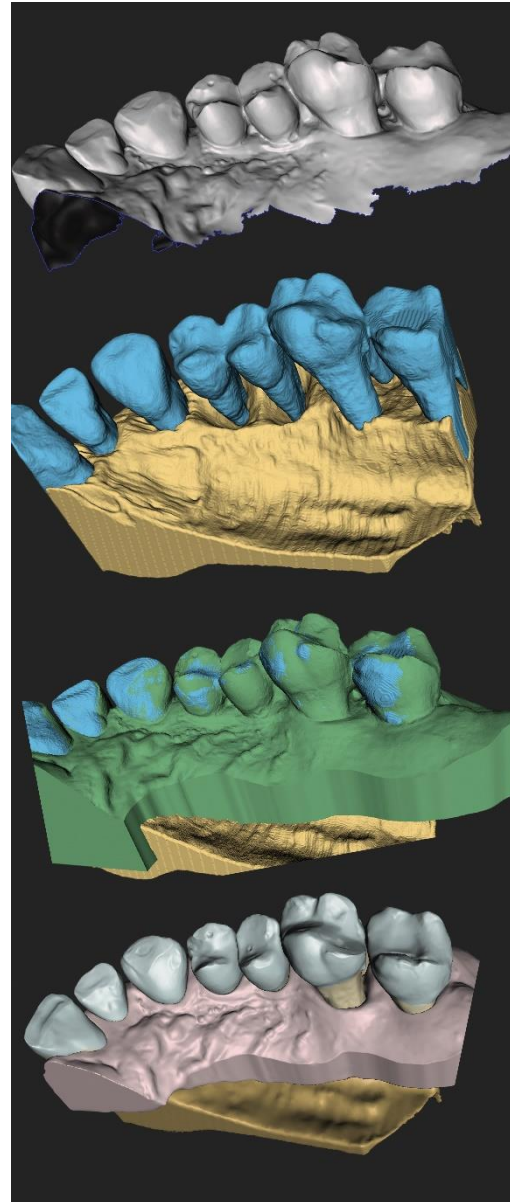


Figure 44.: Stages of model preparation

4.2.4 Virtual planning and surgical simulation

After model preparation, surgical planning and simulation were executed in Meshmixer® as well, utilizing CAD modeling tools in the software's inventory even though their original intended purpose is completely different. Stepwise surgical treatment of the complex defect was planned.

In the first step, extraction and simultaneous alveolar preservation was performed. One month after the first surgery regenerative treatment of the intrabony defects around teeth 24 and 25 was carried out.

4.2.4.1 Initial incision and flap elevation

Due to the unique model composition of the data processing method described in section 3.1.3, boundaries and dimensions of separate anatomical structures mimic the true clinical situation. Therefore, if the incision and the flap elevation are simulated on the soft tissues, underlying hard tissue defects will be visible and the most convenient access to a certain part of the defect can be determined. Even though the two surgical steps require a different flap design and regenerative materials, the basic principles for surgical planning are similar, therefore it will only be discussed here.

Utilizing “**Select**”, the area where the flap will be elevated was selected on the soft tissue model (selected triangles are highlighted in orange). And by applying transformation to only the selected portion of the model it was modified until the underlying bone defect became visible. If the flap design wasn't satisfactory, the selected area was modified and the process was repeated.

4.2.4.2 Regenerative material application

Both surgeries utilized membranes; a long-term resorbable membrane (Soft Cortical Lamina®, TecnoSS, Torino, Italy) was used for alveolar ridge preservation in the first

surgery, and a resorbable collagen membrane (Bio-Oss Collagen®, Geistlich AG, Wolhusen, Switzerland) was used for guided tissue regeneration (GTR) in the second surgery. The 3D model of periodontal and alveolar hard tissue defects allows for the customization of different types of barrier membrane. The area of the defect was outlined on the hard tissue model by selecting the surface, and by utilizing the “**Unwrap**” function in the “*Edit*” module of Meshmixer® a flattened representation of the selected area was generated. During surgery the membranes were shaped according to the flattened objects.

4.2.5 Additive manufacturing of hard tissue model

The main focus of this thesis is virtual planning and the application of digital models, thus additive manufacturing (3D printing) will not be discussed in detail, although it is a powerful tool to aid surgeons and educate patients (8-10, 166, 167). Digital models visible on a computer screen provide a realistic 3D representation, therefore 3D printed models are often not necessary for surgical planning.

Nevertheless, in the planning and treatment process of this case a 3D printed physical model was utilized during surgery. The model was manufactured with stereolithography (SLA) technology on a Form 3B® (Formlabs, Somerville, Massachusetts, USA) 3D printer from surgical grade resin (Formlabs Dental SG®) (168).

4.2.6 Surgical rehabilitation process

4.2.6.1 Step 1: Alveolar ridge preservation utilizing the extraction site development technique (XSD)

Extraction and simultaneous ridge preservation were carried out according to the XSD technique (115) described in section **1.4.2**. Atraumatic extraction of tooth 27 was performed by trisection and the application of small elevators. Following preparation of a double-layer tunnel flap from a single mesially-placed vertical incision, the pre-shaped long-term resorbable membrane (Soft Cortical Lamina®, TecnoSS, Torino, Italy) was

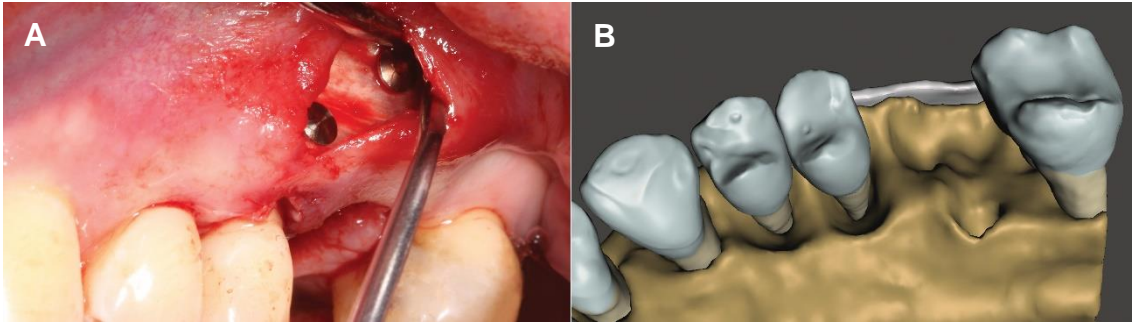


Figure 45.: Re-establishment of the buccal bone dehiscence with a long-term resorbable membrane

A: Intraoperative image; B: Preoperative plan

placed in the subperiosteal layer on the buccal bone surface (*Figure 45.*). The membrane was extended slightly mesially and distally to the extraction defect in an attempt to achieve approximal defect fill at the neighboring teeth. Approximal components of the periodontal defects developed at teeth 25 and 27 were debrided from the extraction socket.

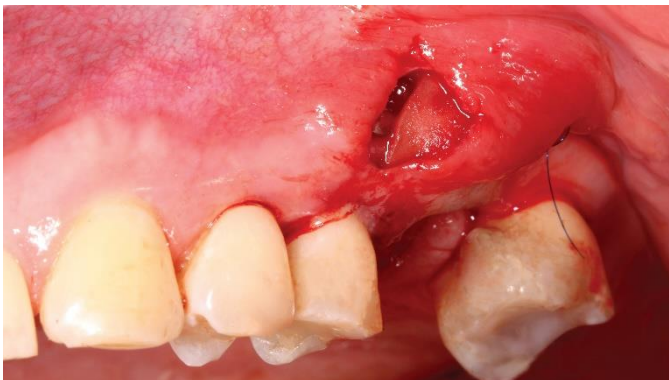


Figure 46.: Fixation of the xenogeneic collagen matrix

To maintain ideal soft tissue contour at the extraction site, a xenogeneic collagen matrix (mucoderm®, Botiss, Zossen, Germany) was pulled into the suprapariosteal tunnel and was fixed with horizontal mattress sutures (*Figure 46.*). Resorbable collagen fleece (Lyostypt®, B. Braun, Melsungen, Germany) was placed into the extraction socket to stabilize the blood clot. The extraction socket was sutured with an external crossed horizontal mattress suture utilizing 5-0 non-resorbable monofilament suturing material (*Figure 47.*). The patient was instructed to avoid brushing at

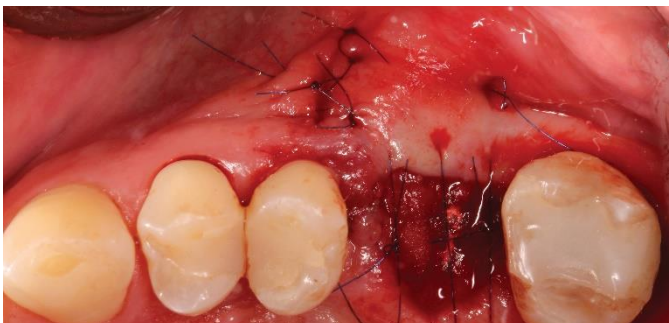


Figure 47.: Wound closure

the surgical area for the first two postoperative weeks. Sutures were removed after 14 days.

4.2.6.2 Step 2: Periodontal regenerative surgical treatment

One month following the first surgical intervention, regenerative surgical treatment of the circumferential horizonto-vertical periodontal defects around of teeth 24 and 25 was carried out. Combining different aspects of the NIPSA, SFA, and pinhole (169) surgical techniques, defects were treated with a minimally invasive approach.

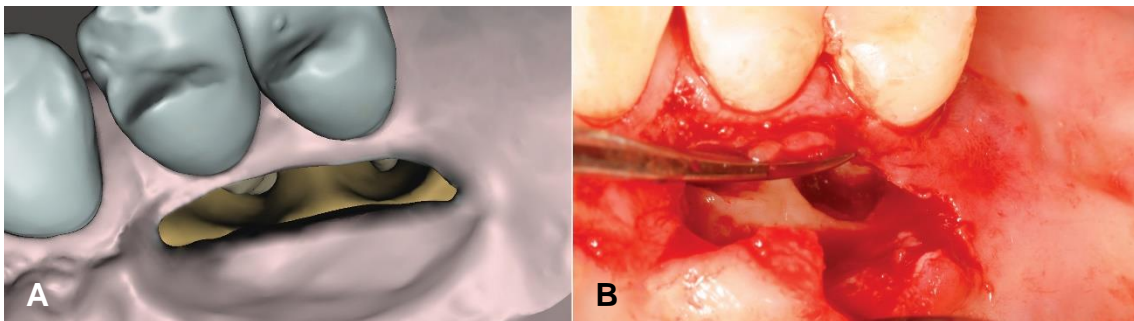


Figure 48.: Palatal remote paramarginal incision
A: Preoperative plan; **B:** Intraoperative image

The initial paramarginal incision was placed at the palatal aspect of teeth 24 and 25 4 mm away from the sulcus. The remote full thickness mucoperiosteal flap was elevated to access the palatal area of the circumferential defects (*Figure 48.*).

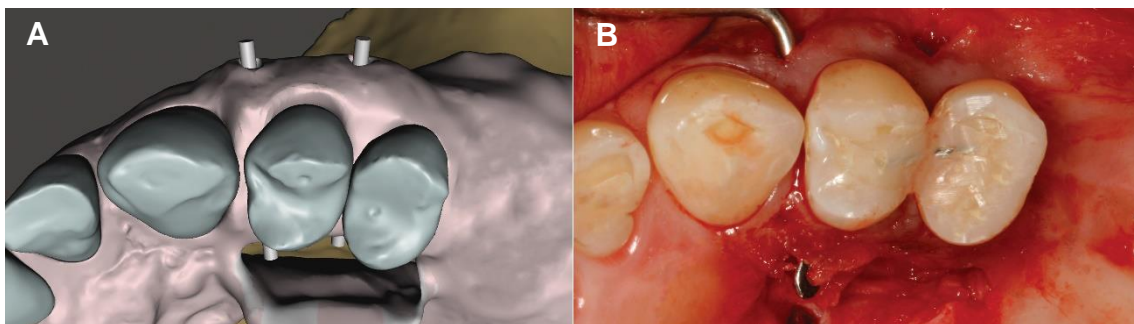


Figure 49.: Buccal pinhole incisions for enhanced surgical access and a "tunnelized" interdental papilla **A:** Preoperative plan; **B:** Intraoperative image

Two pinhole incisions were made at the buccal aspect 5 mm away from the marginal gingiva at the interdental spaces of teeth 23, 24, and 25 to allow access to the buccal area

of the defect. Intrasulcular incisions and incision of papillae were avoided to increase postoperative blood clot stability (113) (*Figure 49*).

Defect debridement was performed with hand and ultrasonic instruments. During debridement the 3D printed, sterilized model was utilized for intraoperative navigation to enhance visibility and haptic perception of the defect – similarly to how surgeons use anatomical 3D printed models in general medicine (170-172).

After defect debridement a combination of GTR (Bio-Guide®, Geistlich AG, Wolhusen, Switzerland) and bovine derived xenograft (BDX) was applied as the regenerative strategy. The defect was filled with Bio-Oss Collagen® that consists of 90% BDX and 10% porcine derived collagen (173). According to the digitally predetermined membrane forms, two separate membrane strips were shaped. The first strip was pulled between the two premolars the second semilunar shaped strip was placed on top to cover the palatal

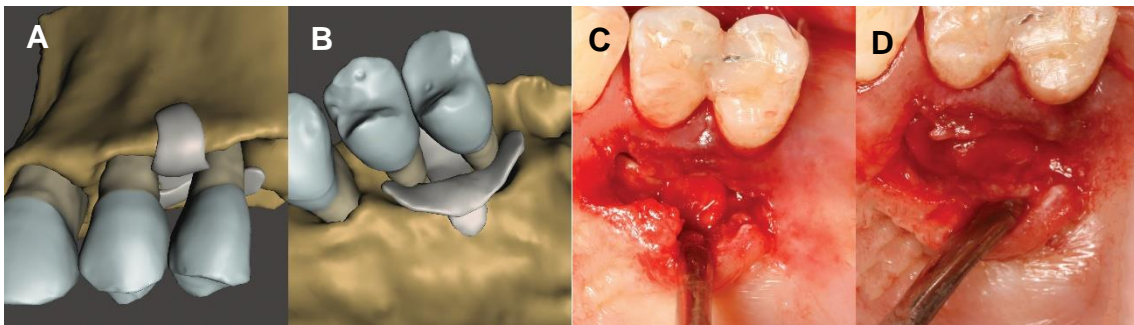


Figure 50.: Positioning of the resorbable collagen membrane strips
A: Preoperative plan, buccal aspect; **B:** Preoperative plan, palatal aspect; **C-D:** Intraoperative image palatal aspect

aspect of the defect (173) (*Figure 50*).

Pinhole incisions and the palatal paramarginal incision were sutured with horizontal mattress sutures utilizing a 6-0 monofilament suturing material. Sutures were removed after 14 days. The patient was instructed to avoid mechanical cleaning in the surgical area until suture removal.

4.2.7 Follow-up and evaluation of surgical outcomes – Outcome measures

After the second surgical intervention the patient was recalled at 1, 3, 6, and 9 months for follow-up appointments. After the 9-month healing period a second follow-up CBCT scan and an IOS were acquired to validate surgical outcomes. After the segmentation of the 9-

month follow-up CBCT, spatial alignment of CBCT and IOS data was carried out, subsequently pre- and postoperative statuses could be compared (*Figure 51*).

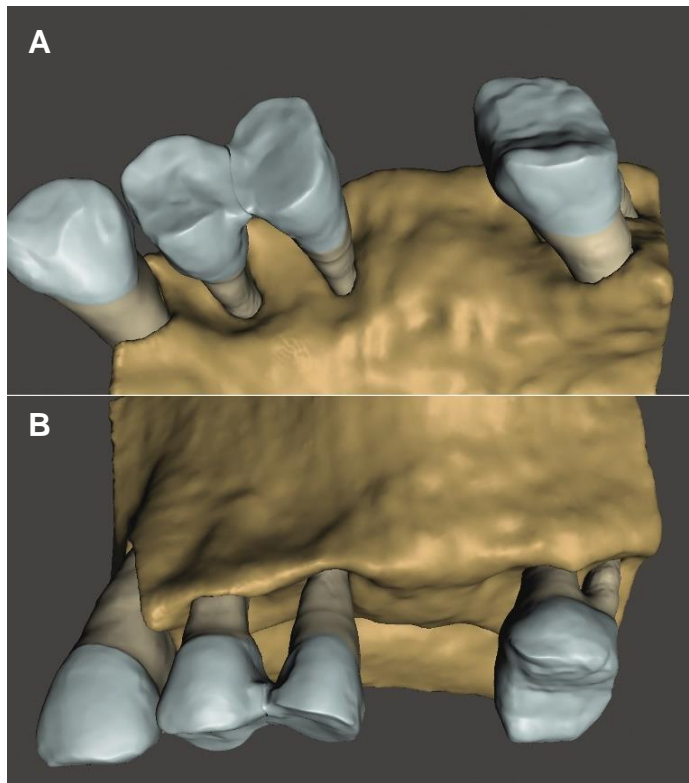


Figure 51.: *Segmented 3D model of 9-month follow-up CBCT*

A: *Palatal aspect, showing partial fill of the intrabony defect components as well as a slight marginal bone resorption;*

B: *Marginal bone resorption is visible at the buccal aspects of both premolar teeth resulting in the postoperative recession of the marginal gingiva*

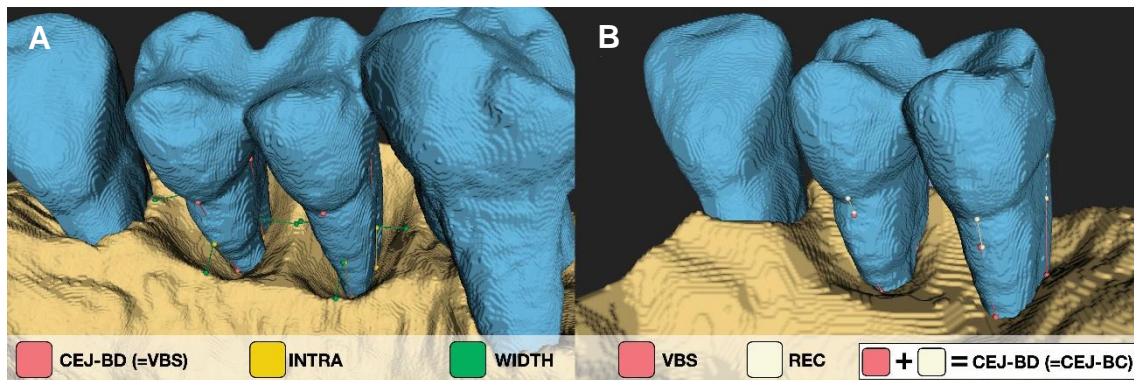
4.2.7.1 Primary outcome measure – Volumetric and morphological changes

Three-dimensional subtraction analysis of the pre- and postoperative 3D model was performed to assess volumetric and 3D morphological changes of hard tissues following surgery. The methodology will be described in detail in section 4.3.4.2.

4.2.7.2 Secondary outcome measure – Linear evaluation, radiographic defect fill

Digital linear measurements were taken utilizing the “**Line markup**” tool in 3D Slicer at the mesial (mes), distal (dist), buccal (bucc), and palatal (palat) aspects of teeth 24 and 25 to determine tissue alterations at each tooth surface (*Figure 52*). The following parameters were measured on the baseline and follow up hybrid models were constructed from the CBCT scan and IOS:

- **CEJ-BD**: vertical distance between the cemento-enamel junction (CEJ) and the bottom of the defect (BD)
- **CEJ-BC**: vertical distance between the CEJ and the bone crest (BC)
- **INTRA**: vertical distance between the bone crest and the bottom of the defect
- **WIDTH**: Horizontal distance between the tooth surface and marginal bone crest
- **VREC** (virtual gingival recession): vertical distance between the CEJ and the marginal gingiva measured on the virtual models
- **VBS** (virtual bone sounding): vertical distance between the marginal gingiva and the bottom of the defect



*Figure 52.: Digital linear measurements on pre- and postoperative 3D models
A: Preoperative defect characteristics; B: Postoperative periodontal bony topography*

Besides digital measurements, the following clinical parameters were assessed: (i) probing pocket depth (PPD), (ii) gingival recession (REC), (iii) clinical attachment level (CAL), (iv) full mouth plaque score (FMPS), and (v) full mouth bleeding score (FMPS).

By comparing pre- and postoperative CEJ-BD values, intrabony hard tissue gain can be determined for each specific tooth surface, while by comparing pre- and postoperative CEJ-BC values the crestal bone resorption can be evaluated at each tooth surface. The percentage of intrabony defect fill could be determined by the ratio of the intrabony hard tissue gain and the depth of the intrabony component (INTRA) at baseline.

4.3 CBCT Subtraction Analysis of 3D Changes Following Alveolar Ridge Preservation: a case series of 10 patients with a 6-month follow-up

In the previous sections virtual models were utilized mostly for surgical planning and simulation. However, virtual models can be used for the volumetric evaluation of surgical outcomes.

In section *1.5.2* articles describing different methods for the evaluation of several ARP procedures were summarized including the XSD technique (115, 133, 135). In their article *Windisch et al.* utilized linear and planimetric measurement with the help of a 1 mm² grid to validate the outcomes, however 3D measurements were not taken.

A retrospective case series published by our group evaluated volumetric and 3D morphological surgical outcomes of 10 cases treated with the XSD technique. Additionally, to present the results of the surgical outcomes, the article with the same title described a novel 3D subtraction method (174).

4.3.1 Patient selection

Ten surgical sites of ten systemically healthy, partially edentulous patients were selected for ARP and radiographical analysis. EDS type 3 and type 4 defects (95) around single rooted teeth with a hopeless prognosis were treated.

Exclusion criteria were:

- previous irradiation therapy in the surgical area
- uncontrolled diabetes
- systemic steroid treatment
- systemic bisphosphonate treatment
- smoking
- bad oral hygiene
- pregnancy

4.3.2 Surgical procedure

Defects were treated with the aforementioned XSD technique (*Figure 53.*) (sections 1.4.2.1 and 3.3.6.1), therefore the surgical procedure will not be described here.

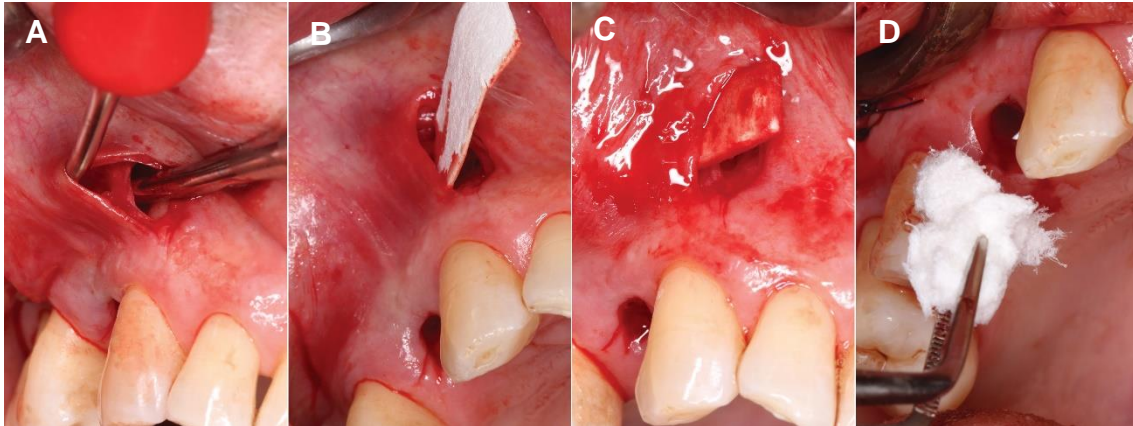


Figure 53.: Extraction site development (XSD) technique for the preservation of an EDS type 4 extraction defect at the area of tooth 14

A: Bilaminar tunnel preparation; B: Positioning of a long-term resorbable membrane subperiosteally; C: Suprapariosteal placement of a xenogeneic collagen matrix; D: Collagen fleece placed into the extraction socket

4.3.3 Image acquisition

CBCT scans were taken prior to and 6 months after tooth extraction to evaluate the results of the surgery. Due to the retrospective nature of the evaluation, the CBCT scanning protocol was not standardized, therefore exposure parameters (FOV, voxel size, anode voltage, and tube current) varied between CBCT datasets. Out of the 10 pre- and 10 postoperative CBCT scans, 16 scans were taken with I-CAT FLX® (KaVo Dental GmbH, Biberach an der Riß, Germany), 2 scans were taken with Planmeca Viso® (Planmeca, Helsinki, Finland), 1 scan was taken with Carestream CS 8100® (Onex Corporation, Toronto, Canada), and 1 scan was taken with PaX-Reve 3D® (Vatech, Gyeonggi-do, South Korea). Metal artifact reduction was applied if the patients had permanent restorations or implants.

- Imaging parameters (I-CAT FLX®):
 - voxel size: 300 μm
 - anode voltage: 120 kV
 - x-ray tube current: 36 mA
- Imaging parameters (Planmeca Viso®)
 - voxel size: 150 μm
 - anode voltage: 100 kV
 - x-ray tube current: 12 mA
- Imaging parameters (Carestream CS 8100®)
 - voxel size: 75 μm
 - anode voltage: 84 kV
 - x-ray tube current: 6 mA
- Imaging parameters (PaX-Reve 3D®)
 - voxel size: 120 μm
 - anode voltage: 89 kV
 - x-ray tube current: 5 mA

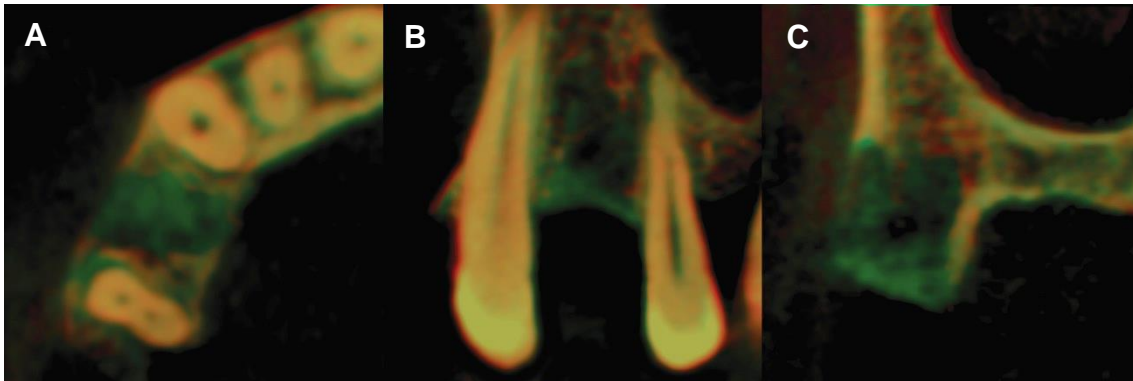
4.3.4 Radiographic image processing

4.3.4.1 Spatial registration of pre- and postoperative CBCT scans

Spatial registration in medical image processing is utilized to find the spatial relationship between two or more images. Spatial registration has already been mentioned in section **3.1.2** for the alignment of CBCT scans and IOS data. In that instance anatomical landmark-based transformation was executed (146, 149). However, registration of two CBCT datasets can be done automatically with the application of an intensity-based registration algorithm (175).

3D Slicer extension “**elastix**”, developed by PerkLab (Queens University, Kingston, Canada) for the Insight Toolkit (ITK) (176) was utilized for spatial registration. Utilizing this algorithm, baseline and follow-up CBCT images were aligned based on similarities in voxel intensity values. To ensure an accurate alignment both images were cropped to the same general area (i.e. upper or lower jaw), however over-cropping should be avoided. During registration one dataset, the moving volume (follow-up) was transformed to fit the other dataset (baseline), the fixed volume. To validate the accuracy of the transformation the color palette of CBCT datasets was changed from gray to red (baseline) and green (follow-up) and the opacity of the follow-up dataset was reduced.

Two alternate color palettes allowed differences between the two datasets to be examined (e.g., extracted teeth visible in red, hard tissue gain visible in green) (*Figure 54.*) (174).



*Figure 54.: Superimposition of pre- and postoperative CBCT scans with Slicer elastix
A: Axial view; B: Sagittal view; C: Coronal view*

4.3.4.2 CBCT Segmentation and 3D subtraction

Three-dimensional hard tissue models of pre- and postoperative CBCT datasets were acquired with the semi-automatic segmentation protocol described in section 3.1.1.

After spatial registration and image segmentation, preoperative alveolar bone models were subtracted from postoperative alveolar bone models in order to visualize volumetric

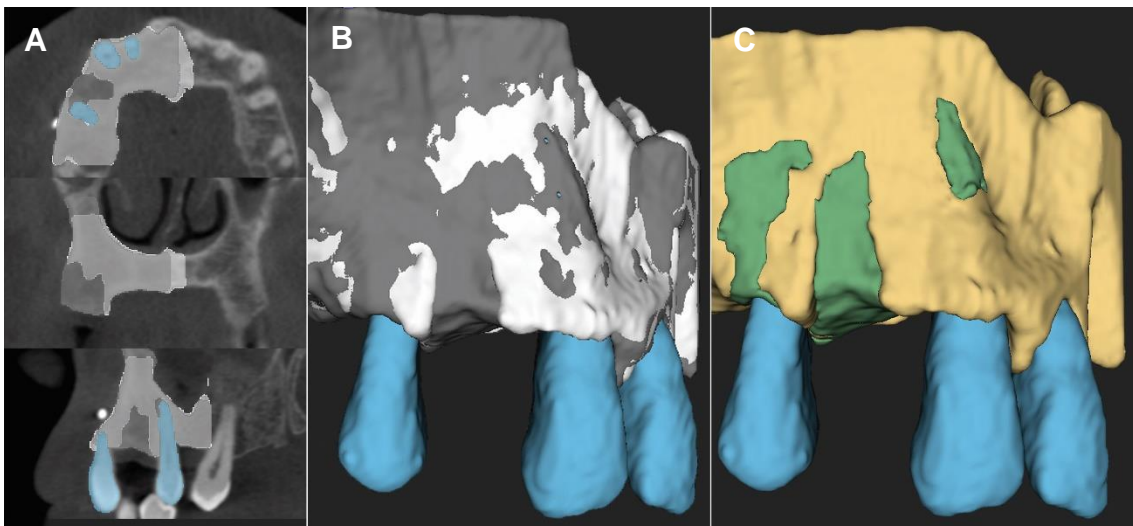


Figure 55: Spatial registration and subsequent 3D subtraction of pre- and postoperative models

A: 2D views of superimposed, segmented pre- and postoperative CBCT scans; B: Superimposed 3D models; C: Hard tissue gain visualized after 3D subtraction

hard tissue gain and 3D hard tissue alterations. Utilizing the “*Subtract*” function in the “*Logical Operators*” tool **Boolean subtraction** was applied to the two alveolar bone models. After subtraction a new 3D model representing hard tissue gain was acquired (*Figure 55.*).

4.3.5 Outcome variables

4.3.5.1 Primary outcome variable – Volumetric and 3D morphological hard tissue alterations

The primary outcome variable of the study was the volumetric difference between pre- and postoperative CBCT scans. The volume of the newly formed hard tissues was

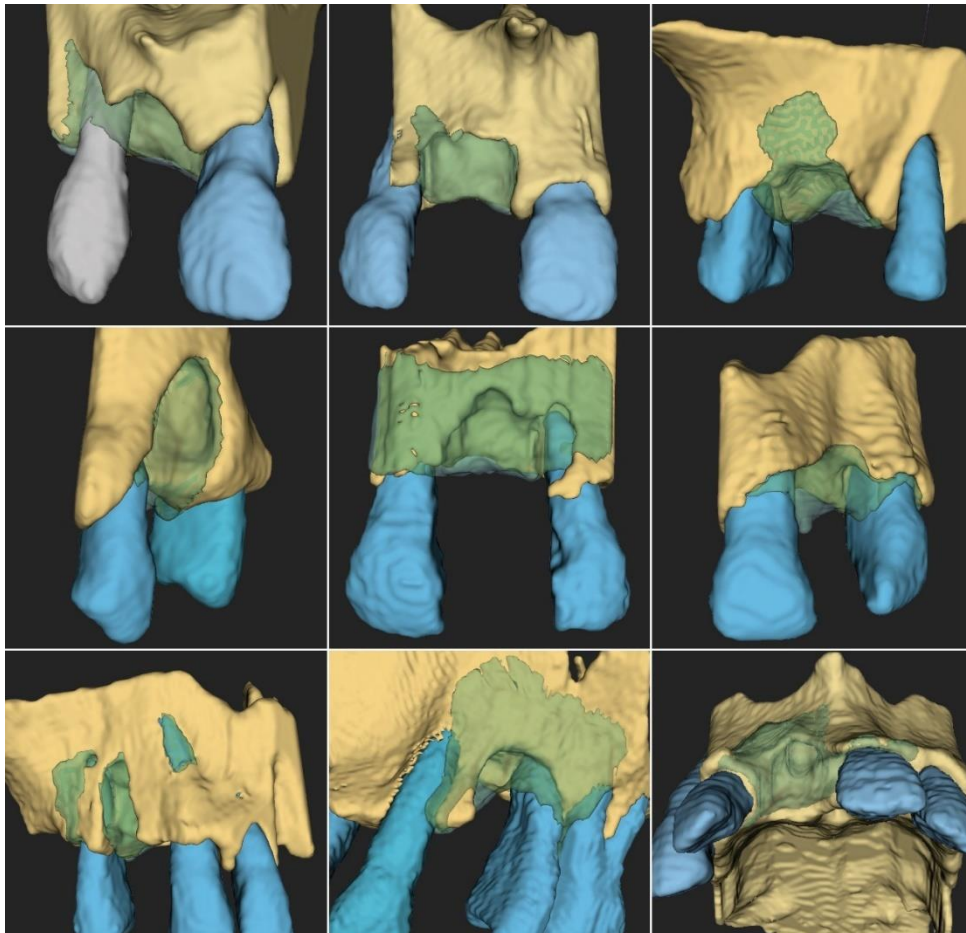


Figure 56.: 3D morphological hard tissue alterations at extraction sites (174)

calculated with the application of the “*Segment statistics*” module. Also, 3D morphological alterations were observed (*Figure 56.*).

4.3.5.2 Secondary outcome measure – Linear measurements of horizontal and vertical dimensions at the surgical area

Secondary outcomes of the study were the horizontal and vertical linear measurements taken midcrestally at the midline, distal, and mesial aspects of the extraction site utilizing the “**Line markup**” tool in 3D Slicer. Vertical changes were measured from the base of the defect (preoperative) to the most coronal portion of the edentulous ridge

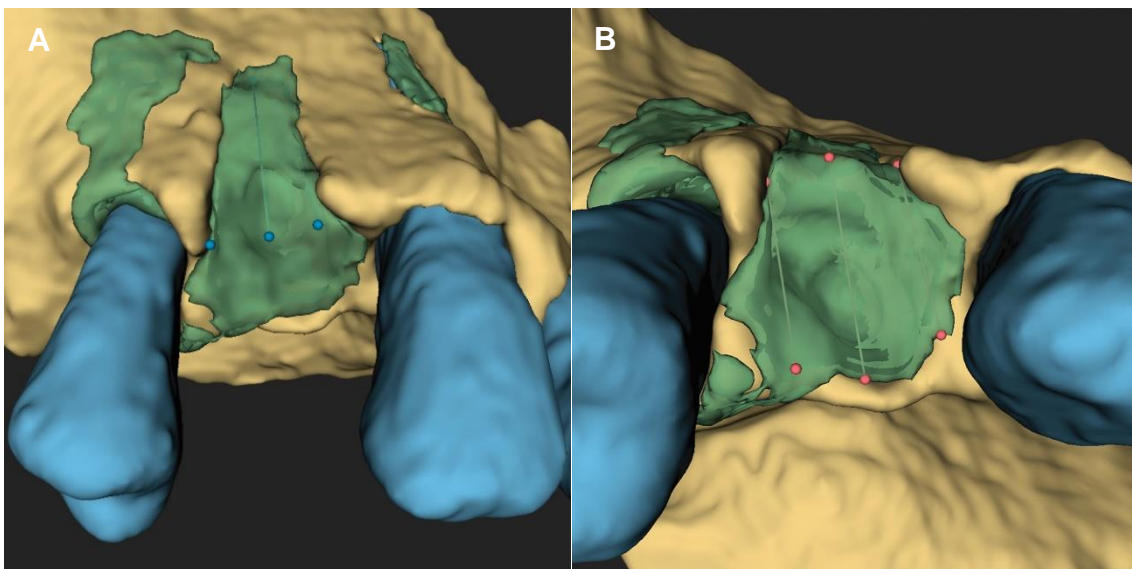


Figure 57.: Linear measurements

A: Midcrestal vertical measurements at the extraction site; **B:** Horizontal measurements at the top of the alveolar crest at the extraction site

(postoperative) at all three aspects (*Figure 57.*). Horizontal changes were measured between the palatal marginal bone crest (preoperative) and the newly formed buccal bone crest (postoperative) at all three aspects.

4.3.6 Statistical analysis

In the present study the amount of new hard tissue gain was expressed with volumetric, horizontal, and vertical dimension changes. Therefore, only descriptive statistics were executed, and mean values and standard deviations (SDs) were calculated.

4.4 Summary

In the second part of the “Methods” chapter, applications of the virtual hybrid models in the regenerative-reconstructive surgical treatment of periodontal and alveolar ridge defects were presented. Virtual models were utilized prior to surgery for diagnostic purposes to visualize periodontal and extraction defects in 3D for a more accurate surgical planning and simulation of different regenerative approaches. Virtual and 3D printed models were utilized intraoperatively to enhance “visibility” during minimally invasive surgical approaches, while pre- and postoperative 3D models were utilized to assess volumetric and 3D morphological alterations after regenerative-reconstructive surgical approaches. However, beyond their application in periodontology and implant dentistry, models can be utilized in other fields of dentistry, such as endodontic surgery, orthodontic treatment, orthognathic surgery, and other areas of maxillofacial surgery.

5 RESULTS

5.1 Digital Hybrid Model Preparation for Virtual Planning of Reconstructive Dentoalveolar Surgical Procedures – Descriptive results

The paper that describes the detailed protocol for model acquisition was a methodology article with its main focus being to present the model acquisition method step-by-step. Therefore, only short descriptive results were included in the original article (137).

Various semi-automatic segmentation tools, such as delineation tools (“**Level tracing**”), morphological contour interpolation algorithms (“**Fill between slices**”), and model smoothing (“**Smoothing**”) found in the inventory of 3D Slicer significantly reduce the duration of image processing compared to manual segmentation. However, due to the similarity of voxel intensity values of teeth and alveolar bone, separation of these two anatomical structures must be done by hand, which can be time-consuming. Artifacts present on CBCT scans also hinder the segmentation process.

Through superimposition of IOS data and subsequent CAD modeling, a highly detailed virtual patient setup was constructed. The coronal portions of the segmented tooth models were compromised by artifacts produced by dental restorations. Replacement of segmented tooth crowns with the crowns on the IOS resulted in improved composite tooth models that represent the clinical situation more realistically. However, occasional alignment errors compromise the accuracy of the models. By separating dental structures from the rest of the IOS, a static 3D model of soft tissues (gingiva, keratinized mucosa, mobile oral mucosa) was incorporated.

A series of Boolean subtractions between each element of the hybrid model and coloring of the model finalized the virtual patient setup, thus models became a digital representation of the clinical situation.

5.2 Three-dimensional visualization of intrabony periodontal defects for regenerative surgical treatment planning

5.2.1 *Baseline patient and defect characteristics*

The mean age was 48.75 ± 14.82 years; 2 patients were male, and 2 patients were female. From the treated teeth three were single rooted (upper central incisor, lower second incisor, lower first premolar) and three were multi rooted (lower first molar, upper first molar, upper second molar). Baseline PPD, REC, and CAL values averaged 8.00 ± 1.26 mm, 1.67 ± 1.03 mm, and 9.67 ± 1.21 mm, respectively. FMPS value averaged 12.85 %, and FMBS was found to be 9.73 %.

5.2.2 *Comparison of intrasurgical- and digital measurements – validation of virtual models*

Following flap elevation and surgical defect debridement, the depth and width (INTRA, WIDTH) of the intrabony components were assessed directly at multiple aspects. During surgery a 4.22 ± 1.67 mm average vertical distance between the marginal bone crest to the bottom of the defect was measured, while the vertical distance on digital models averaged at 4.05 ± 1.51 mm. Horizontal distances between the marginal bone crest and the tooth surface were found to be 3.17 ± 0.98 mm intrasurgically and 3.50 ± 1.02 mm on digital models.

Differences of INTRA and WIDTH values of intrabony components between the two measurements were 0.31 ± 0.21 mm and 0.41 ± 0.44 mm respectively. Following statistical analysis, no significant differences were found between INTRA and WIDTH values. The difference between clinical- and digital measurements regarding components of periodontal defects was statistically not significant ($P < 0,001$). Values and differences in intrasurgical and digital measurements are shown in *Table 1* (161). With a Bland Altman analysis the mean value of difference (bias) was 0,163 mm and -0.136 in terms of the vertical- and horizontal dimensions of the intrabony component respectively.

| Defect | INTRA* (mm) | | WIDTH** (mm) | |
|--------|--------------------|--------------------|--------------------|--------------------|
| | Intrasurgical | Digital | Intrasurgical | Digital |
| 1 | 3 | 2.28 | 2 | 2.17 |
| | 3 | 3.27 | | |
| | 4 | 3.86 | | |
| 2 | 8 | 7.41 | 4 | 4.36 |
| 3 | 3 | 3.23 | 2 | 2.25 |
| | 4 | 4.13 | | |
| 4 | 5 | 4.72 | 4 | 3.75 |
| 5 | 3 | 2.80 | 4 | 4.15 |
| 6 | 5 | 4.79 | 3 | 4.30 |
| | 4.22 ± 1.64 | 4.05 ± 1.51 | 3.17 ± 0.98 | 3.50 ± 1.02 |

* Vertical distance from marginal bone crest to the base of the defect
** Horizontal distance from the root surface to the most coronal point of the bone crest

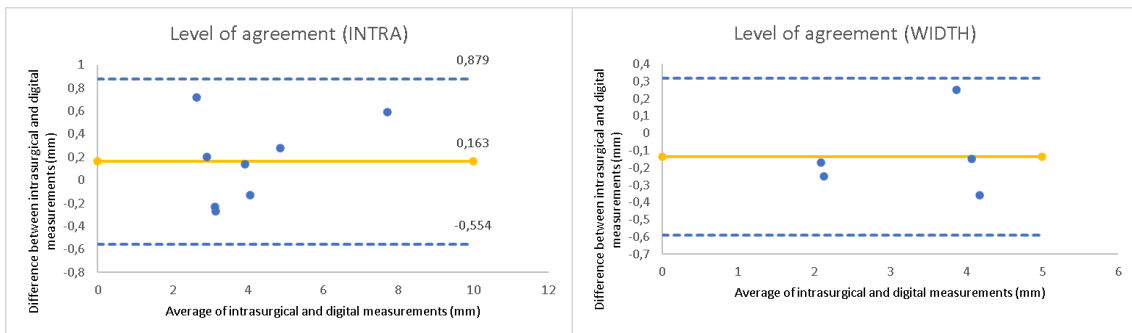


Figure 58: Bland Altman plot. Level of agreement between two measurement modalities

5.2.3 Preoperative defect morphology assessment

A secondary outcome measure of the study was to investigate whether the defect morphology and subsequent surgical modality could be predetermined precisely with conventional diagnostic methods versus the 3D virtual models.

Out of six cases (i) general defect morphology was assessed correctly in four, (ii) the number of affected tooth surfaces was determined correctly in three, and (iii) the number of bony walls was determined correctly in only one case using conventional diagnostic methods. In cases of multirouted teeth, (iv) grade of furcation involvement could not be

determined correctly with conventional diagnostic methods. With conventional diagnostic methods, one- and two-walled approximal intrabony defects could be diagnosed successfully.

In summary, all four defect characteristics were assessed accurately in only one case with IRs and direct clinical measurements. Conversely, with the application of the 3D models generated with the presented semi-automatic segmentation method all four defect characteristics could be determined in all cases. Data are shown in **Table 2** (161).

| Defect Characteristics | | Patient 1 | Patient 2 | | Patient 3 | | Patient 4 |
|---|----------------|---------------------|------------|------------|---------------------------|-----------------|-----------------|
| | | Tooth 11 | Tooth 44 | Tooth 42 | Tooth 36 | Tooth 16 | Tooth 27 |
| Morphology | Conventional* | Horizontal | Vertical | Vertical | Vertical | Vertical | Horizontal |
| | 3D** | Horizontal-Vertical | Vertical | Vertical | Vertical | Vertical | Vertical |
| | Intraoperative | Horizontal-Vertical | Vertical | Vertical | Vertical | Vertical | Vertical |
| No. of affected tooth surfaces | Conventional | 3 | 1 | 1 | 2 | 1 | 1 |
| | 3D | 3 | 1 | 2 | 3 | 2 | 3 |
| | Intraoperative | 3 | 1 | 2 | 3 | 2 | 3 |
| No. of bony walls | Conventional | 0 | 1 | 2 | Mes***: 2; Dist****: 1 | 2 | 0 |
| | 3D | 3 | 1 | 1 | Mes: 1; Dist: 1 | 1 | 2 |
| | Intraoperative | 3 | 1 | 1 | Mes: 1; Dist: 1 | 1 | 2 |
| Furcation involvement | Conventional | - | - | - | Grade 0 | Mesial grade I | Grade 0 |
| | 3D | - | - | - | Lingual grade II | Mesial grade II | Mesial grade II |
| | Intraoperative | - | - | - | Lingual grade II | Mesial grade II | Mesial grade II |
| Was it possible to determine defect characteristics with conventional methods? | | NO | YES | NO | NO | NO | NO |
| Was it possible to determine defect characteristics with the aid of 3D virtual models? | | YES | YES | YES | YES | YES | YES |
| * Direct clinical measurements + intraoral radiographs ** 3D virtual models *** Mesial tooth surface **** Distal tooth surface | | | | | | | |

Virtual planning and volumetric evaluation in the regenerative-reconstructive surgical treatment of a complex periodontal defect

5.2.4 Volumetric and 3D morphological alterations after stepwise surgical treatment

After semi-automatic segmentation, spatial registration, and model subtraction, volumetric and 3D morphological changes were assessed. As a result of the stepwise surgical treatment a cumulative hard tissue gain of 0.44 cm³ occurred at the surgical area. Hard tissue gain was observed within the extraction socket of tooth 26 and in the intrabony component of circumferential defects around tooth 24 and tooth 25. Slight buccal hard tissue gain outside of the bony envelope at the extraction and alveolar ridge preservation site could be observed. Simultaneously, marginal hard tissue resorption of 0.11 cm³ was observed. Hard tissue resorption however did not affect periodontal attachment on the two premolar teeth (165).

5.2.5 Linear evaluation, radiographic defect fill after reconstructive periodontal treatment

Measurements were taken at four surfaces (mesial, palatal, distal, buccal) of tooth 24 and tooth 25 on both the pre- and postoperative 3D models to determine linear periodontal hard tissue gain and marginal periodontal bone resorption.

5.2.5.1 Baseline defect parameters

5.2.5.1.1 Baseline parameters around tooth 24

Digitally CEJ-BD (vertical distance between the CEJ and the bottom of the defect) values were measured to be 5.36 mm at the mesial aspect; 7.12 mm at the palatal aspect; 6.97 mm at the distal aspect, and 2.97 mm at the buccal aspect. CEJ-BC (vertical distance between the CEJ and the marginal bone crest) values were measured to be 2.89 mm at the mesial aspect, 2.89 mm at the palatal aspect, 5.05 mm at the distal aspect, and 2.10 mm

at the buccal aspect. INTRA (vertical distance between the marginal bone crest and the bottom of the defect) was measured digitally to be 2.47 mm at the mesial aspect, 4.23 mm at the palatal aspect, 1.92 mm at the distal aspect, and 0.87 mm at the buccal aspect. WIDTH (horizontal distance between the tooth surface and the marginal bone crest) was measured at 2.64mm, 1.79 mm, 2.19 mm, and 0.74 mm at the mesial, palatal, distal, and buccal aspects of the tooth. On the 3D virtual models no recession of the marginal gingiva (VREC) was recorded at baseline. VBS (virtual bone sounding) values were calculated by the summation of VREC and CEJ-BD values, however since VREC could not be detected, baseline CEJ-BD and VBS values were the same. Digital measurements are summarized in **Table 3**.

| <i>Table 3: Digitally measured baseline parameters around tooth 24 (mm)</i> | | | | |
|---|---------------|----------------|---------------|---------------|
| | Mesial aspect | Palatal aspect | Distal aspect | Buccal aspect |
| VBS | 5.36 | 7.12 | 6.97 | 2.97 |
| CEJ-BD | 5.36 | 7.12 | 6.97 | 2.97 |
| CEJ-BC | 2.89 | 2.89 | 5.05 | 2.10 |
| INTRA | 2.47 | 4.23 | 1.92 | 0.87 |
| WIDTH | 2.64 | 1.79 | 2.19 | 0.74 |
| VREC | 0.00 | 0.00 | 0.00 | 0.00 |

Clinically PPD, REC, CAL values were measured at the same aspects as on the digital models. Clinical parameters are shown in **Table 4**.

| <i>Table 4: Baseline clinical parameters around tooth 24 (mm)</i> | | | | |
|---|---------------|----------------|---------------|---------------|
| | Mesial aspect | Palatal aspect | Distal aspect | Buccal aspect |
| PPD | 10 | 8 | 7 | 2 |
| REC | 0 | 0 | 0 | 0 |
| CAL | 10 | 8 | 7 | 2 |

5.2.5.1.2 Baseline parameters around tooth 25

CEJ-BD values were measured to be 8.69 mm at the mesial, 8.04 mm at the palatal, 9.19 mm at the distal, and 5.75 mm at the buccal aspect of tooth 25. CEJ-BC was measured 4.91 mm at the mesial, 4.11 mm at the palatal, 6.02 mm at the distal, and 2.85 mm at the

buccal aspects. INTRA was measured digitally to be 3.78 mm at the mesial aspect, 3.93 mm at the palatal aspect, 3.17 mm at the distal aspect, and 2.9 mm at the buccal aspect. WIDTH values were measured on the 3D models to be 1.70 mm, 2.24 mm, 1.63 mm and 1.28 mm, at the mesial, palatal, distal, and buccal aspects of tooth 25, respectively. On the 3D virtual models VREC could not be recorded at baseline. Digital measurements are summarized in *Table 5*.

| | Mesial aspect | Palatal aspect | Distal aspect | Buccal aspect |
|---------------|---------------|----------------|---------------|---------------|
| VBS | 8.69 | 8.04 | 9.19 | 5.75 |
| CEJ-BD | 8.69 | 8.04 | 9.19 | 5.75 |
| CEJ-BC | 4.91 | 4.11 | 6.02 | 2.85 |
| INTRA | 3.78 | 3.93 | 3.17 | 2.90 |
| WIDTH | 1.70 | 2.24 | 1.63 | 1.28 |
| VREC | 0.00 | 0.00 | 0.00 | 0.00 |

Clinically PPD, REC, CAL values were measured at the same aspects as on the digital models. Clinical parameters are shown in *Table 6*.

| | Mesial aspect | Palatal aspect | Distal aspect | Buccal aspect |
|------------|---------------|----------------|---------------|---------------|
| PPD | 8 | 6 | 9 | 6 |
| REC | 0 | 0 | 0 | 0 |
| CAL | 8 | 6 | 9 | 6 |

5.2.5.2 Outcomes at 9-month follow-up

5.2.5.2.1 Follow-up parameters at tooth 24

After complete or partial resolution of the intrabony component (and/or marginal bone resorption) follow-up CEJ-BD values equal CEJ-BC values. At 9 months CEJ-BD (=CEJ-BC) was measured digitally to be 3.28 mm at the mesial, 5.95 mm at the palatal, 5.62 mm at the distal, and 3.28 mm at the buccal aspect of tooth 24, whereas 1 mm and 2.11 mm VREC could be detected at the palatal and distal aspects, respectively. VBS values were measured to be 3.28 mm (mesial aspect), 4.95 mm (palatal aspect), 3.51 mm (distal aspect), and 3.28 mm (buccal aspect). Follow-up digital measurements are summarized in **Table 7**. Follow-up clinical parameters are shown in **Table 8**.

Table 7: Digitally measured follow-up parameters around tooth 24 (mm)

| | Mesial aspect | Palatal aspect | Distal aspect | Buccal aspect |
|---------------|---------------|----------------|---------------|---------------|
| VBS | 3.28 | 4.95 | 3.51 | 3.28 |
| CEJ-BD | 3.28 | 5.95 | 5.62 | 3.28 |
| CEJ-BC | 3.28 | 5.95 | 5.62 | 3.28 |
| VREC | 0.00 | 1.00 | 2.11 | 0.00 |

Table 8: Follow-up clinical parameters around tooth 24 (mm)

| | Mesial aspect | Palatal aspect | Distal aspect | Buccal aspect |
|------------|---------------|----------------|---------------|---------------|
| PPD | 4 | 3 | 4 | 2 |
| REC | 1 | 2 | 2 | 2 |
| CAL | 5 | 5 | 6 | 4 |

Around tooth 24 mesial, palatal, distal, and buccal CEJ-BD values showed reductions of 2.08 mm, 1.17 mm, 1.35 mm, and 0.31 mm respectively; these values represent linear intraosseus periodontal hard tissue gain. CEJ-BC values increased by 0.39 mm at the mesial, 3.06 mm at the palatal, 0.57 mm at the distal, and 1.18 mm at the buccal aspect of tooth 24, representing the crestal bone resorption at each tooth surface. The ratio of

intrabony hard tissue fill around tooth 24 was found to be 45.5 % (CEJ-BD change/baseline INTRA) (*Figure 58.*)

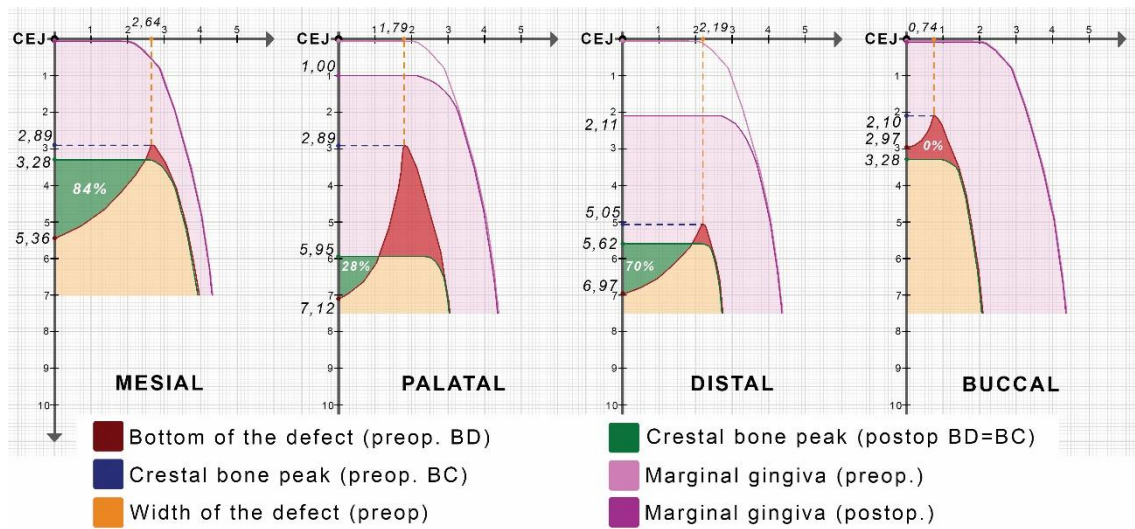


Figure 59.: Schematic visualization of crestal bone level changes (165)

5.2.5.2.2 Follow-up parameters at tooth 25

At 9 months CEJ-BD (=CEJ-BC) was measured digitally to be 5.61 mm at the mesial, 5.68 mm at the palatal, 6.01 mm at the distal, and 5.44 at the buccal aspect of tooth 25, whereas 1.09 mm, 1.46 mm, 2.11 mm, and 2 mm VREC could be detected at the mesial, palatal, distal, and buccal aspects of tooth 25, respectively. VBS values were measured to be 4.52 mm (mesial aspect), 4.22 mm (palatal aspect), 3.90 mm (distal aspect), and 3.39 mm (buccal aspect). Results are shown in *Table 9*. Follow-up clinical parameters are shown in *Table 10*.

| <i>Table 9: Digitally measured follow-up parameters around tooth 25 (mm)</i> | | | | |
|--|---------------|----------------|---------------|---------------|
| | Mesial aspect | Palatal aspect | Distal aspect | Buccal aspect |
| VBS | 4.52 | 4.22 | 3.90 | 3.39 |
| CEJ-BD | 5.61 | 5.68 | 6.01 | 5.44 |
| CEJ-BC | 5.61 | 5.68 | 6.01 | 5.44 |
| VREC | 1.09 | 1.46 | 2.11 | 2.05 |

| | Mesial aspect | Palatal aspect | Distal aspect | Buccal aspect |
|------------|---------------|----------------|---------------|---------------|
| PPD | 4 | 3 | 4 | 3 |
| REC | 1 | 2 | 2 | 2 |
| CAL | 5 | 5 | 6 | 5 |

Around tooth 25, CEJ-BD values showed a reduction of 3.08 mm at the mesial, 2.18 mm at the palatal, 3.18 mm at the distal, and 0.31 mm at the buccal aspects, while CEJ-BC values increased by 0.70 mm at the mesial, 1.57 mm at the palatal, 0.00 mm at the distal, and 2.59 mm at the buccal aspects of tooth 25. The ratio of intrabony hard tissue fill around tooth 25 was found to be 62.25 % (CEJ-BD change/ baseline INTRA). At the distal aspect a 100% intrabony defect fill was observed, resulting in complete resolution of the intrabony component of the defect (*Figure 59*).

VREC values were increased on average by 1.22 ± 0.87 mm resulting in the resolution of the supraosseous component of the defect.

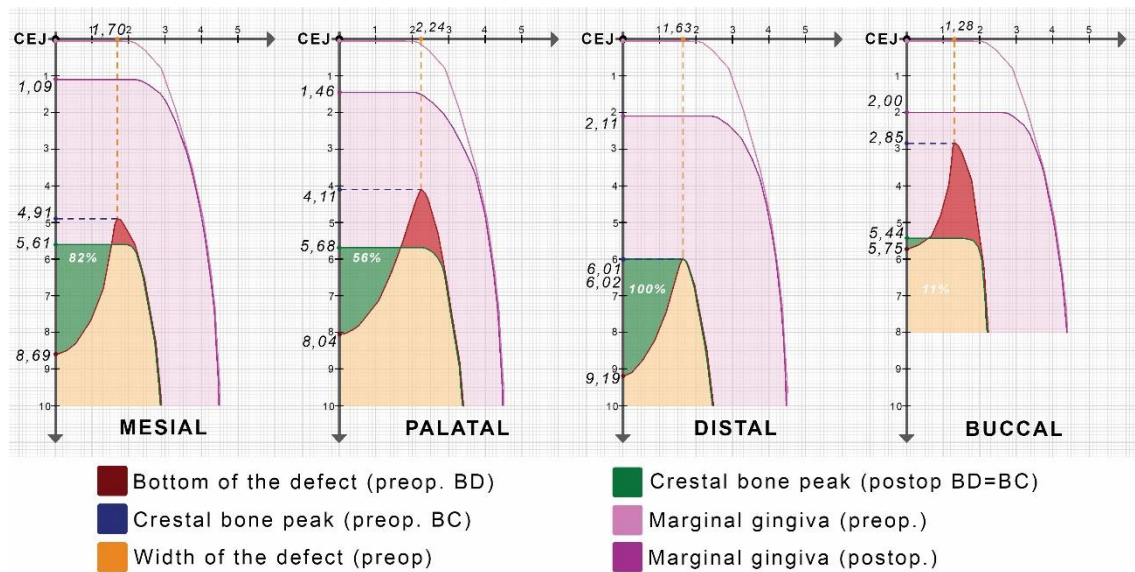


Figure 60: Schematic visualization of crestal bone changes around tooth 25 (165)

5.3 CBCT Subtraction Analysis of 3D Changes Following Alveolar Ridge Preservation: a case series of 10 patients with a 6-month follow-up

5.3.1 *Baseline patient demographics*

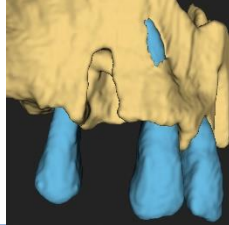
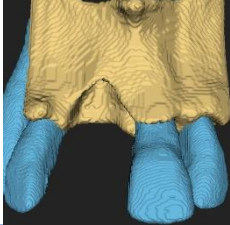
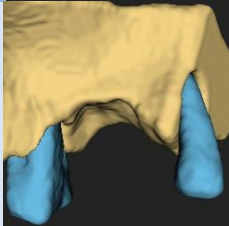
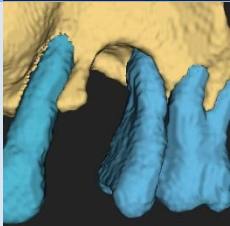
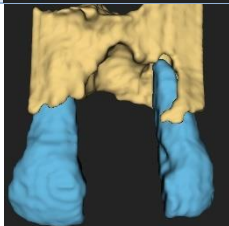
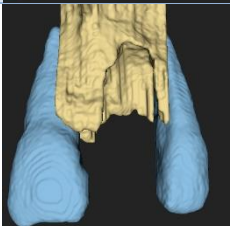
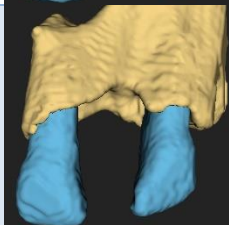
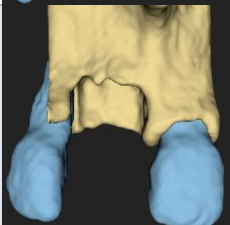
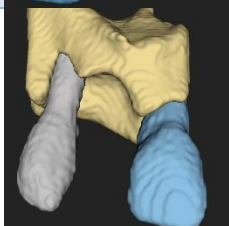
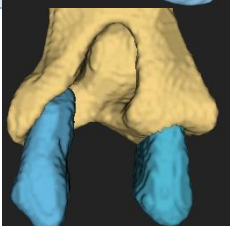
Ten patients with 10 single rooted teeth were enrolled in the study. Six patients were male, four patients were female. Their mean age was 42.70 ± 14.38 years. Out of 10 surgically treated teeth, 5 were upper central incisors, 1 was an upper lateral incisor, 1 was an upper canine, 1 was an upper first premolar, and 2 were upper second premolars. Seven teeth were extracted due to advanced periodontal lesions and three teeth due to endo-periodontal lesions caused by root fracture or internal root resorption.

5.3.2 *Volumetric and 3D morphological analysis*

5.3.2.1 *Baseline 3D defect morphology*

On 3D models acquired by the segmentation of baseline CBCT scans, extraction defect morphology was analyzed. Four cases were classified as EDS type 3 and six cases were classified as EDS class 4 extraction defects. Defect morphologies visible on 3D models correlated with the clinically determined extraction defect morphologies. Buccal bone dehiscences were present in all cases, and only three cases showed minor palatal bone loss. In six cases, alveolar ridge defects affected approximal root surfaces of one or both adjacent teeth. Baseline defect morphologies and EDS classifications are shown in **Table 11**.

Table 11: Baseline defect morphologies

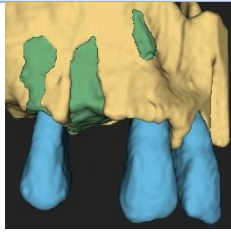
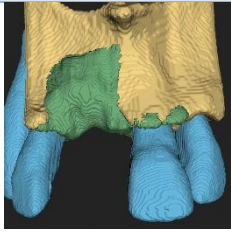
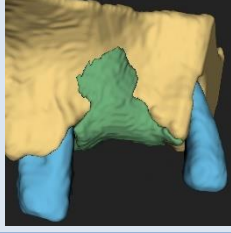
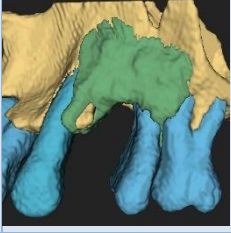

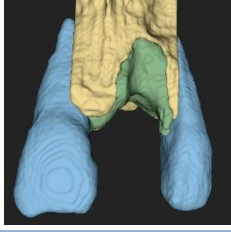
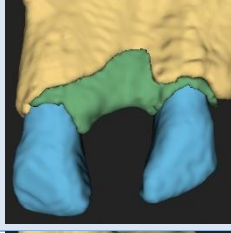
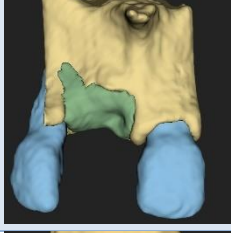
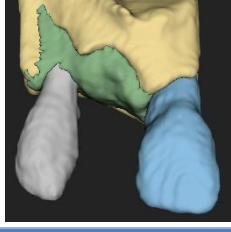
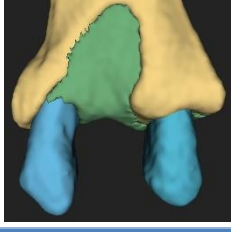
| Case | EDS classification | Case | EDS classification |
|---|--------------------|--|--------------------|
|  | Class 3 |  | Class 3 |
|  | Class 4 |  | Class 4 |
|  | Class 4 |  | Class 3 |
|  | Class 3 |  | Class 4 |
|  | Class 4 |  | Class 4 |

5.3.2.2 3D radiographic hard tissue alterations at 6-month follow-up

After subtraction of pre- and postoperative 3D models, volumetric hard tissue gain was analyzed and found to be $0.34 \text{ cm}^3 \pm 0.09 \text{ cm}^3$.

At the 6-month follow-up, the horizontal dimension of the edentulous ridge was maintained or even increased in some cases. In 6 cases where the loss of the proximal

bone at adjacent teeth was visible, previously exposed root surfaces were covered by newly formed hard tissues. Radiographic images of newly formed hard tissues resembled the trabecularization of native bone. Data are shown in *Table 12* (174).

| <i>Table 12: Volumetric hard tissue gain</i> | | | |
|---|--|--|--|
| Case | Volumetric hard tissue gain (cm ³) | Case | Volumetric hard tissue gain (cm ³) |
|  | 0.46 |  | 0.34 |
|  | 0.38 |  | 0.39 |
|  | 0.48 |  | 0.24 |
|  | 0.25 |  | 0.28 |
|  | 0.24 |  | 0.38 |
| Average | 0.34 cm ³ ± 0.09 cm ³ | | |

5.3.3 Linear evaluation of alveolar ridge alterations

Vertical linear measurements were taken midcrestally at the mesial, distal, and middle aspects of the extraction sites between the bottom of the extraction socket – the most coronal portion of the newly-formed, healed edentulous ridge. The mean vertical hard tissue change of was 5.97 ± 3.18 mm at the mesial, 6.40 ± 3.03 mm at the distal, and 7.01 ± 3.02 mm at the middle aspects of the treated sites.

Horizontal linear hard tissue changes were taken at the mesial, distal, and middle aspects between the maintained palatal marginal bone crest and the newly formed buccal bone. Average horizontal linear changes were 6.19 ± 0.68 mm at the mesial, 6.32 ± 1.52 mm at the distal, and 6.90 ± 1.48 mm at the middle aspects of the extraction sites. Data are summarized in **Table 13** (174).

Table 13: Horizontal and vertical linear change

| Patient | Horizontal change (mm) | | | Vertical change (mm) | | |
|---------|------------------------|-----------------|-----------------|----------------------|-----------------|-----------------|
| | Mesial | Middle | Distal | Mesial | Middle | Distal |
| 1. | 6.06 | 7.85 | 5.98 | 3.26 | 4.76 | 4.80 |
| 2. | 6.90 | 7.10 | 4.21 | 6.57 | 5.27 | 5.08 |
| 3. | 6.95 | 7.99 | 9.37 | 1.62 | 4.43 | 2.32 |
| 4. | 4.76 | 4.90 | 5.13 | 4.90 | 5.80 | 9.28 |
| 5. | 5.72 | 5.04 | 6.46 | 12.30 | 13.50 | 11.70 |
| 6. | 6.01 | 6.47 | 5.66 | 4.02 | 6.83 | 5.67 |
| 7. | 6.88 | 5.47 | 5.29 | 6.31 | 4.66 | 5.08 |
| 8. | 6.55 | 8.64 | 5.85 | 9.85 | 9.96 | 10.50 |
| 9. | 5.76 | 6.49 | 7.13 | 6.72 | 5.32 | 4.01 |
| 10. | 6.31 | 9.05 | 8.08 | 4.12 | 9.56 | 5.55 |
| Average | 6.19 ± 0.68 | 6.90 ± 1.48 | 6.32 ± 1.52 | 5.97 ± 3.18 | 7.01 ± 3.02 | 6.40 ± 3.03 |

5.4 Summary

Results must be analyzed on three levels. Firstly, it is important to analyze data regarding the model acquisition method by discussing the advantages and disadvantages compared to other methods. Secondly, the newly developed diagnostic and evaluation methods utilizing 3D models need to be discussed. In the third and final step clinical data acquired with the newly developed diagnostic and evaluation methods regarding the applied surgical techniques need to be analyzed and compared to similar studies found in the literature. The three-level analysis will be discussed in the “**DISCUSSION**” chapter.

6 DISCUSSION

6.1 LEVEL 1 - Digital hybrid model acquisition method

6.1.1 *Discussion of model preparation method*

With the presented method, 3D virtual hybrid models could be acquired and the morphology of periodontal and alveolar ridge defects were visualized. Virtual patient setup (36) was generated by combining 3D CBCT data and IOS data with a sequence of radiographic image segmentation, spatial registration, and CAD modeling.

In articles (1, 2, 86, 134, 135, 177, 178) where the authors described the application of 3D models for diagnosis and treatment planning, the segmentation of CBCT data was carried out using automatic thresholding algorithms (39-41). Conversely, our approach utilizes a newly developed dedicated semi-automatic segmentation method using segmentation tools found in the inventory of 3D Slicer. Elements of 3D model acquisition methods utilized in the field of general medicine (e.g., cardiac surgery, orthopedic surgery, thoracic surgery) have been implemented for dental applications (179-183).

The superimposition of IOS over CBCT data has been utilized in many surgical fields (1, 2, 4, 146, 149), however in most articles IOS was only projected over CBCT data without the application of CAD modeling and Boolean operators. In fact, a similar method for model acquisition has not been previously described in the literature (137).

6.1.2 *Advantages*

The introduced semi-automatic segmentation method can be utilized for the 3D reconstruction of not just CBCT datasets, but any type of volumetric radiographic image in DICOM (Digital Imaging and Communication in Medicine), such as conventional CT images and magnetic resonance images (MRI), regardless of image quality, whereas global thresholding algorithms only work reliably on high quality datasets (14, 15) and fail to visualize small details (e.g. periodontal defects) in 3D.

Complete manual segmentation of CBCT datasets has not been discussed so far, even though it is widely considered to be the gold standard for radiographic image segmentation (184) and many articles introducing new image segmentation modalities use manual segmentation as the control to validate the accuracy of their methods (42, 45, 47, 49, 185-187). However, this thesis is primarily focused on clinical applications, therefore validation of model accuracy was not investigated and complete manual segmentation of CBCT datasets was not performed in any of the studies. Comparison of the semi-automatic segmentation method and other image processing modalities can only be done based on literature data and personal experience. The advantage of the currently applied method over manual segmentation is the reduced duration of the process. Due to the lengthy procedure of generating labelmaps on every single slice of the dataset, the application of manual segmentation is not rational in clinical practice.

Conversely, previously mentioned (in section *1.2.1.4*) AI-based segmentation methods reduce the segmentation timeframe significantly (54, 56, 186, 187), however previously mentioned limitations (e.g., unreliable outcomes due to diverse input data, low availability, applicable only to the segmentation of specific types of defects) of AI segmentation methods compromise segmentation outcomes and thus limit their clinical application.

Construction of the virtual patient setup allowed us to analyze hard tissue defects in relation to the overlaying soft tissues. Bone, teeth, and soft tissues are separately represented in the virtual patient setup, therefore each step of the surgical intervention (i.e., incision, flap preparation, regenerative strategy, flap closure) can be predesigned and simulated virtually.

Guided implant placement is routinely performed in daily dental practice with high reliability (2, 188, 189). Nevertheless, implant positions are primarily planned on the planar views of the CBCT datasets due to the low-quality models acquired with global thresholding algorithms. With the clear 3D reconstruction of bone surfaces however, implant positions can be planned in 3D, enhancing the planning process.

The entire process was done using only free, open-source software (3D Slicer, Meshmixer®); users therefore do not have to invest in expensive planning software suites.

6.1.3 Disadvantages, future improvements

A significant drawback of the method is the relatively long duration and repetitive nature of the process, even though the model acquisition timeframe is shorter than when using manual segmentation. Certain aspects of the process could be automated (e.g., delineation, morphological interpolation, smoothing) (136, 138, 141, 142, 145), however some actions still require manual interaction which lengthens the process, such as separation of teeth and bone, and manual correction of metal artifacts. Additionally, users must be familiar with basic image processing and CAD modeling techniques.

Reduced segmentation times can be achieved with automatic segmentation methods (AI-based segmentation, global thresholding methods); the disadvantages of these methods were summarized in the previous section.

Another notable limitation of this process and related research is the lack of information regarding the accuracy of the models. The majority of the publications that investigate the accuracy of their methods perform the segmentation on CBCT and/or μ -CT scans of dry human skulls and compare results to a control group where 3D models were acquired with manual segmentation (42, 45, 47-49, 53, 54, 56, 178, 185-187). This thesis, however, is mainly focused on clinical applications, and accuracy was only moderately investigated. So far, mostly pilot studies have been conducted where the introduced semi-automatic segmentation method was utilized, however prior to future prospective trials the accuracy of the segmentation method must be addressed.

For another layer of realism, digital face scans utilizing mobile applications could be added in the future (144, 190, 191).

6.2 LEVEL 2 - 3D diagnostics and postoperative evaluation method

6.2.1 *Three-dimensional visualization of intrabony periodontal defects for regenerative surgical treatment planning*

6.2.1.1 *Discussion of 3D diagnostic method*

In the case series study describing the application of a novel semi-automatic segmentation method, 3D virtual models were utilized for the diagnosis and regenerative surgical treatment planning of intrabony periodontal defects (161). Clinical measurements (periodontal probing) IRs have been considered to be the gold standard for periodontal diagnostics, assessment of pretherapeutic single tooth prognosis, and periodontal surgical planning (63, 64, 93, 192) for over 40 years. Technological advancements in DMFR allowed the application of cone-beam computed tomography as a third diagnostic modality in periodontology. Since its introduction, many articles have investigated the application of CBCT scans for the diagnosis of periodontal lesions (16, 21, 66-69, 74-83, 193) and concluded that CBCT scans were superior to conventional diagnostic methods in the detection of furcation defects, three wall intrabony defects, midbuccal intrabony defects and dehiscence-type defects. However, systematic reviews and professional guidelines have stated that it should only be used when conventional methods are unable to provide an accurate diagnosis (66-69). The accuracy of various diagnostic modalities has been compared previously (77, 79, 80).

Grimard et al. assessed intrabony defect morphology and bone level changes with three different diagnostic methods (77). The authors compared the accuracy of periapical radiograph and CBCT measurement to direct intraoperative measurements. Datasets were reconstructed and MPR views of the examined area were acquired. Defect-involved interproximal tooth surfaces were oriented orthoradially for measurements. Conversely, our approach utilized reconstructed 3D models for linear CBCT measurements, therefore markup points could be placed in two different planes (in the same orientation). The mean difference in CEJ-BD values between CBCT and intrasurgical measurements was -0.9 ± 0.8 mm, while differences in CEJ-BC measurements averaged at 0.1 ± 1.2 mm. However, our study compared the horizontal (WIDTH) and vertical dimensions (INTRA)

of the intrabony component. A similar level of accuracy was detected: differences between digitally and intrasurgically measured INTRA and WIDTH values averaged 0.31 ± 0.21 mm and 0.41 ± 0.44 mm, respectively. Neither of the two research groups found significant differences between CBCT and intraoperative measurements, and they suggested that CBCT scans and segmented 3D models could be used reliably for the detection of intrabony periodontal defects. However, *Grimard et al.* found significantly less correlation between IR and intrasurgical measurements, subsequently concluding that linear measurements taken on IRs were significantly less accurate than CBCT measurements regarding all investigated parameters (77).

Two articles compared the detectability of furcation defects using clinical diagnostics and CBCT scans. *Cimbaljevic et al.* examined the agreement between the two diagnostic modalities and found that furcation defects were detected in only 46.9 % of all 174 examined sites with both diagnostic methods – meaning that 53.1 % of all areas with furcation involvement were undetected with clinical diagnostic methods. Hence, the authors suggested CBCT as an adjunct tool for the assessment of furcation defects in periodontitis cases (79). Additionally, our group assessed whether the grade of furcation defect was determinable with the two diagnostic modalities, and whether the grade of furcation defects could not be determined accurately with clinical examination and IRs. Similarly, in a recent article *Yusof et al.* compared the diagnostic accuracy of CBCT scans, IRs, and intraoperative linear measurements in the assessment of furcation defects. No significant difference was found between CBCT and direct intraoperative measurements. However, CBCT scans provided more information on hard tissue loss, vertical, and horizontal dimensions of furcation defects than periapical radiographs (80).

6.2.1.2 Advantages

CBCT scans were found to be superior to IRs and clinical examination methods in the detection of both intrabony periodontal defects and furcation defects (77, 79, 80). However, the majority of the previous articles did not generate 3D models of dental and alveolar structures. Few articles utilized 3D models for the diagnosis of periodontal intrabony defects (84-88). *Nemoto et al.*, *Tayman et al.* and *Gonçalves et al.* reconstructed

only the area of the defect to calculate the volume, but not the alveolar bone itself (84, 85, 87). Thus, periodontal bone topography could not be assessed. *Mohan et al.* utilized a global thresholding algorithm for 3D reconstruction; therefore teeth and alveolar bone could not be separated and resolution of the presented 3D model of a wide and deep intrabony defect was low (86). Contrarywise, in the 3D models utilized in our approach teeth are separated from the alveolar bone, thus periodontal defect morphology could be viewed more easily due to the clearly visible border between the two anatomical structures. The colors of the different components of the 3D model can be changed for an even better representation.

6.2.1.3 *Disadvantages, improvements*

When it comes to the diagnostic application of CBCT scans in periodontology, the number one concern is the elevated radiation dose when compared to conventional radiographic diagnostic modalities (i.e., IRs, panoramic X-rays). It was mentioned in section 1.1.1.1 that the effective radiation dose can vary greatly between CBCT machines of different manufacturers (14-16, 194). According to an article by *Pauwels et al.* the large FOV I-CAT FLX® scan used in this examination has an effective radiation dose of 83 μSv (194). This is about two times the effective dosage of a full-mouth periodontal status radiograph, comprised of 14 intraoral x-rays, with a cumulative radiation dose of about 40 μSv (195). However, if the added diagnostic benefit of the 3D models is taken into account based on the ALADAIP principle (19, 196), elevated radiation doses might be justified for the diagnosis of periodontal intrabony defects.

In this study, large FOV CBCT scans with a relatively low resolution (voxel size: 300 μm) were applied. Even though the presented semi-automatic segmentation method can be applied on any CBCT/ CT dataset, the quality of the 3D models however is greatly affected by the quality of the scans (larger voxel sizes, artifacts) (28, 197). Even though segmentations acquired with the semi-automatic method provide a detailed view of the 3D defect morphology, the quality of the 3D models could be further increased by optimizing CBCT exposure parameters.

Another drawback of this examination is the relatively small sample size (6 defects were enrolled). Even though statistical analysis was performed, further examinations on larger sample sizes with standardized measurements would need to be conducted to validate measurements thoroughly.

Contrary to the hybrid model preparation method described in **CHAPTER 3**, in this study only hard tissue models were utilized for diagnostic and treatment planning purposes. However, for even more detailed surgical planning incorporating all major steps of the surgical intervention (i.e., initial incision, flap elevation, surgical access, application of the regenerative strategy, wound closure) 3D soft tissue models (acquired with an IOS) must be included in the virtual patient setup.

To further expand the application of computer assisted technologies in periodontal regenerative surgery, virtual models can be manufactured with 3D printing technologies and models can be applied as intraoperative aids (198). With the continuing development of 3D bioprinting technologies, they are more and more prominently used in dental fields (199). In a case series study *Rasperini et al.* utilized a 3D printed polycaprolactone (PCL) scaffold for the regeneration of an intrabony periodontal defect. The presented case was unsuccessful in the long term, however improving the scaffold design by the application of more precise 3D models could result in favorable long-term outcomes (200). As it was presented by *Pellegrino et al.* an augmented reality (AR) setup can be used for dynamic implant navigation. Based on their idea, digital models could also be uploaded into an AR setup as an interactive aid to further increase the visualization of the surgical field (201).

6.2.2 *Virtual planning and volumetric evaluation in the regenerative-reconstructive surgical treatment of a complex periodontal defect*

6.2.2.1 *Discussion of 3D diagnostic and evaluation method*

In this published case report a two-staged regenerative-reconstructive treatment of a complex, multi-component periodontal defect was presented. In complex defect morphologies the application of 3D diagnostics is even more important than in singular intrabony defects. However, available literature data on the treatment of such complex defect morphologies is very limited. This is due to the morphological diversity of complex defects and therefore it is difficult to standardize treatment modalities. Nevertheless, based on the results of our previous studies and clinical experiments, it is safe to assume that 3D treatment planning is extremely beneficial in the treatment of multi-component periodontal and/or alveolar defects. Many of the limitations discussed in the previous (6.2.1.3) section have been addressed; model preparation and measurement methodology have also been improved compared to the previous case series study (165).

Digital linear measurements taken on the pre- and postoperative 3D models were based on the paper by *Cortellini et al.* where the authors described specific measurements for the intraoperative assessment of the initial periodontal defect morphologies (131). The authors also described the measurement process for a second re-entry surgery to assess hard tissue alterations directly. Direct bone measurements were found to be more accurate than the registration of pre- and postoperative clinical parameters, therefore it is widely considered to be the gold standard for the quantitative assessment of periodontal regeneration (128, 129). Our approach utilized 3D bone models for both pre- and postoperative assessment instead of direct bone measurement during a second re-entry procedure. The accuracy of CBCT images in periodontal diagnostics and in the evaluation of surgical results has already been discussed in sections 1.3.1.3, 1.5.1.1, and 6.2.1.1 (77, 79, 80, 84, 87, 88). Previous studies have described methods where the volumetric change after periodontal regenerative surgeries was presented, however both articles calculated the regenerated hard tissue volume by multiplying areas measured on 2D slices by the slice thickness (84, 88). Conversely, our method utilized 3D subtraction analysis to

determine the volumetric gain as well as analyze 3D morphological hard tissue alterations (as seen in section *1.5.1.1*).

The addition of IOS data in this case report study allowed us to plan all major surgical steps as was mentioned in section *6.2.1.3* and to assess soft tissue changes digitally, although virtual measurement of gingival recession (VREC) did not provide substantially more information compared to the clinical assessment of gingival recession.

6.2.2.2 Advantages

Many of the limitations discussed in the previous (*6.2.1.3*) study have been addressed and improved upon. IOS data have been included to acquire a hybrid model, and a 3D printed model of hard tissues was utilized as an intraoperative aid. Furthermore, the FOV of CBCT scans was reduced in order to increase the resolution without increasing the effective radiation dose. In fact, due to the available low dose protocol (21, 202) the effective radiation dose of the utilized single jaw CBCT scan is lower (60 μ Sv) than the large FOV I-CAT FLX® scan used in the previous study (83 μ Sv) (194).

Favorable clinical outcomes achieved with the described flap technique support our initial theory regarding the importance of virtual 3D planning and surgical simulation in minimally invasive flap designs. In this case report, three remote incisions (1 palatal paramarginal and 2 buccal pinhole incisions) with limited flap elevation were utilized to access the defects of tooth 24 and tooth 25. Incision and flap elevation were planned virtually and the most convenient access to the defect was determined prior to surgery on the virtual models.

Digital linear measurements and subtraction analysis provided deeper understanding of healing mechanisms that occur after the reconstructive treatment of complex periodontal defects. Besides hard tissue gain, marginal resorption around teeth and at the implant site could also be visualized. Linear measurements at 4 surfaces on each premolar allowed us to analyze horizontal and vertical hard tissue gain and once again the marginal resorption of bone peaks. Previously, marginal bone loss was rarely visualized, and the localization and the extent were not quantified, therefore specific reasons for this occurrence are thus far not known.

6.2.2.3 Disadvantages, future improvements

Even though many of the limitations described in the previous study have been addressed, there is still room for improvements. Thorough analysis of periodontal regeneration has been executed, by linear and volumetric measurements; the most objective validation of periodontal new attachment formation would be to measure its root surface area. Area-based evaluation has not yet been demonstrated in the literature, however our group has made steps towards the development of such a method.

The greatest disadvantage of this study was that it only reported results from one single case, therefore precautions must be taken before deriving any conclusions. Unfortunately, the uniqueness of the defect morphology and novelty of the treatment approach are the greatest drawbacks of this study. Due to the diversity in morphologies of complex periodontal defects it is difficult to develop a standardized treatment approach and to conduct prospective case studies.

6.2.3 CBCT Subtraction Analysis of 3D Changes Following Alveolar Ridge Preservation: a case series of 10 patients with a 6-month follow-up

6.2.3.1 Discussion of 3D evaluation method

Besides the application of the three-dimensional models in periodontal diagnostics and postoperative evaluation, another aim of the current thesis was to validate surgical outcomes following alveolar ridge preservation utilizing the extraction site development technique (XSD) (115). In the previous section (6.2.2) 3D subtraction analysis was utilized to assess hard tissue changes after the two-staged (1. stage: XSD; 2. stage reconstructive periodontal surgery) treatment of a complex periodontal defect, and results were already briefly discussed. However, in this study surgical outcomes following the ARP of EDS type 3 and EDS type 4 (95) singular extraction defects were evaluated. Results after XSD were already examined in the initial publication, however authors utilized a linear measurement to determine the gain of new tissues (174).

6.2.3.2 Advantages

The two studies utilized slightly different measurement approaches, hence the notable difference between results. In our case series article, both volumetric and linear measurements were performed on the reconstructed 3D models, whereas *Windisch et al.* performed linear and planimetric measurements on 2D orthoradially oriented MPR views of the CBCT dataset. In their study, horizontal linear hard tissue changes were measured from the buccal cortical wall; in our approach linear differences were measured between the palatal bone wall and the most buccal extent of the newly formed edentulous ridge. Similar differences can be noted in case of vertical linear measurements. In their study *Windisch et al.* measured linear vertical changes on both palatal and buccal aspects, whereas in our approach vertical linear differences were measured midcrestally. Three-dimensional evaluation, however, provides clinically and scientifically more relevant information regarding healing mechanisms of extraction defects treated with the XSD approach than linear measurements; hence it was selected as the primary objective of our study.

In their study, *Chappuis et al.* examined ridge alterations following tooth extraction (spontaneous healing) on 3D virtual models (134). On high resolution small FOV CBCT scans, the authors acquired 3D surface models utilizing an automatic segmentation method. Following segmentation, both pre- and postoperative datasets were superimposed based on anatomical landmarks. Ridge alterations were visualized by color-coded zones, and linear measurements were taken at the most coronal part of the extraction socket. Similar to the article by *Windisch et al.*, dimensional changes were calculated from linear measurements instead of calculating the volume of the newly formed (or resorbed) hard tissues. Our approach utilized a semi-automatic segmentation method, and different anatomical structures could be segmented separately. On the other hand, *Chappuis et al.* utilized global thresholding algorithms, therefore the effects of tooth extraction on adjacent teeth could not be analyzed. Spatial alignment in their study was executed by selecting identical points; in order to reduce the duration and increase accuracy of the spatial registration in our study an automatic alignment algorithm was utilized (175).

6.2.3.3 Disadvantages, future improvements

Limitations discussed in the previous two sections (**6.1.3**; 6.2.1.3; 6.2.2.3) are essentially relevant in this case as well. Therefore, the relatively long duration of the model acquisition process and the fact that only hard tissue models (IOS scans were not included) were utilized to assess outcomes can still be mentioned as limitations. The inclusion of IOS data would allow the assessment of post-extraction soft tissue dimensional changes. It must be noted that due to the retrospective nature of the study CBCT imaging parameters were not standardized, which may have affected study outcomes.

It was briefly mentioned that extraction and consequent ARP had an indirect effect on the healing of defects at adjacent tooth surfaces, however this was not examined further because at the time of manuscript preparation the methodology was not sufficiently refined. Since then, our group has developed the methodology to assess the formation of new periodontal attachment based on root surface area calculations.

6.3 LEVEL 3 - Analysis of clinical outcomes

In the previous two sections results of the model acquisition method as well as 3D diagnostic and evaluation methods were discussed. In this section, clinical results of the studies – which are only possible to assess with the clinical application of 3D technology – will be discussed.

6.3.1 Three-dimensional visualization of intrabony periodontal defects for regenerative surgical treatment planning

In this study our group utilized a relatively subjective, but practical method to compare the diagnostic accuracy of intraoral radiographs and CBCT scans. From a clinician's perspective the examined defect characteristics are the primary defect-related factors that determine the surgical modality. If these defect characteristics cannot be determined correctly it might be necessary to alter the treatment strategy during surgical intervention which may compromise clinical outcomes. Based on IRs, the general morphology (horizontal or vertical) could be determined in four cases. In one case where the three-wall intrabony component of a horizonto-vertical defect was located on the palatal aspect the intrabony component could not be detected by the expert clinician. General defect morphology was not determined correctly around an upper second molar. The number of affected root surfaces was almost always underestimated because the area of the defect extending to the midbuccal or midlingual/midpalatal aspect could not be detected on IRs. Consequently, if 3D models were not utilized the surgical access may not be determined correctly and defects could not be debrided completely. Due to overlapping lingual and buccal cortical, estimating the number of bony walls was difficult on IRs, hence it was correctly determined in only one case. Furcation involvement is one of the most difficult aspects to determine on IRs and therefore it is the most common indication for taking CBCT scans prior to surgical treatment (68, 69, 78, 79, 81, 83, 85).

In summary, all four defect characteristics were assessed accurately in only one case with IRs and direct clinical measurements, although all four defect characteristics could be determined correctly. Conversely, with the application of the 3D models generated with

the presented semi-automatic segmentation method, all four defect characteristics could be determined in all cases.

Literature data was supported by our results, as the grade of furcation defects could not be determined in any of the cases. The findings of our study correlate with clinical data regarding the inaccuracy of IRs in the detection of midbuccal/lingual/palatal intrabony defects, three-wall intrabony defects, dehiscence type defects, and furcation defects. Our study also found that specific surgical treatment influencing defect characteristics could not be determined on IRs, therefore clinical application of 3D models acquired by CBCT segmentation could be justified in periodontal diagnosis and treatment planning (161).

6.3.2 Virtual planning and volumetric evaluation in the regenerative-reconstructive surgical treatment of a complex periodontal defect

In this additional case report, diagnosis, treatment planning, and surgical results were also evaluated utilizing 3D technology. Pre-and postoperative hybrid models incorporating 3D data of CBCTs and IOSs were utilized during the two-stage treatment approach.

It was previously emphasized that extraction and consequent alveolar ridge preservation may have indirect positive effects on adjacent tooth surfaces, however this was not examined thoroughly. Linear CBCT measurements were taken and intrabony defect fill was calculated by the ratio of postoperative intrabony hard tissue gain and the depth of the intrabony component (INTRA) at baseline. Out of all 8 assessed tooth surfaces, complete resolution of the intrabony component (100% defect fill) was only found at the distal surface of tooth 25 – significantly greater than the 35-72% values found in the literature (203, 204). Based on our previous clinical experience it can be assumed that this more favorable outcome was induced by the first, XSD procedure. However, more thorough examination on large sample sizes and a refined evaluation method is necessary to derive further conclusions. Additionally, increased postoperative blood clot stability achieved by a limited flap elevation also contributed to a more favorable surgical outcome (113).

Both three-dimensional evaluation and linear measurements visualized the slight marginal resorption at the palatal, buccal, and interdental aspect of teeth 24 and 25. However, the exact causes cannot be determined due to the limited data. A slight marginal palatal crestal bone resorption could also be detected at the extraction site of tooth 26, while hard tissue gain – even slightly beyond the bony envelope – was visible on the buccal aspect. This is due to the fact that the XSD technique aims to preserve the buccal cortical bone, although slight resorption of the palatal crest is clinically irrelevant to future implant position.

The quality of hard tissue composition and bone microstructure, however, cannot be assessed on CBCT datasets due to their relative low resolution (205, 206). Therefore, clinical measurements (PPD, CAL, REC) need to support radiographic findings in order to validate positive outcomes. In this case, clinical measurements confirmed radiographic findings, however previous studies often reported unfavorable results when intrabony periodontal defects were treated with a combined approach (GTR + BDX). Due to occasional connective tissue encapsulation of xenograft particles, radiographic and clinical results did not correlate with the histological findings (207-209).

With 3D subtraction analysis, the cumulative volume of newly formed and resorbed hard tissues could be measured, however from a clinical perspective the evaluation of morphological changes gives more relevant information regarding the healing mechanisms. Thorough analysis of defect healing allows the retrospective evaluation of the surgical modality and may indicate certain aspects of the surgical procedure that would have to be improved upon (165).

6.3.3 CBCT Subtraction Analysis of 3D Changes Following Alveolar Ridge Preservation: a case series of 10 patients with a 6-month follow-up

This study examined the volumetric and 3D morphological changes of advanced extraction defect morphologies (EDS type 3, EDS type 4) following XSD procedure. Single rooted teeth were extracted due to periodontal or endo-periodontal lesions. With volumetric evaluation an average of $0.34 \text{ cm}^3 \pm 0.09 \text{ cm}^3$ hard tissue gain could be achieved following extraction and subsequent ARP of periodontally (or endo-

periodontally) involved teeth. In a more recent article, *Ben Amara et al.* examined the efficacy of ARP in case of periodontally involved teeth. The authors utilized the combination of BDX (for socket fill) and site coverage with double-layer collagen membrane for ARP and compared the results to spontaneous healing. Even though more favorable results were achieved with ARP, both groups presented volumetric hard tissue loss. In their study, using ARP the volumetric hard tissue loss was found to be $0.027 \text{ cm}^3 \pm 0.039 \text{ cm}^3$, whereas in case of treatment with the XSD technique a volumetric hard tissue gain of $0.34 \text{ cm}^3 \pm 0.09 \text{ cm}^3$ was observed. A detailed description of extraction defect morphologies was not provided in their examination; however the authors mentioned the presence of bone dehiscence at one of the socket walls.

Unlike most ARP procedures (116, 118, 119, 122, 123, 135, 210) XSD does not utilize xenogeneic particulate grafts, which may interfere with the natural healing process of the post-extraction wound. Many articles including systematic reviews have concluded that xenograft particles may compromise the quality of newly formed hard tissues (118). Radiographic images of extraction sites treated with the XSD technique show a trabecular structure that resembles the radiographic appearance of native bone. However, without histological evidence the quality of newly formed hard tissues cannot be assessed.

Previously it was emphasized that the XSD technique has a positive effect on hard tissue regeneration at periodontally affected adjacent tooth surfaces. Due to the 3D evaluation, it was visualized in a few cases that previously exposed adjacent root surfaces were covered with hard tissues after XSD, however further evaluation is necessary (174).

7 CONCLUSIONS

It can be concluded that the described 3D digital workflow can be utilized for a wide variety of applications in the field of periodontal regenerative-reconstructive surgery and implant dentistry.

With the application of a dedicated radiographic image segmentation method, 3D virtual models can be generated from CBCT datasets, facilitating 3D morphology of dental and alveolar structures. Compared to widely utilized global thresholding segmentation methods, the described method provides a more realistic 3D representation of CBCT datasets. Results are not (or are only slightly) compromised by artifacts, and teeth can be separated from the surrounding alveolar bone. With the inclusion of IOS data a soft tissue layer can be added to the segmented CBCT models. The generated virtual patient setup depicts the clinical situation realistically, thus allowing the digital planning of each surgical step.

Three-dimensional models acquired with CBCT segmentation provide more diagnostic information on periodontal defect morphologies than conventional 2D intraoral radiographs, clinical probing, or planar CBCT images. Therefore, it can be utilized as an additional diagnostic tool in periodontology in cases where conventional periodontal diagnostic modalities are unable to provide sufficient information on defect morphologies. Three-dimensional reconstruction of CBCT datasets can be especially useful in the planning of complex periodontal defects.

Volumetric evaluation of hard tissue changes after different surgical intervention (e.g., periodontal regenerative surgery, alveolar ridge preservation, or alveolar ridge augmentation) provides a deeper understanding of tissue healing. Even though qualitative assessment can only be performed by histological analysis, 3D evaluation is an objective method that overcomes several limitations of direct bone measurements as well as clinical and conventional radiographic evaluation methods. With 3D morphological analysis of tissue alterations following regenerative-reconstructive surgeries, the effects of surgical flap elevation and different regenerative strategies on tissue healing can be visualized in three dimensions, thereby generating feedback on the effectiveness of the surgical treatment. With a thorough 3D analysis of the results the advantages and disadvantages

of the surgical intervention can be analyzed. Thus, different aspects of the surgical treatment, such as incision, flap elevation, and regenerative strategy, could be improved further.

Besides the clinical benefits of the currently described digital workflow in regenerative-reconstructive periodontal surgery and implant dentistry, previously described studies have a few notable limitations that should be addressed in the future. The radiographic imaging protocol should be standardized to acquire high quality CBCT scans and 3D segmented models. The timeframe of image segmentation and CAD modeling needs to be reduced significantly in favor of a more efficient and user-friendly approach. Lastly, future prospective clinical studies must be conducted in order to further validate clinical results acquired with this three-dimensional approach.

8 SUMMARY – ENGLISH

Objective of this thesis was to present a completely digital workflow in reconstructive periodontal surgery and implant dentistry incorporating the application of 3D virtual models to aid treatment planning, surgical intervention, and postoperative evaluation. Our digital approach comprises of the following stages: (i) digital data acquisition, (ii) digital data processing, (iii) virtual surgical planning, (iv) computer-aided surgical procedure, and (v) three-dimensional postoperative evaluation.

In the first part steps of a **model acquisition method** were detailed consisting of (i) semi-automatic image segmentation, (ii) spatial alignment, and (iii) CAD modeling. In the second part, various **clinical applications** within the framework of the digital workflow were discussed. Including: (i) three-dimensional visualization of intrabony periodontal defects, (ii) presentation of a completely digital workflow in the regenerative-reconstructive treatment of complex periodontal-alveolar ridge defect, and (iii) subtraction analysis of volumetric and morphological hard tissue alterations following ARP.

Acquired 3D models provide more diagnostic information on periodontal defect morphologies than conventional 2D intraoral radiographs, clinical probing, or planar CBCT images. Therefore, it can be utilized as an additional diagnostic tool in periodontology in cases where conventional periodontal diagnostic modalities are unable to provide sufficient information on defect morphologies. Volumetric evaluation of hard tissue changes after different surgical intervention (e.g., periodontal regenerative surgery, alveolar ridge preservation, or alveolar ridge augmentation) on the other hand provides a deeper understanding of tissue healing.

9 SUMMARY – HUNGARIAN

Jelen disszertáció célja, hogy bemutassa az általunk kifejlesztett teljesen digitális munkafolyamat lépéseit, valamint a 3D technológia alkalmazásának lehetőségeit a rekonstruktív parodontális sebészetben és az implantológiában. Az alkalmazott munkafolyamat lépései: (i) digitális adatgyűjtés, (ii) digitális adatfeldolgozás, (iii) virtuális műtéti tervezés, (iv) számítógép által támogatott sebészi beavatkozás és (v) műtéti eredmények három-dimenziós kiértékelése.

A elsőként a virtuális modellalkotás egyes lépéseinek részletes ismertetését végeztük, mely az alábbi fázisokból áll: (i) fél-automatikus radiológiai képfeldolgozás (szegmentáció), (ii) adatok térbeli illesztése és (iii) CAD modellezés. Módszerek ismeretetésének második részében az előállított virtuális 3D modellek különböző lehetséges alkalmazásait mutattuk be. Ezek a következők: (i) intraoszer parodontális defektusok három-dimenziós megjelenítése, (ii) digitális munkafolyamat alkalmazása a regeneratív-rekonstruktív parodontális sebészetben és (iii) alveolus prezervációt követő keményszöveti változások 3D szubtrakciós analízise.

Összegezhető, hogy az előállított 3D modellek több információt biztosítanak intraoszer defektusok morfológiájáról, mint a konvencionális radiológiai képalkotó eljárások, klinikai vizsgálómódszerek vagy CBCT felvételek két-dimenziós metszetei. Ennek következtében a jelen tézisben leírt 3D diagnosztikai módszer alkalmas parodontális intraoszer defektusok vizsgálatára, ha az előbb említett konvencionális diagnosztikus eljárások nem biztosítanak kellő információt a műtéti tervezéshez. Keményszöveti változások volumetrikus kiértékelése különböző rekonstruktív eljárások után lehetővé teszi a gyógyulás mechanizmusának pontosabb megértését.

10 BIBLIOGRAPHY

1. Güth JF, Kauling AEC, Schweiger J, Kühnisch J, Stimmelmayer M. (2017) Virtual Simulation of Periodontal Surgery Including Presurgical CAD/CAM Fabrication of Tooth-Colored Removable Splints on the Basis of CBCT Data: A Case Report. *Int J Periodontics Restorative Dent*, 37: e310-e320.
2. Ganz SD. (2015) Three-dimensional imaging and guided surgery for dental implants. *Dent Clin North Am*, 59: 265-290.
3. van der Meer WJ, Vissink A, Ng YL, Gulabivala K. (2016) 3D Computer aided treatment planning in endodontics. *J Dent*, 45: 67-72.
4. Xia JJ, Gateno J, Teichgraeber JF, Yuan P, Chen KC, Li J, Zhang X, Tang Z, Alfi DM. (2015) Algorithm for planning a double-jaw orthognathic surgery using a computer-aided surgical simulation (CASS) protocol. Part 1: planning sequence. *Int J Oral Maxillofac Surg*, 44: 1431-1440.
5. Papadiochou S, Pissiotis AL. (2018) Marginal adaptation and CAD-CAM technology: A systematic review of restorative material and fabrication techniques. *J Prosthet Dent*, 119: 545-551.
6. Baan F, de Waard O, Bruggink R, Xi T, Ongkosuwito EM, Maal TJJ. (2020) Virtual setup in orthodontics: planning and evaluation. *Clin Oral Investig*, 24: 2385-2393.
7. Mangano FG, Hauschild U, Admakin O. (2018) Full in-Office Guided Surgery with Open Selective Tooth-Supported Templates: A Prospective Clinical Study on 20 Patients. *Int J Environ Res Public Health*, 15.
8. Matsumoto JS, Morris JM, Foley TA, Williamson EE, Leng S, McGee KP, Kuhlmann JL, Nesberg LE, Vrtiska TJ. (2015) Three-dimensional Physical Modeling: Applications and Experience at Mayo Clinic. *Radiographics*, 35: 1989-2006.
9. Abdullah KA, Reed W. (2018) 3D printing in medical imaging and healthcare services. *J Med Radiat Sci*, 65: 237-239.
10. Mitsouras D, Liacouras P, Imanzadeh A, Giannopoulos AA, Cai T, Kumamaru KK, George E, Wake N, Caterson EJ, Pomahac B, Ho VB, Grant GT, Rybicki FJ. (2015) Medical 3D Printing for the Radiologist. *Radiographics*, 35: 1965-1988.

11. Moser N, Santander P, Quast A. (2018) From 3D imaging to 3D printing in dentistry - a practical guide. *Int J Comput Dent*, 21: 345-356.
12. Evens RG. (1995) Röntgen retrospective. One hundred years of a revolutionary technology. *Jama*, 274: 912-916.
13. Mozzo P, Procacci C, Tacconi A, Martini PT, Andreis IA. (1998) A new volumetric CT machine for dental imaging based on the cone-beam technique: preliminary results. *Eur Radiol*, 8: 1558-1564.
14. Jacobs R, Salmon B, Codari M, Hassan B, Bornstein MM. (2018) Cone beam computed tomography in implant dentistry: recommendations for clinical use. *BMC Oral Health*, 18: 88.
15. Jacobs R. (2011) Dental cone beam CT and its justified use in oral health care. *Jbr-btr*, 94: 254-265.
16. Bornstein MM, Scarfe WC, Vaughn VM, Jacobs R. (2014) Cone beam computed tomography in implant dentistry: a systematic review focusing on guidelines, indications, and radiation dose risks. *Int J Oral Maxillofac Implants*, 29 Suppl: 55-77.
17. Harris D, Horner K, Gröndahl K, Jacobs R, Helmrot E, Benic GI, Bornstein MM, Dawood A, Quirynen M. (2012) E.A.O. guidelines for the use of diagnostic imaging in implant dentistry 2011. A consensus workshop organized by the European Association for Osseointegration at the Medical University of Warsaw. *Clin Oral Implants Res*, 23: 1243-1253.
18. Hendee WR, Edwards FM. (1986) ALARA and an integrated approach to radiation protection. *Semin Nucl Med*, 16: 142-150.
19. Oenning AC, Jacobs R, Pauwels R, Stratis A, Hedesi M, Salmon B. (2018) Cone-beam CT in paediatric dentistry: DIMITRA project position statement. *Pediatr Radiol*, 48: 308-316.
20. Hidalgo Rivas JA, Horner K, Thiruvengkatachari B, Davies J, Theodorakou C. (2015) Development of a low-dose protocol for cone beam CT examinations of the anterior maxilla in children. *Br J Radiol*, 88: 20150559.
21. Yeung AWK, Jacobs R, Bornstein MM. (2019) Novel low-dose protocols using cone beam computed tomography in dental medicine: a review focusing on

- indications, limitations, and future possibilities. *Clin Oral Investig*, 23: 2573-2581.
22. Dawood A, Brown J, Sauret-Jackson V, Purkayastha S. (2012) Optimization of cone beam CT exposure for pre-surgical evaluation of the implant site. *Dentomaxillofac Radiol*, 41: 70-74.
 23. Al-Okshi A, Theodorakou C, Lindh C. (2017) Dose optimization for assessment of periodontal structures in cone beam CT examinations. *Dentomaxillofac Radiol*, 46: 20160311.
 24. Katsumata A, Hirukawa A, Okumura S, Naitoh M, Fujishita M, Ariji E, Langlais RP. (2009) Relationship between density variability and imaging volume size in cone-beam computerized tomographic scanning of the maxillofacial region: an in vitro study. *Oral Surg Oral Med Oral Pathol Oral Radiol Endod*, 107: 420-425.
 25. Jacobs R, Quirynen M. (2014) Dental cone beam computed tomography: justification for use in planning oral implant placement. *Periodontol 2000*, 66: 203-213.
 26. Kuusisto N, Vallittu PK, Lassila LV, Huumonen S. (2015) Evaluation of intensity of artefacts in CBCT by radio-opacity of composite simulation models of implants in vitro. *Dentomaxillofac Radiol*, 44: 20140157.
 27. Schulze R, Heil U, Gross D, Bruellmann DD, Dranischnikow E, Schwanecke U, Schoemer E. (2011) Artefacts in CBCT: a review. *Dentomaxillofac Radiol*, 40: 265-273.
 28. Queiroz PM, Oliveira ML, Groppo FC, Haiter-Neto F, Freitas DQ. (2018) Evaluation of metal artefact reduction in cone-beam computed tomography images of different dental materials. *Clin Oral Investig*, 22: 419-423.
 29. Mörmann WH. (2004) The origin of the Cerec method: a personal review of the first 5 years. *Int J Comput Dent*, 7: 11-24.
 30. Mörmann WH, Brandestini M, Lutz F. (1987) [The Cerec system: computer-assisted preparation of direct ceramic inlays in 1 setting]. *Quintessenz*, 38: 457-470.
 31. Leinfelder KF, Isenberg BP, Essig ME. (1989) A new method for generating ceramic restorations: a CAD-CAM system. *J Am Dent Assoc*, 118: 703-707.

32. Joda T, Brägger U. (2015) Digital vs. conventional implant prosthetic workflows: a cost/time analysis. *Clin Oral Implants Res*, 26: 1430-1435.
33. Joda T, Zarone F, Ferrari M. (2017) The complete digital workflow in fixed prosthodontics: a systematic review. *BMC Oral Health*, 17: 124.
34. Meier B, Wiemer KB, Miethke RR. (2003) Invisalign--patient profiling. Analysis of a prospective survey. *J Orofac Orthop*, 64: 352-358.
35. Lagravère MO, Flores-Mir C. (2005) The treatment effects of Invisalign orthodontic aligners: a systematic review. *J Am Dent Assoc*, 136: 1724-1729.
36. Vandenberghe B. (2018) The digital patient - Imaging science in dentistry. *J Dent*, 74 Suppl 1: S21-s26.
37. Rekow ED. (2020) Digital dentistry: The new state of the art - Is it disruptive or destructive? *Dent Mater*, 36: 9-24.
38. Hendriks CLL, Malm P, Bengtsson E. Rapid Prototyping of Image Analysis Applications. In: Dougherty G (szerk.), *Medical Image Processing: Techniques and Applications*, doi:10.1007/978-1-4419-9779-1_2. Springer New York, New York, NY, 2011: 5-25.
39. Suetens P, Bellon E, Vandermeulen D, Smet M, Marchal G, Nuyts J, Mortelmans L. (1993) Image segmentation: methods and applications in diagnostic radiology and nuclear medicine. *Eur J Radiol*, 17: 14-21.
40. Stolojescu-Crisan C, Stefan H. (2013) A Comparison of X-Ray Image Segmentation Techniques. *Advances in Electrical and Computer Engineering*, 3.
41. Friedli L, Kloukos D, Kanavakis G, Halazonetis D, Gkantidis N. (2020) The effect of threshold level on bone segmentation of cranial base structures from CT and CBCT images. *Sci Rep*, 10: 7361.
42. Michetti J, Basarab A, Diemer F, Kouame D. (2017) Comparison of an adaptive local thresholding method on CBCT and μ CT endodontic images. *Phys Med Biol*, 63: 015020.
43. Johari M, Esmaeili F, Andalib A, Garjani S, Saberkari H. (2016) A Novel Thresholding Based Algorithm for Detection of Vertical Root Fracture in Nonendodontically Treated Premolar Teeth. *J Med Signals Sens*, 6: 81-90.
44. Palus H. HOMOGENEITY CRITERIA FOR REGION-GROWING IMAGE SEGMENTATION IN IHS COLOUR SPACE, 1998.

45. Jiang Y, Qian J, Lu S, Tao Y, Lin J, Lin H. (2021) LRVRG: a local region-based variational region growing algorithm for fast mandible segmentation from CBCT images. *Oral Radiol*, doi:10.1007/s11282-020-00503-5.
46. Xi T, Schreurs R, Heerink WJ, Bergé SJ, Maal TJ. (2014) A novel region-growing based semi-automatic segmentation protocol for three-dimensional condylar reconstruction using cone beam computed tomography (CBCT). *PLoS One*, 9: e111126.
47. Fan Y, Beare R, Matthews H, Schneider P, Kilpatrick N, Clement J, Claes P, Penington A, Adamson C. (2019) Marker-based watershed transform method for fully automatic mandibular segmentation from CBCT images. *Dentomaxillofac Radiol*, 48: 20180261.
48. Kakehbaraei S, Seyedarabi H, Zenouz AT. (2018) Dental Segmentation in Cone-beam Computed Tomography Images Using Watershed and Morphology Operators. *J Med Signals Sens*, 8: 119-124.
49. Naumovich SS, Naumovich SA, Goncharenko VG. (2015) Three-dimensional reconstruction of teeth and jaws based on segmentation of CT images using watershed transformation. *Dentomaxillofac Radiol*, 44: 20140313.
50. Burger W, Burge MJ. Detecting Simple Curves. In: Burger W, Burge MJ (szerk.), *Principles of Digital Image Processing: Core Algorithms*, doi:10.1007/978-1-84800-195-4_3. Springer London, London, 2009: 1-19.
51. Bozek J, Mustra M, Delac K, Grgic M. A Survey of Image Processing Algorithms in Digital Mammography. In: Grgic M, Delac K, Ghanbari M (szerk.), *Recent Advances in Multimedia Signal Processing and Communications*, doi:10.1007/978-3-642-02900-4_24. Springer Berlin Heidelberg, Berlin, Heidelberg, 2009: 631-657.
52. Pauwels R, Jacobs R, Bosmans H, Pittayapat P, Kosalagood P, Silkosessak O, Panmekiate S. (2014) Automated implant segmentation in cone-beam CT using edge detection and particle counting. *Int J Comput Assist Radiol Surg*, 9: 733-743.
53. Michetti J, Georgelin-Gurgel M, Mallet JP, Diemer F, Boulanouar K. (2015) Influence of CBCT parameters on the output of an automatic edge-detection-based endodontic segmentation. *Dentomaxillofac Radiol*, 44: 20140413.

54. Cardenas CE, Yang J, Anderson BM, Court LE, Brock KB. (2019) Advances in Auto-Segmentation. *Semin Radiat Oncol*, 29: 185-197.
55. Bishop C. Pattern Recognition and Machine Learning. In: Vol. 16, 2006: 140-155.
56. Currie G, Hawk KE, Rohren E, Vial A, Klein R. (2019) Machine Learning and Deep Learning in Medical Imaging: Intelligent Imaging. *J Med Imaging Radiat Sci*, 50: 477-487.
57. Leite AF, Vasconcelos KF, Willems H, Jacobs R. (2020) Radiomics and Machine Learning in Oral Healthcare. *Proteomics Clin Appl*, 14: e1900040.
58. Hung K, Yeung AWK, Tanaka R, Bornstein MM. (2020) Current Applications, Opportunities, and Limitations of AI for 3D Imaging in Dental Research and Practice. *Int J Environ Res Public Health*, 17.
59. Rosenman MA, Smith G, Maher ML, Ding L, Marchant D. (2007) Multidisciplinary collaborative design in virtual environments. *Automation in Construction*, 16: 37-44.
60. Tovey M, Owen J. (2000) Sketching and direct CAD modelling in automotive design. *Design Studies*, 21: 569-588.
61. Kamio T, Suzuki M, Asaumi R, Kawai T. (2020) DICOM segmentation and STL creation for 3D printing: a process and software package comparison for osseous anatomy. *3D Print Med*, 6: 17.
62. Hur SM, Kim HC, Lee SH. (2002) STL File Generation with Data Reduction by the Delaunay Triangulation Method in Reverse Engineering. *The International Journal of Advanced Manufacturing Technology*, 19: 669-678.
63. Listgarten MA. (1980) Periodontal probing: what does it mean? *J Clin Periodontol*, 7: 165-176.
64. Lang NP, Hill RW. (1977) Radiographs in periodontics. *J Clin Periodontol*, 4: 16-28.
65. Papapanou PN, Sanz M, Buduneli N, Dietrich T, Feres M, Fine DH, Flemmig TF, Garcia R, Giannobile WV, Graziani F, Greenwell H, Herrera D, Kao RT, Kebschull M, Kinane DF, Kirkwood KL, Kocher T, Kornman KS, Kumar PS, Loos BG, Machtei E, Meng H, Mombelli A, Needleman I, Offenbacher S, Seymour GJ, Teles R, Tonetti MS. (2018) Periodontitis: Consensus report of

- workgroup 2 of the 2017 World Workshop on the Classification of Periodontal and Peri-Implant Diseases and Conditions. *J Periodontol*, 89 Suppl 1: S173-s182.
66. Mandelaris GA, Scheyer ET, Evans M, Kim D, McAllister B, Nevins ML, Rios HF, Sarment D. (2017) American Academy of Periodontology Best Evidence Consensus Statement on Selected Oral Applications for Cone-Beam Computed Tomography. *J Periodontol*, 88: 939-945.
 67. Scarfe WC, Azevedo B, Pinheiro LR, Priaminiarti M, Sales MAO. (2017) The emerging role of maxillofacial radiology in the diagnosis and management of patients with complex periodontitis. *Periodontol 2000*, 74: 116-139.
 68. Walter C, Schmidt JC, Dula K, Sculean A. (2016) Cone beam computed tomography (CBCT) for diagnosis and treatment planning in periodontology: A systematic review. *Quintessence Int*, 47: 25-37.
 69. Woelber JP, Fleiner J, Rau J, Ratka-Krüger P, Hannig C. (2018) Accuracy and Usefulness of CBCT in Periodontology: A Systematic Review of the Literature. *Int J Periodontics Restorative Dent*, 38: 289-297.
 70. Eickholz P, Kim TS, Benn DK, Staehle HJ. (1998) Validity of radiographic measurement of interproximal bone loss. *Oral Surg Oral Med Oral Pathol Oral Radiol Endod*, 85: 99-106.
 71. Christiaens V, De Bruyn H, Thevissen E, Koole S, Dierens M, Cosyn J. (2018) Assessment of periodontal bone level revisited: a controlled study on the diagnostic accuracy of clinical evaluation methods and intra-oral radiography. *Clin Oral Investig*, 22: 425-431.
 72. Rams TE, Slots J. (1993) Comparison of two pressure-sensitive periodontal probes and a manual periodontal probe in shallow and deep pockets. *Int J Periodontics Restorative Dent*, 13: 520-529.
 73. Updegrave WJ. (1951) The paralleling extension-cone technique in intraoral dental radiography. *Oral Surg Oral Med Oral Pathol*, 4: 1250-1261.
 74. Vandenberghe B, Jacobs R, Yang J. (2007) Diagnostic validity (or acuity) of 2D CCD versus 3D CBCT-images for assessing periodontal breakdown. *Oral Surg Oral Med Oral Pathol Oral Radiol Endod*, 104: 395-401.
 75. Vandenberghe B, Jacobs R, Yang J. (2008) Detection of periodontal bone loss using digital intraoral and cone beam computed tomography images: an in vitro

- assessment of bony and/or infrabony defects. *Dentomaxillofac Radiol*, 37: 252-260.
76. de Faria Vasconcelos K, Evangelista KM, Rodrigues CD, Estrela C, de Sousa TO, Silva MA. (2012) Detection of periodontal bone loss using cone beam CT and intraoral radiography. *Dentomaxillofac Radiol*, 41: 64-69.
 77. Grimard BA, Hoidal MJ, Mills MP, Mellonig JT, Nummikoski PV, Mealey BL. (2009) Comparison of clinical, periapical radiograph, and cone-beam volume tomography measurement techniques for assessing bone level changes following regenerative periodontal therapy. *J Periodontol*, 80: 48-55.
 78. Walter C, Kaner D, Berndt DC, Weiger R, Zitzmann NU. (2009) Three-dimensional imaging as a pre-operative tool in decision making for furcation surgery. *J Clin Periodontol*, 36: 250-257.
 79. Cimbajevic MM, Spin-Neto RR, Miletic VJ, Jankovic SM, Aleksic ZM, Nikolic-Jakoba NS. (2015) Clinical and CBCT-based diagnosis of furcation involvement in patients with severe periodontitis. *Quintessence Int*, 46: 863-870.
 80. Yusof NAM, Noor E, Reduwan NH, Yusof M. (2021) Diagnostic accuracy of periapical radiograph, cone beam computed tomography, and intrasurgical linear measurement techniques for assessing furcation defects: a longitudinal randomised controlled trial. *Clin Oral Investig*, 25: 923-932.
 81. Rinne CA, Dagassan-Berndt DC, Connert T, Müller-Gerbl M, Weiger R, Walter C. (2020) Impact of CBCT image quality on the confidence of furcation measurements. *J Clin Periodontol*, 47: 816-824.
 82. Zhang X, Li Y, Ge Z, Zhao H, Miao L, Pan Y. (2020) The dimension and morphology of alveolar bone at maxillary anterior teeth in periodontitis: a retrospective analysis-using CBCT. *Int J Oral Sci*, 12: 4.
 83. Nikolic-Jakoba N, Spin-Neto R, Wenzel A. (2016) Cone-Beam Computed Tomography for Detection of Intrabony and Furcation Defects: A Systematic Review Based on a Hierarchical Model for Diagnostic Efficacy. *J Periodontol*, 87: 630-644.
 84. Nemoto Y, Kubota T, Nohno K, Nezu A, Morozumi T, Yoshie H. (2018) Clinical and CBCT Evaluation of Combined Periodontal Regenerative Therapies Using

- Enamel Matrix Derivative and Deproteinized Bovine Bone Mineral With or Without Collagen Membrane. *Int J Periodontics Restorative Dent*, 38: 373-381.
85. Gonçalves BC, Costa ALF, Correa R, Andere N, Ogawa CM, Santamaria MP, de Castro Lopes SLP. (2021) Analysis of geometrical tomographic parameters of furcation lesions in periodontitis patients. *Heliyon*, 7: e06119.
 86. Mohan R, Mark R, Sing I, Jain A. (2014) Diagnostic Accuracy of CBCT for Aggressive Periodontitis. *J Clin Imaging Sci*, 4: 2.
 87. Tayman MA, Kamburoğlu K, Küçük Ö, Ateş F, Günhan M. (2019) Comparison of linear and volumetric measurements obtained from periodontal defects by using cone beam-CT and micro-CT: an in vitro study. *Clin Oral Investig*, 23: 2235-2244.
 88. Yan ZY, Tan Y, Xie XY, He W, Guo CB, Cui NH. (2020) Computer-aided three-dimensional assessment of periodontal healing distal to the mandibular second molar after coronectomy of the mandibular third molar: a prospective study. *BMC Oral Health*, 20: 264.
 89. Cortellini P, Tonetti MS. (2015) Clinical concepts for regenerative therapy in intrabony defects. *Periodontol 2000*, 68: 282-307.
 90. Trombelli L, Farina R, Franceschetti G, Calura G. (2009) Single-flap approach with buccal access in periodontal reconstructive procedures. *J Periodontol*, 80: 353-360.
 91. Aslan S, Buduneli N, Cortellini P. (2017) Entire Papilla Preservation Technique: A Novel Surgical Approach for Regenerative Treatment of Deep and Wide Intrabony Defects. *Int J Periodontics Restorative Dent*, 37: 227-233.
 92. Moreno Rodríguez JA, Ortiz Ruiz AJ, Caffesse RG. (2019) Supra-alveolar attachment gain in the treatment of combined intra-suprabony periodontal defects by non-incised papillae surgical approach. *J Clin Periodontol*, 46: 927-936.
 93. McGuire MK, Nunn ME. (1996) Prognosis versus actual outcome. II. The effectiveness of clinical parameters in developing an accurate prognosis. *J Periodontol*, 67: 658-665.
 94. Karoussis IK, Kotsovilis S, Fourmoussis I. (2007) A comprehensive and critical review of dental implant prognosis in periodontally compromised partially edentulous patients. *Clin Oral Implants Res*, 18: 669-679.

95. Caplanis N, Lozada JL, Kan JY. (2005) Extraction defect assessment, classification, and management. *J Calif Dent Assoc*, 33: 853-863.
96. Clementini M, Agostinelli A, Castelluzzo W, Cugnata F, Vignoletti F, De Sanctis M. (2019) The effect of immediate implant placement on alveolar ridge preservation compared to spontaneous healing after tooth extraction: Radiographic results of a randomized controlled clinical trial. *J Clin Periodontol*, 46: 776-786.
97. Temmerman A, Vandessel J, Castro A, Jacobs R, Teughels W, Pinto N, Quirynen M. (2016) The use of leucocyte and platelet-rich fibrin in socket management and ridge preservation: a split-mouth, randomized, controlled clinical trial. *J Clin Periodontol*, 43: 990-999.
98. Hammarström L, Heijl L, Gestrelus S. (1997) Periodontal regeneration in a buccal dehiscence model in monkeys after application of enamel matrix proteins. *J Clin Periodontol*, 24: 669-677.
99. Heijl L. (1997) Periodontal regeneration with enamel matrix derivative in one human experimental defect. A case report. *J Clin Periodontol*, 24: 693-696.
100. Sculean A, Windisch P, Keglevich T, Fabi B, Lundgren E, Lyngstadaas PS. (2002) Presence of an enamel matrix protein derivative on human teeth following periodontal surgery. *Clin Oral Investig*, 6: 183-187.
101. Windisch P, Sculean A, Klein F, Tóth V, Gera I, Reich E, Eickholz P. (2002) Comparison of clinical, radiographic, and histometric measurements following treatment with guided tissue regeneration or enamel matrix proteins in human periodontal defects. *J Periodontol*, 73: 409-417.
102. Harrel SK. (1998) A minimally invasive surgical approach for periodontal bone grafting. *Int J Periodontics Restorative Dent*, 18: 161-169.
103. Harrel SK, Abraham CM, Rivera-Hidalgo F, Shulman JD, Nunn ME. (2014) Videoscope-assisted minimally invasive periodontal surgery (V-MIS). *J Clin Periodontol*, 41: 900-907.
104. Harrel SK, Wilson TG, Jr., Rivera-Hidalgo F. (2013) A videoscope for use in minimally invasive periodontal surgery. *J Clin Periodontol*, 40: 868-874.

105. Cortellini P, Prato GP, Tonetti MS. (1995) The modified papilla preservation technique. A new surgical approach for interproximal regenerative procedures. *J Periodontol*, 66: 261-266.
106. Cortellini P, Prato GP, Tonetti MS. (1999) The simplified papilla preservation flap. A novel surgical approach for the management of soft tissues in regenerative procedures. *Int J Periodontics Restorative Dent*, 19: 589-599.
107. Cortellini P, Tonetti MS. (2007) A minimally invasive surgical technique with an enamel matrix derivative in the regenerative treatment of intra-bony defects: a novel approach to limit morbidity. *J Clin Periodontol*, 34: 87-93.
108. Cortellini P, Tonetti MS. (2009) Improved wound stability with a modified minimally invasive surgical technique in the regenerative treatment of isolated interdental intrabony defects. *J Clin Periodontol*, 36: 157-163.
109. Tunnell JC, Harrel SK. (2017) Minimally Invasive Surgery in Periodontal Regeneration: A Review of the Literature. *Compend Contin Educ Dent*, 38: e13-e16.
110. Trombelli L, Simonelli A, Quaranta A, Tu YK, Li H, Augusto M, Jiao XJ, Farina R. (2021) Effect of Flap Design for Enamel Matrix Derivative Application in Intraosseous Defects. *JDR Clin Trans Res*, 6: 184-194.
111. Clementini M, Ambrosi A, Cicciarelli V, De Risi V, de Sanctis M. (2019) Clinical performance of minimally invasive periodontal surgery in the treatment of infrabony defects: Systematic review and meta-analysis. *J Clin Periodontol*, 46: 1236-1253.
112. Cortellini P, Tonetti MS. (2011) Clinical and radiographic outcomes of the modified minimally invasive surgical technique with and without regenerative materials: a randomized-controlled trial in intra-bony defects. *J Clin Periodontol*, 38: 365-373.
113. Azuma H, Kono T, Morita H, Tsumori N, Miki H, Shiomi K, Umeda M. (2017) Single Flap Periodontal Surgery Induces Early Fibrous Tissue Generation by Wound Stabilization. *Journal of Hard Tissue Biology*, 26: 119-126.
114. Araújo MG, Lindhe J. (2005) Dimensional ridge alterations following tooth extraction. An experimental study in the dog. *J Clin Periodontol*, 32: 212-218.

115. Molnár B, Deutsch T, Marton R, Orbán K, Martin A, Windisch P. (2019) Demonstration of Radiographic Bone Fill in Postextraction Sockets Using a Novel Implant-Site Development Technique: A Retrospective Comparative Case Series. *Int J Periodontics Restorative Dent*, 39: 845-852.
116. García-González S, Galve-Huertas A, Aboul-Hosn Centenero S, Mareque-Bueno S, Satorres-Nieto M, Hernández-Alfaro F. (2020) Volumetric changes in alveolar ridge preservation with a compromised buccal wall: a systematic review and meta-analysis. *Med Oral Patol Oral Cir Bucal*, 25: e565-e575.
117. Darby I, Chen ST, Buser D. (2009) Ridge preservation techniques for implant therapy. *Int J Oral Maxillofac Implants*, 24 Suppl: 260-271.
118. Horváth A, Mardas N, Mezzomo LA, Needleman IG, Donos N. (2013) Alveolar ridge preservation. A systematic review. *Clin Oral Investig*, 17: 341-363.
119. Vittorini Orgeas G, Clementini M, De Risi V, de Sanctis M. (2013) Surgical techniques for alveolar socket preservation: a systematic review. *Int J Oral Maxillofac Implants*, 28: 1049-1061.
120. Araújo MG, Lindhe J. (2009) Ridge preservation with the use of Bio-Oss collagen: A 6-month study in the dog. *Clin Oral Implants Res*, 20: 433-440.
121. Araújo MG, Lindhe J. (2011) Socket grafting with the use of autologous bone: an experimental study in the dog. *Clin Oral Implants Res*, 22: 9-13.
122. Lindhe J, Araújo MG, Bufler M, Liljenberg B. (2013) Biphasic alloplastic graft used to preserve the dimension of the edentulous ridge: an experimental study in the dog. *Clin Oral Implants Res*, 24: 1158-1163.
123. Cardaropoli D, Tamagnone L, Roffredo A, De Maria A, Gaveglio L. (2018) Alveolar Ridge Preservation Using Tridimensional Collagen Matrix and Deproteinized Bovine Bone Mineral in the Esthetic Area: A CBCT and Histologic Human Pilot Study. *Int J Periodontics Restorative Dent*, 38: s29-s35.
124. Lekovic V, Camargo PM, Klokkevold PR, Weinlaender M, Kenney EB, Dimitrijevic B, Nedic M. (1998) Preservation of alveolar bone in extraction sockets using bioabsorbable membranes. *J Periodontol*, 69: 1044-1049.
125. Zadeh HH. (2011) Minimally invasive treatment of maxillary anterior gingival recession defects by vestibular incision subperiosteal tunnel access and platelet-derived growth factor BB. *Int J Periodontics Restorative Dent*, 31: 653-660.

126. Ellegaard B, Løe H. (1971) New attachment of periodontal tissues after treatment of intrabony lesions. *J Periodontol*, 42: 648-652.
127. Nyman S, Lindhe J, Karring T, Rylander H. (1982) New attachment following surgical treatment of human periodontal disease. *J Clin Periodontol*, 9: 290-296.
128. Machtei EE. (1997) Outcome variables for the study of periodontal regeneration. *Ann Periodontol*, 2: 229-239.
129. Reddy MS, Jeffcoat MK. (1999) Methods of assessing periodontal regeneration. *Periodontol 2000*, 19: 87-103.
130. Mealey BL, Neubauer MF, Butzin CA, Waldrop TC. (1994) Use of furcal bone sounding to improve accuracy of furcation diagnosis. *J Periodontol*, 65: 649-657.
131. Cortellini P, Pini Prato G, Tonetti MS. (1993) Periodontal regeneration of human infrabony defects. II. Re-entry procedures and bone measures. *J Periodontol*, 64: 261-268.
132. Porto OCL, Silva BSF, Silva JA, Estrela CRA, Alencar AHG, Bueno MDR, Estrela C. (2020) CBCT assessment of bone thickness in maxillary and mandibular teeth: an anatomic study. *J Appl Oral Sci*, 28: e20190148.
133. Sun DJ, Lim HC, Lee DW. (2019) Alveolar ridge preservation using an open membrane approach for sockets with bone deficiency: A randomized controlled clinical trial. *Clin Implant Dent Relat Res*, 21: 175-182.
134. Chappuis V, Engel O, Reyes M, Shahim K, Nolte LP, Buser D. (2013) Ridge alterations post-extraction in the esthetic zone: a 3D analysis with CBCT. *J Dent Res*, 92: 195s-201s.
135. Wongpairojpanich J, Kijartorn P, Suwanprateeb J, Buranawat B. (2021) Effectiveness of bilayer porous polyethylene membrane for alveolar ridge preservation: A randomized controlled trial. *Clin Implant Dent Relat Res*, 23: 73-85.
136. Fedorov A, Beichel R, Kalpathy-Cramer J, Finet J, Fillion-Robin JC, Pujol S, Bauer C, Jennings D, Fennessy F, Sonka M, Buatti J, Aylward S, Miller JV, Pieper S, Kikinis R. (2012) 3D Slicer as an image computing platform for the Quantitative Imaging Network. *Magn Reson Imaging*, 30: 1323-1341.

137. Palkovics D, Solyom E, Molnar B, Pinter C, Windisch P. (2021) Digital Hybrid Model Preparation for Virtual Planning of Reconstructive Dentoalveolar Surgical Procedures. *J Vis Exp*, doi:10.3791/62743.
138. Pinter C, Lasso A, Fichtinger G. (2019) Polymorph segmentation representation for medical image computing. *Comput Methods Programs Biomed*, 171: 19-26.
139. Omran J, Enezate T, Abdullah O, Al-Dadah AS, Aronow HD, Mustapha J, Saab F, Brilakis ES, Reeves RR, Bhatt DL, Mahmud E. (2018) Bivalirudin versus unfractionated heparin in peripheral vascular interventions. *Cardiovasc Revasc Med*, 19: 695-699.
140. Albu AB, Beugeling T, Laurendeau D. (2008) A morphology-based approach for interslice interpolation of anatomical slices from volumetric images. *IEEE Trans Biomed Eng*, 55: 2022-2038.
141. Zukić D, Vicory, J., McCormick, M., Wisse, L., Gerig, G., Yushkevich, P., Aylward, S. . (2016) N-D morphological contour interpolation. *Insight Journal*.
142. Taubin G, Zhang T, Golub G. Optimal surface smoothing as filter design. In: *Computer Vision — ECCV '96 (Buxton B, Cipolla R szerk.)*. Springer Berlin Heidelberg, Berlin, Heidelberg, 1996: 283-292.
143. Joda T, Brägger U, Gallucci G. (2015) Systematic literature review of digital three-dimensional superimposition techniques to create virtual dental patients. *Int J Oral Maxillofac Implants*, 30: 330-337.
144. Mangano C, Luongo F, Migliario M, Mortellaro C, Mangano FG. (2018) Combining Intraoral Scans, Cone Beam Computed Tomography and Face Scans: The Virtual Patient. *J Craniofac Surg*, 29: 2241-2246.
145. Ungi T, Lasso A, Fichtinger G. (2016) Open-source platforms for navigated image-guided interventions. *Med Image Anal*, 33: 181-186.
146. Flügge T, Derksen W, Te Poel J, Hassan B, Nelson K, Wismeijer D. (2017) Registration of cone beam computed tomography data and intraoral surface scans - A prerequisite for guided implant surgery with CAD/CAM drilling guides. *Clin Oral Implants Res*, 28: 1113-1118.
147. Jamjoom FZ, Kim DG, Lee DJ, McGlumphy EA, Yilmaz B. (2018) Effect of length and location of edentulous area on the accuracy of prosthetic treatment plan

- incorporation into cone-beam computed tomography scans. *Clin Implant Dent Relat Res*, 20: 300-307.
148. Deferm JT, Nijsink J, Baan F, Verhamme L, Meijer G, Maal T. (2021) Soft tissue-based registration of intraoral scan with cone beam computed tomography scan. *Int J Oral Maxillofac Surg*, doi:10.1016/j.ijom.2021.04.004.
 149. Ritter L, Reiz SD, Rothamel D, Dreiseidler T, Karapetian V, Scheer M, Zöller JE. (2012) Registration accuracy of three-dimensional surface and cone beam computed tomography data for virtual implant planning. *Clin Oral Implants Res*, 23: 447-452.
 150. Swennen GR, Barth EL, Eulzer C, Schutyser F. (2007) The use of a new 3D splint and double CT scan procedure to obtain an accurate anatomic virtual augmented model of the skull. *Int J Oral Maxillofac Surg*, 36: 146-152.
 151. Pascual D, Vaysse J. (2016) [Guided and computer-assisted implant surgery and prosthetic: The continuous digital workflow]. *Rev Stomatol Chir Maxillofac Chir Orale*, 117: 28-35.
 152. Mehl A. (2013) The "virtual patient" in medicine and dentistry. *Int J Comput Dent*, 16: 3-5.
 153. Ottmann T, Widmayer P, Wood D. (1985) A fast algorithm for the Boolean masking problem. *Computer Vision, Graphics, and Image Processing*, 30: 249-268.
 154. Gindis E. Chapter 24 - Boolean Operations. In: Gindis E (szerk.), *Up and Running with AutoCAD 2013 (Third Edition)*, doi:<https://doi.org/10.1016/B978-0-12-398416-6.00024-2>. Academic Press, Boston, 2013: 533-542.
 155. Bayrak S, Kursun Cakmak ES, Kamalak H. (2020) Contrast-to-noise ratios of different dental restorative materials: an in-vitro cone beam computed tomography study. *Eur Oral Res*, 54: 36-41.
 156. Nardi C, Borri C, Regini F, Calistri L, Castellani A, Lorini C, Colagrande S. (2015) Metal and motion artifacts by cone beam computed tomography (CBCT) in dental and maxillofacial study. *Radiol Med*, 120: 618-626.
 157. Nabha W, Hong YM, Cho JH, Hwang HS. (2014) Assessment of metal artifacts in three-dimensional dental surface models derived by cone-beam computed tomography. *Korean J Orthod*, 44: 229-235.

158. Almutairi T, Naudi K, Nairn N, Ju X, Whitters J, Ayoub A. (2018) Replacement of the Distorted Dentition of the Cone-Beam Computed Tomography Scans for Orthognathic Surgery Planning. *J Oral Maxillofac Surg*, 76: 1561.e1561-1561.e1568.
159. Nairn NJ, Ayoub AF, Barbenel J, Moos K, Naudi K, Ju X, Khambay BS. (2013) Digital replacement of the distorted dentition acquired by cone beam computed tomography (CBCT): a pilot study. *Int J Oral Maxillofac Surg*, 42: 1488-1493.
160. Misch KA, Yi ES, Sarment DP. (2006) Accuracy of cone beam computed tomography for periodontal defect measurements. *J Periodontol*, 77: 1261-1266.
161. Palkovics D, Mangano FG, Nagy K, Windisch P. (2020) Digital three-dimensional visualization of intrabony periodontal defects for regenerative surgical treatment planning. *BMC Oral Health*, 20: 351.
162. Papapanou PN, Tonetti MS. (2000) Diagnosis and epidemiology of periodontal osseous lesions. *Periodontol 2000*, 22: 8-21.
163. Goldman HM, Cohen DW. (1958) The Infrabony Pocket: Classification and Treatment. *The Journal of Periodontology*, 29: 272-291.
164. Hamp SE, Nyman S, Lindhe J. (1975) Periodontal treatment of multirrooted teeth. Results after 5 years. *J Clin Periodontol*, 2: 126-135.
165. Sólyom E, Palkovics D, Pintér C, Mangano FG, Windisch P. (2021) Virtuális tervezés és volumetrikus kiértékelés egy komplex parodontális defektus regeneratív-rekonstruktív sebészi ellátásában: Egy eset bemutatása. *Fogorvosi Szemle*, 114: 120-130.
166. Dawood A, Marti Marti B, Sauret-Jackson V, Darwood A. (2015) 3D printing in dentistry. *Br Dent J*, 219: 521-529.
167. Tejo-Otero A, Buj-Corral I, Fenollosa-Artés F. (2020) 3D Printing in Medicine for Preoperative Surgical Planning: A Review. *Ann Biomed Eng*, 48: 536-555.
168. Marei HF, Alshaia A, Alarifi S, Almasoud N, Abdelhady A. (2019) Effect of Steam Heat Sterilization on the Accuracy of 3D Printed Surgical Guides. *Implant Dent*, 28: 372-377.
169. Chao JC. (2012) A novel approach to root coverage: the pinhole surgical technique. *Int J Periodontics Restorative Dent*, 32: 521-531.

170. Ganguli A, Pagan-Diaz GJ, Grant L, Cvetkovic C, Bramlet M, Vozenilek J, Kesavadas T, Bashir R. (2018) 3D printing for preoperative planning and surgical training: a review. *Biomed Microdevices*, 20: 65.
171. Borracci RA, Ferreira LM, Alvarez Gallesio JM, Tenorio Núñez OM, David M, Eyheremendy EP. (2021) Three-dimensional virtual and printed models for planning adult cardiovascular surgery. *Acta Cardiol*, 76: 534-543.
172. Brouwers L, Teutelink A, van Tilborg F, de Jongh MAC, Lansink KWW, Bemelman M. (2019) Validation study of 3D-printed anatomical models using 2 PLA printers for preoperative planning in trauma surgery, a human cadaver study. *Eur J Trauma Emerg Surg*, 45: 1013-1020.
173. Sculean A, Chiantella GC, Windisch P, Arweiler NB, Brex M, Gera I. (2005) Healing of intra-bony defects following treatment with a composite bovine-derived xenograft (Bio-Oss Collagen) in combination with a collagen membrane (Bio-Gide PERIO). *J Clin Periodontol*, 32: 720-724.
174. Palkovics D, Pinter C, Bartha F, Molnar B, Windisch P. (2021) CBCT subtraction analysis of 3D changes following alveolar ridge preservation: a case series of 10 patients with 6-months follow-up. *Int J Comput Dent*, 24: 241-251.
175. Klein S, Staring M, Murphy K, Viergever MA, Pluim JP. (2010) elastix: a toolbox for intensity-based medical image registration. *IEEE Trans Med Imaging*, 29: 196-205.
176. Yushkevich PA, Yang G, Gerig G. (2016) ITK-SNAP: An interactive tool for semi-automatic segmentation of multi-modality biomedical images. *Annu Int Conf IEEE Eng Med Biol Soc*, 2016: 3342-3345.
177. Gultekin BA, Cansiz E, Borahan O, Mangano C, Kolerman R, Mijiritsky E, Yalcin S. (2016) Evaluation of Volumetric Changes of Augmented Maxillary Sinus With Different Bone Grafting Biomaterials. *J Craniofac Surg*, 27: e144-148.
178. Li Y, Qiao SC, Gu YX, Zhang XM, Shi JY, Lai HC. (2019) A novel semiautomatic segmentation protocol to evaluate guided bone regeneration outcomes: A pilot randomized, controlled clinical trial. *Clin Oral Implants Res*, 30: 344-352.

179. Yilmaz P, Wallecan K, Kristanto W, Aben JP, Moelker A. (2018) Evaluation of a Semi-automatic Right Ventricle Segmentation Method on Short-Axis MR Images. *J Digit Imaging*, 31: 670-679.
180. Zou Z, Liao SH, Luo SD, Liu Q, Liu SJ. (2017) Semi-automatic segmentation of femur based on harmonic barrier. *Comput Methods Programs Biomed*, 143: 171-184.
181. Benke K, Barabás JI, Daróczy L, Sayour AA, Szilveszter B, Pólos M, Lux Á, Székely A, Radovits T, Hartyánszky I, Merkely B, Szabolcs Z. (2017) Routine aortic valve replacement followed by a myriad of complications: role of 3D printing in a difficult cardiac surgical case. *J Thorac Dis*, 9: E1021-e1024.
182. Barabás JI, Pólos M, Daróczy L, Hüttl T, Benke K, Horkay F, Szabolcs Z, Hartyánszky I. (2018) [Computer-assisted decision-making in cardiac surgery: from 3D preoperative planning to computational fluid dynamics in the design of surgical procedures]. *Magy Seb*, 71: 117-125.
183. Barabás JI, Ghimessy Á K, Rényi-Vámos F, Kocsis Á, Agócs L, Mészáros L, Pukacsik D, Andi J, Laki A, Vörös F, Hartyánszky I, Panajotu A, Fazekas L, Szabolcs Z, Merkely B. (2019) [Innovation in medicine: opportunities of 3D modeling and printing for perioperative care of cardio and thoracic surgical patients. Experiences in Hungary]. *Orv Hetil*, 160: 1967-1975.
184. Alsufyani NA, Flores-Mir C, Major PW. (2012) Three-dimensional segmentation of the upper airway using cone beam CT: a systematic review. *Dentomaxillofac Radiol*, 41: 276-284.
185. Loubele M, Maes F, Schutyser F, Marchal G, Jacobs R, Suetens P. (2006) Assessment of bone segmentation quality of cone-beam CT versus multislice spiral CT: a pilot study. *Oral Surg Oral Med Oral Pathol Oral Radiol Endod*, 102: 225-234.
186. Lahoud P, EzEldeen M, Beznik T, Willems H, Leite A, Van Gerven A, Jacobs R. (2021) Artificial Intelligence for Fast and Accurate 3-Dimensional Tooth Segmentation on Cone-beam Computed Tomography. *J Endod*, 47: 827-835.
187. Li Q, Chen K, Han L, Zhuang Y, Li J, Lin J. (2020) Automatic tooth roots segmentation of cone beam computed tomography image sequences using U-net and RNN. *J Xray Sci Technol*, 28: 905-922.

188. D'Haese J, Ackhurst J, Wismeijer D, De Bruyn H, Tahmaseb A. (2017) Current state of the art of computer-guided implant surgery. *Periodontol 2000*, 73: 121-133.
189. Varga E, Jr., Antal M, Major L, Kiscsatári R, Braunitzer G, Piffkó J. (2020) Guidance means accuracy: A randomized clinical trial on freehand versus guided dental implantation. *Clin Oral Implants Res*, 31: 417-430.
190. Harris BT, Montero D, Grant GT, Morton D, Llop DR, Lin WS. (2017) Creation of a 3-dimensional virtual dental patient for computer-guided surgery and CAD-CAM interim complete removable and fixed dental prostheses: A clinical report. *J Prosthet Dent*, 117: 197-204.
191. Hassan B, Greven M, Wismeijer D. (2017) Integrating 3D facial scanning in a digital workflow to CAD/CAM design and fabricate complete dentures for immediate total mouth rehabilitation. *J Adv Prosthodont*, 9: 381-386.
192. Lang NP, Joss A, Orsanic T, Gusberti FA, Siegrist BE. (1986) Bleeding on probing. A predictor for the progression of periodontal disease? *J Clin Periodontol*, 13: 590-596.
193. Kasaj A, Willershausen B. (2007) Digital volume tomography for diagnostics in periodontology. *Int J Comput Dent*, 10: 155-168.
194. Pauwels R, Beinsberger J, Collaert B, Theodorakou C, Rogers J, Walker A, Cockmartin L, Bosmans H, Jacobs R, Bogaerts R, Horner K. (2012) Effective dose range for dental cone beam computed tomography scanners. *Eur J Radiol*, 81: 267-271.
195. Ludlow JB, Davies-Ludlow LE, White SC. (2008) Patient risk related to common dental radiographic examinations: the impact of 2007 International Commission on Radiological Protection recommendations regarding dose calculation. *J Am Dent Assoc*, 139: 1237-1243.
196. Oenning AC, Jacobs R, Salmon B. (2021) ALADAIP, beyond ALARA and towards personalized optimization for paediatric cone-beam CT. *Int J Paediatr Dent*, doi:10.1111/ipd.12797.
197. Queiroz PM, Santaella GM, Groppo FC, Freitas DQ. (2018) Metal artifact production and reduction in CBCT with different numbers of basis images. *Imaging Sci Dent*, 48: 41-44.

198. Lei L, Yu Y, Ke T, Sun W, Chen L. (2019) The Application of Three-Dimensional Printing Model and Platelet-Rich Fibrin Technology in Guided Tissue Regeneration Surgery for Severe Bone Defects. *J Oral Implantol*, 45: 35-43.
199. Rodriguez-Salvador M, Ruiz-Cantu L. (2019) Revealing emerging science and technology research for dentistry applications of 3D bioprinting. *Int J Bioprint*, 5: 170.
200. Rasperini G, Pilipchuk SP, Flanagan CL, Park CH, Pagni G, Hollister SJ, Giannobile WV. (2015) 3D-printed Bioresorbable Scaffold for Periodontal Repair. *J Dent Res*, 94: 153s-157s.
201. Pellegrino G, Mangano C, Mangano R, Ferri A, Taraschi V, Marchetti C. (2019) Augmented reality for dental implantology: a pilot clinical report of two cases. *BMC Oral Health*, 19: 158.
202. Ludlow J, Koivisto J. Dosimetry of Orthodontic Diagnostic FOVs Using Low Dose CBCT protocol, 2015.
203. Kao RT, Nares S, Reynolds MA. (2015) Periodontal regeneration - intrabony defects: a systematic review from the AAP Regeneration Workshop. *J Periodontol*, 86: S77-104.
204. Falk H, Laurell L, Ravald N, Teiwik A, Persson R. (1997) Guided tissue regeneration therapy of 203 consecutively treated intrabony defects using a bioabsorbable matrix barrier. Clinical and radiographic findings. *J Periodontol*, 68: 571-581.
205. Huang Y, Dessel JV, Depypere M, EzEldeen M, Iliescu AA, Santos ED, Lambrechts I, Liang X, Jacobs R. (2014) Validating cone-beam computed tomography for peri-implant bone morphometric analysis. *Bone Res*, 2: 14010.
206. Bastami F, Shahab S, Parsa A, Abbas FM, Noori Kooshki MH, Namdari M, Lisar HA, Rafiei T, Fahimipour F, Salehi M, Jafari M. (2018) Can gray values derived from CT and cone beam CT estimate new bone formation? An in vivo study. *Oral Maxillofac Surg*, 22: 13-20.
207. Sculean A, Stavropoulos A, Windisch P, Keglevich T, Karring T, Gera I. (2004) Healing of human intrabony defects following regenerative periodontal therapy with a bovine-derived xenograft and guided tissue regeneration. *Clin Oral Investig*, 8: 70-74.

208. Sculean A, Windisch P, Chiantella GC. (2004) Human histologic evaluation of an intrabony defect treated with enamel matrix derivative, xenograft, and GTR. *Int J Periodontics Restorative Dent*, 24: 326-333.
209. Richardson CR, Mellonig JT, Brunsvold MA, McDonnell HT, Cochran DL. (1999) Clinical evaluation of Bio-Oss: a bovine-derived xenograft for the treatment of periodontal osseous defects in humans. *J Clin Periodontol*, 26: 421-428.
210. Ben Amara H, Kim JJ, Kim HY, Lee J, Song HY, Koo KT. (2021) Is ridge preservation effective in the extraction sockets of periodontally compromised teeth? A randomized controlled trial. *J Clin Periodontol*, 48: 464-477.

11 BIBLIOGRAPHY OF THE CANDIDATE'S PUBLICATIONS

On the topic of the thesis:

1. **Palkovics D**, Mangano FG, Nagy K, Windisch P. (2020) Digital three-dimensional visualization of intrabony periodontal defects for regenerative surgical treatment planning. *BMC Oral Health*, 20: 351.
2. **Palkovics D**, Pinter C, Bartha F, Molnar B, Windisch P. (2021) CBCT subtraction analysis of 3D changes following alveolar ridge preservation: a case series of 10 patients with a 6-month follow-up. *Int J Comput Dent*, 24: 241-251.
3. **Palkovics D**, Solyom E, Molnar B, Pinter C, Windisch P. (2021) Digital Hybrid Model Preparation for Virtual Planning of Reconstructive Dentoalveolar Surgical Procedures. *J Vis Exp*, doi:10.3791/62743.
4. Sólyom E, **Palkovics D**, Pintér C, Mangano FG, Windisch P. (2021) Virtuális tervezés és volumetrikus kiértékelés egy komplex parodontális defektus regeneratív-rekonstruktív sebészi ellátásában: Egy eset bemutatása. *Fogorvosi Szemle*, 114: 120-130

Other publications:

1. **Palkovics D**, Gera I. (2016) [The significance of biotype in the predictability of dental-periodontal treatment]. *Fogorv Sz*, 109: 45-55.
2. Shahbazi A, Feigl G, Sculean A, Grimm A, **Palkovics D**, Molnár B, Windisch P. (2021) Vascular survey of the maxillary vestibule and gingiva-clinical impact on incision and flap design in periodontal and implant surgeries. *Clin Oral Investig*, 25: 539-546.
3. Windisch P, Iorio-Siciliano V, **Palkovics D**, Ramaglia L, Blasi A, Sculean A. (2021) The role of surgical flap design (minimally invasive flap vs. extended flap with papilla preservation) on the healing of intrabony defects treated with an enamel matrix derivative: a 12-month two-center randomized controlled clinical trial. *Clin Oral Investig*, doi:10.1007/s00784-021-04155-5.

12 ACKNOWLEDGEMENT

I would like to thank my supervisor **Prof. Dr. Peter Windisch** for his constant support of the research work and for providing his vast clinical knowledge and expertise during the studies.

I would like to thank **Prof. Dr. Katalin Nagy** for her constant support of my scientific progression.

I would like to thank **Dr. Bálint Molnár** for his indispensable help during preparation of the manuscripts.

I thank **Dr. Csaba Pintér** for the support he provided during radiographic image processing and for lending his stupendous knowledge in radiographic informatics.

I would like to thank **Dr. Francesco Guido Mangano** for encouraging the study of digital technologies in periodontal reconstructive surgery as well as for providing his support during manuscript preparation and submission.

I thank **Prof. Dr. István Gera** for his support of my studies and research work as a periodontist from the very beginning.

I would like to thank **Dr. Pál Nagy** for his thorough review for the home defense of this thesis.

I would like to thank all the co-authors who contributed to the preparation of the manuscripts.

I would like to thank my **father, László** and my **mother, Mónika** for their constant support.

Last but not least, this thesis could not have been prepared without the support of my **wife Veronika** and my wonderful **son Artúr**.